SLIDING MODE DIRECT TORQUE CONTROL OF THREE PHASE INDUCTION MACHINE APPLICABLE IN ELECTRIC VEHICLES

BY

AJAH, GENESIS NNAEMEKA
PG/M.ENG/12/62628

A THESIS SUBMITTED IN PARTIAL FULFILLMENT OF THE REQUIREMENTS FOR THE DEGREE OF MASTER OF ENGINEERING IN THE DEPARTMENT OF ELECTRICAL ENGINEERING IN THE UNIVERSITY OF NIGERIA, NSUKKA, NIGERIA.

SUPERVISOR: PROF. E.C. EJIOGU

FEBRUARY, 2015

Approval Page

SLIDING MODE DIRECT TORQUE CONTROL OF THREE-PHASE INDUCTION MACHINE APPLICABLE IN ELECTRIC VEHICLES

BY

AJAH, GENESIS NNAEMEKA
PG/M.ENG/12/62628

A THESIS SUBMITTED IN PARTIAL FULFILLMENT OF THE REQUIREMENTS FOR THE AWARD OF MASTERS DEGREE IN THE DEPARTMENT OF ELECTRICAL ENGINEERING, UNIVERSITY OF NIGERIA, NSUKKA, NIGERIA.

FEBRUARY, 2015

Genesis N. Ajah (Student)	Signature___________________	Date________________
Engr.Prof. E.C. Ejiogu (Supervisor)	Signature___________________	Date________________
Engr. Prof. E.C. Ejiogu (Head of Department)	Signature___________________	Date________________
Engr. Prof. E.S. Obe (Chairman, Faculty Post-Graduate Committee)	Signature___________________	Date________________
Engr. Prof. S.N. Ndubisi (External Examiner)	Signature___________________	Date________________

Certification

AJAH, GENESIS NNAEMEKA, a master's postgraduate student in the Department of Electrical Engineering with registration number *PG/M.ENG/12/62628* has satisfactorily completed the requirements for the award of the degree of Master of Engineering in Electrical Engineering.

The work embodied in this thesis is original and has not been submitted in part or full for any other diploma or degree of this or any other university to the best of our knowledge.

Engr. Prof. E.C. Ejiogu
Supervisor

Engr. Prof. E.C. Ejiogu
Head of Department

Engr. Prof. E.S. Obe
Chairman, Faculty Post Graduate Committee

Dedication

To my family and loved ones.

Acknowledgement

In this path I have chosen, there are shoulders that I have had the privilege to stand on, without which this work would not have been a success.

Immense gratitude goes to my supervisor, Prof. E.C. Ejiogu, whose unceasing and relentless support and drive made this thesis a reality. He taught me perseverance, attention to details and helped me achieve excellence. I am honoured to have been under your supervision and tutelage.

Prof. Agu, your wealth of knowledge is incredible, there was always a light in my path every time I consulted you. Dr. Odeh, thank you sir, you helped me up every time I stumbled. To the entire Department of Electrical engineering, your continuous support and concern is immeasurable. I will not fail to mention the laboratory staff who made sure I had all that I needed, they willingly gave their time and resources to ensure I achieved satisfactory results.

My friends who were there in the dire straits, constantly on stand-by, always there to help; Chuka Agalamanyi (Gali), Nnamdi Zobeashia (Benzino), Nwabueze Obioma (Zed), Chinaza (Nazii) am grateful.

My family and loved ones, you were always there. Daddy, thank you for the calls, mommy, thank you for the relentless prayers, and to my siblings, K-baba, Nnamo, Zibah and Ify, I love you sincerely. Dr. Anyadike, I'm blessed to have you and your family stand by me. Ammy, I typed up your name with a smile on my face; that should settle it. To my daughter, Annabelle, every time I looked around me, you were always that angel of light, I see you and my drive is renewed, I love you and thank you Winifred – you're a great woman.

For all my incredibly happy moments and not-so-good times during this programme, I shared with you my colleagues. I am grateful, it was a privilege.

My Heavenly father, there is none like you. Praise the Lord.

Abstract

The electric vehicle relies on electric motors for propulsion. In this report, the case was made for the induction motor as a suitable candidate for this tractive application. Being able to control the electric motor invariably implies efficient control of the vehicle. This work reports the six-step operation of the constant volts/hertz (*V/f*) control technique for voltage fed induction motor drives. Mathematical equations supporting the principle is discussed and the drive is modelled and implemented in the open loop with results. The line and phase voltage outputs of the laboratory-implemented v/f drive is presented. The modelled results show the behaviour of the v/f drive under varying load conditions. The reference speed is set at 1800rpm while the actual speed only follows the reference speed until torque is applied at 0, 2, 3 and 4 seconds with torque values 0, –11, 11 and 0 Nm respectively. At 2 seconds, the actual speed changes (increases) from the reference speed slightly and reduces slightly when the positive torque is applied, but the speed does not totally match the reference speed until the torque is completely withdrawn. The Direct Torque Control (DTC) scheme is analysed mathematically and the principle of Variable Structure Systems (VSS) theory is applied to the DTC for robustness and tolerance to disturbances. DTC simulation results are presented, the system is run at steady state conditions, at time t = 0.4s, a load-torque disturbance causes it to reduce to one-half of its initial value. The objective of this drive scheme is to keep the load speed constant at its initial value. This causes a sharp increase in speed but it returns to the set reference speed in about 0.4s. This shows the control efficiency and robustness of the DTC scheme as compared with the v/f control method.

Content

List of Tables

List of Figures

Chapter 1

1 Introduction

1.1 Introduction

The block diagram in Figure 1.1 illustrates the elements of typical electric drive system. The elements of 4 and 5 are usually known, 1, 2 and 3 must be chosen. Hence, the mechanical system must be clearly specified. Also in the preliminary stages of the design, it is usually discovered that the power supply may, in some way, be inadequate. Therefore, an understanding of the mechanical system and the demands they make on the power supply is required.

The mechanical system, from the perspective of the motor, is a torque that must be applied to a shaft by the motor coupling. The relationship between this load torque and speed must be defined. For steady state operation, this definition can be described in terms of the four-quadrant speed-torque diagram (Figure 1.2), where ω is the speed of rotation of the motor/driven shaft and T_L is the load presented at the shaft of the mechanical system.

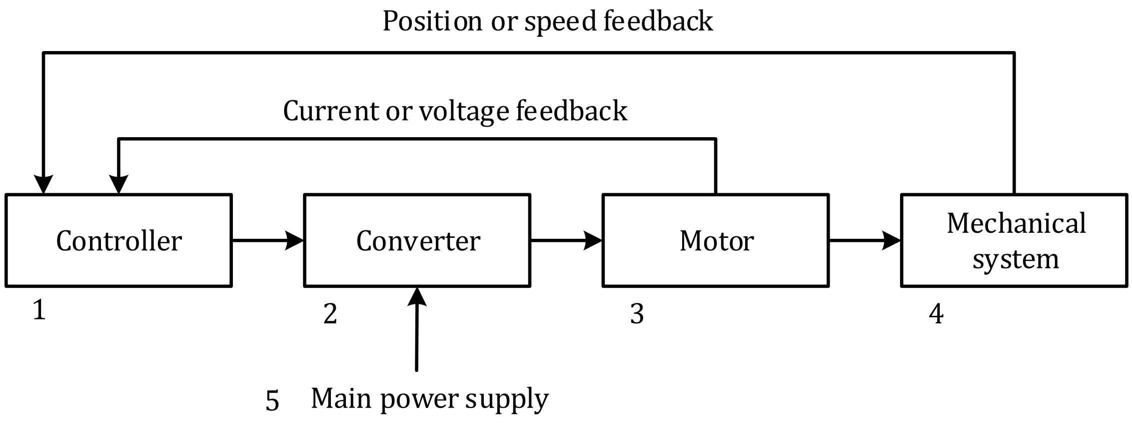

Figure 1.1 Drive system elements [1]

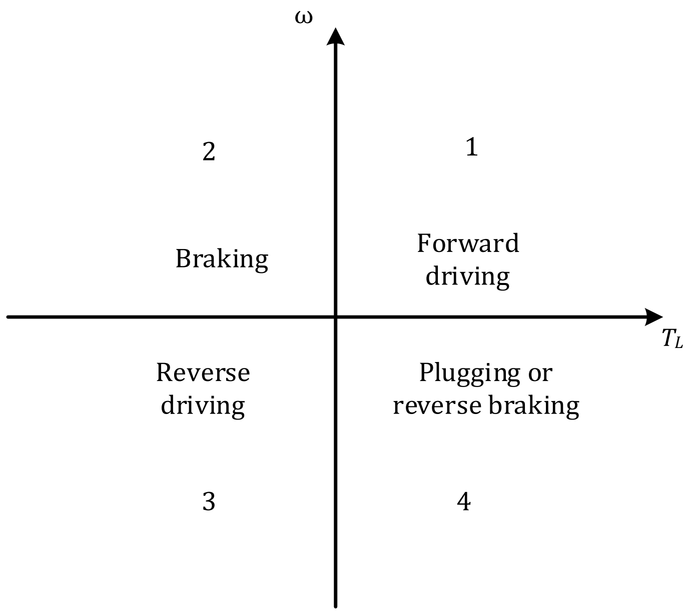

Figure 1.2 Four-quadrant speed-torque diagram

The first quadrant in Figure 1.2 above is the normal forward driving, in the second quadrant, the system demands a negative torque to provide braking. This braking torque may be produced by: (i) friction braking; a mechanical brake is coupled to the shaft and the kinetic energy is dissipated as heat due to friction, (ii) eddy-current braking; the kinetic energy is dissipated largely as eddy-current losses, (iii) dynamic braking; the motor acts as a generator and the energy generated is dissipated as heat in resistors provided for the purpose; (iv) Regenerative braking; the motor acts as a generator and transfers power back to the electric supply system. In the third quadrant, the motor torque and direction of rotation are reversed, similar to the first quadrant. The fourth quadrant may represent one of two possible conditions, if the electrical conditions are the same as in the first-quadrant driving, the mechanical system is driving the motor in a direction opposite to that which would result from its own developed torque. This is another type of braking referred to as plugging [1, 2]. Now, if the electrical conditions are changed to that in the third quadrant (reverse driving), then the types of braking described in the second quadrant are also obtainable.

For the purpose of this research, the mechanical system described here is the electric vehicle. Electric vehicles are highly adaptable and part of everyday society, especially in industrialized economies. Electric cars are found on mountain tops (railway trams, cable cars), at the bottom of the sea (submarines), in space exploration on the moon and even in neighbouring planet mars (Lunar Rover, *Spirit* and *Opportunity* Mars Rovers), in tall buildings (elevators), in cities (subways, light rail, buses, delivery vehicles), hauling heavy rail freight or moving rail passengers fast (Pennsylvania Railroad Washington to New York corridor [3], Tohoku Shinkansen Rail Line [4]) and in sports (Golf Cars, Trolleys) and even for entertainment as found in amusement parks. These are all electric vehicles, they run on rails, shafts, tethers, paved roads and off–road terrains and some run directly on battery power, non-rechargeable and rechargeable alike while some others utilize power directly from the grid.

Electric vehicle technology is now in its third century and still advancing [5] and can be classified in two categories, *1)* battery powered electric vehicle (BEV) and, *2)* the Hybrid Electric Vehicle (HEV). This study is centred on battery electric vehicles, henceforth referred to as “Electric Vehicle (EV)”. A conceptual modern electric drive train is illustrated in Figure 1.3 [6, 7]. Efforts will be made to describe the details of each sub-system.

The drivetrain comprises of 3 subsystems: electric propulsion subsystem, energy source subsystem and auxiliary subsystem. The energy subsystem, made up of the energy management unit, energy source and energy recharging unit, is directly connected to the other two subsystems. It supplies energy for propulsion and provides the necessary power with different voltage levels for all auxiliaries. The energy management unit cooperates with the vehicle controller to control the regenerative braking, its energy recovery and monitors the energy source. The electric propulsion subsystem is made up of the vehicle controller, electronic power converter, electric motor and the transmission. Signals received by the vehicle controller from the brake and accelerator pedals are processed and used to generate control signals to the power converter, which functions to regulate power flow between the electric motor and the energy source. Our interest lies in the electric propulsion system.

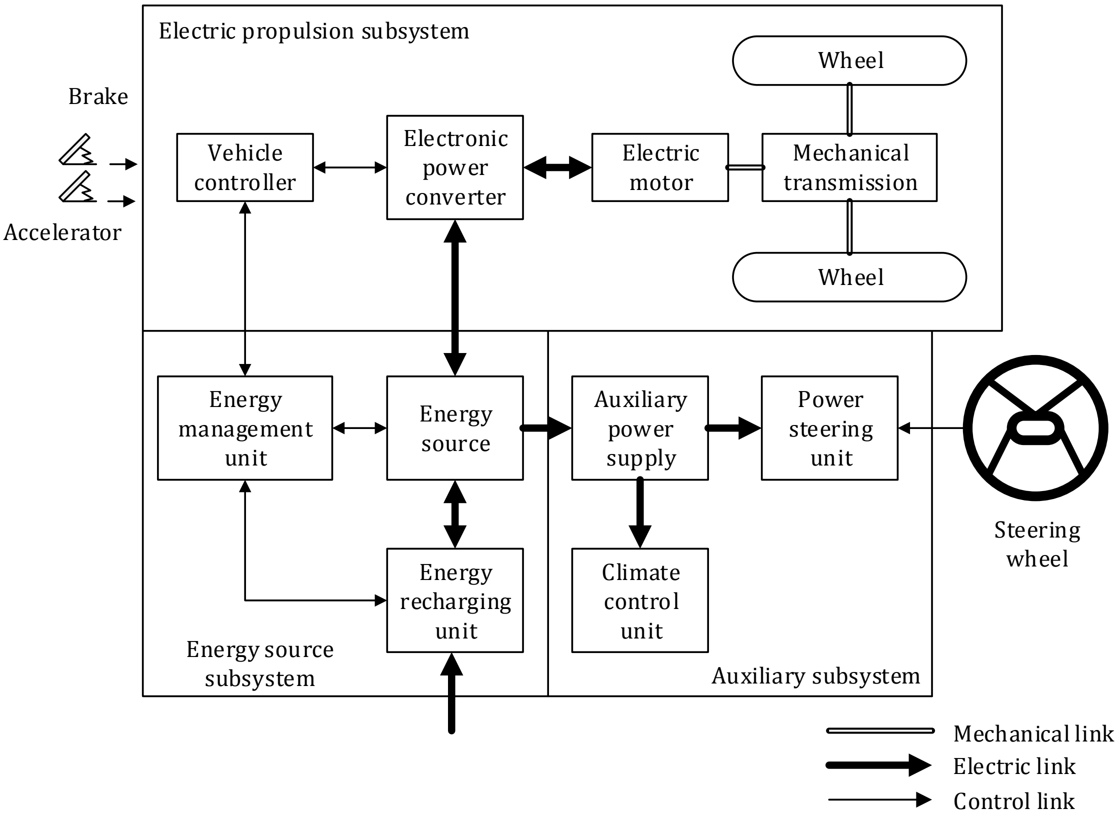

Figure 1.3 Conceptual illustration of general EV configuration [10]

1.1.1 EV Propulsion Systems

Electric propulsion systems are the heart of the EV [8, 9, 6, 10].The choice of electric propulsion system depends on a number of factors such as energy source, motor type and ratings, vehicle purpose and driver's expectations such as acceleration, maximum speed, climbing capability (gradeability), braking and range [6]. Vehicle purpose influences the weight and volume depending on the vehicle type while energy sources relates to batteries, fuel cells, ultra-capacitors, etc. Motor type is also critical and relies on vehicle purpose, available energy and driver's expectations.

The electric motor converts electrical energy into mechanical energy to propel the vehicle or vice versa, to enable regenerative braking and/or to charge the on-board energy storage. The power converter is used to supply the motor with appropriate voltage and current, the controllers command the power converter by sending control signals to it hence controlling the motor to produce proper torque and speed. The functional block diagram of an electric propulsion system is illustrated in Figure 1.4.

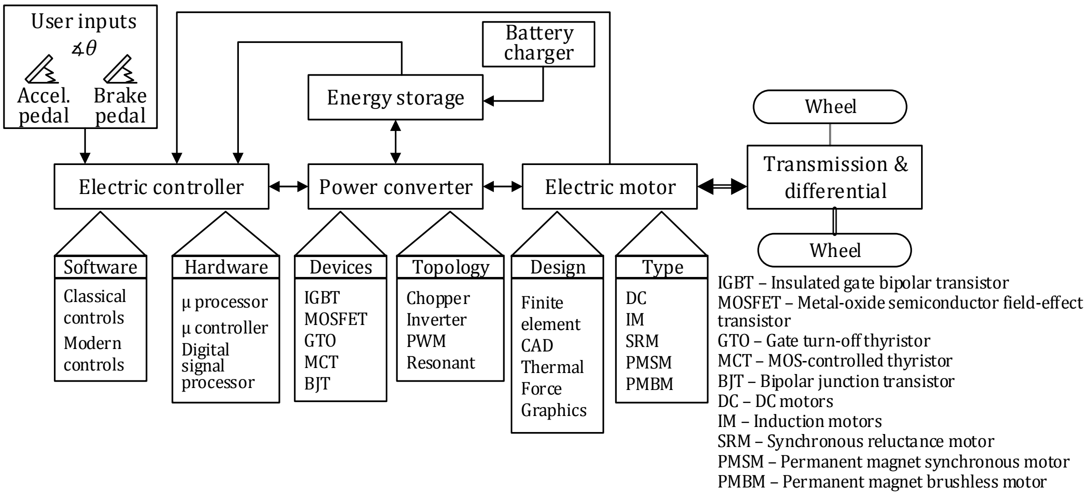

Figure 1.4 Functional block diagram of a typical electric propulsion system [7]

There are different types of motors in industrial application that may also be used to propel EVs. However some performance indexes have to be taken account of when motors are applied in EVs such as efficiency, weight, cost, dynamic characteristics of EVs [11]. For EV applications, motor requirements differ and usually require frequent starts and stops, high rates of acceleration/deceleration; high torque and low-speed hill climbing; low torque and high-speed cruising, the braking application calls for high torque at high speed, and holding that torque to low speed [12] and a very wide speed range of operation. It follows then, that there are characteristics that motors applied in EVs are expected to possess. Motor ratings compared to the conventional internal combustion (IC) engine power ratings and motor requirements for EVs are discussed as follows:

A. *Desired output characteristics of motor drives in EVs:*

The size or power output of electric motors and IC engines are typically described in horsepower (hp). The power that an electric motor can continuously deliver without overheating is its rated hp, which is typically a derated figure. For short periods of time, the motor can deliver two to four times the rated hp [3]. At starting, high power is available from an electric motor for acceleration, and the motor torque can be maximum under stall conditions, i.e., at zero speed. Motor type determines whether maximum torque is available at zero speed or not. On the contrary, an IC engine is rated at a specific r/min level for maximum torque and maximum hp. The IC engine maximum torque and hp ratings are typically derived under idealized laboratory conditions. In practical situations, it is impossible to achieve the rated hp; the maximum hp available from an IC engine is always smaller than the rated hp. The torque characteristics of motors are shown in Figure 1.5 [9], superimposed with torque characteristics of IC engines. The characteristics of specific motors and IC engines may differ from these generalized curves. For electric motors, a high torque is available at starting, which is the peak torque of the motor. The peak torque is much higher (typically twice) than that of the rated torque. The peak torque for electric motors in an EV application needs to be sustained for about 60 to 90 s [9].

The torque with which the motor can be expected to deliver continuously without over heating is referred to as rated torque [12] while the peak or rated power is obtained at base speed (when motor characteristics enter the constant power region from the constant torque region, once the voltage limit of the power supply is reached) [9]. The motor rated speed (rated) is at the end of the constant power region. The IC engine peak power and torque occur at the same speed. At this stage, it is helpful to review the power and torque relation, which is as presented in Equation 1.1. Power (watts) can be converted to hp by the relation; $1watt = 1.34hp$.

$$Power\ (watts) = Torque(N - m) \times Speed(rad/s) \tag{1.1}$$

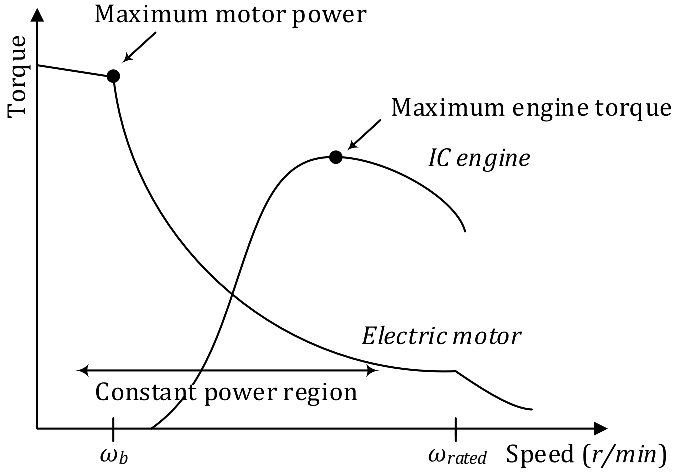

Figure 1.5 Electric motor and IC engine torque characteristics [9]

Vehicle performance usually includes acceleration performance, evaluated by the time used to accelerate the vehicle from zero speed to a given speed (starting acceleration, modelled in Chapter 2), or from a low speed to a given high speed (passing ability) [11]; gradeability, evaluated by the maximum road grade that the vehicle can overcome at a given speed, and the maximum speed that the vehicle can reach. Since in EVs, it is dependent only on the traction motor to deliver torque to the driven wheels, the vehicle performance is completely determined by the torque-speed or power-speed characteristic of the traction motor. From figure 1.5, it can be observed that the EV motor drive is expected to be capable of offering a high torque at low speed for starting and acceleration, and a high power at high speed for cruising. At the same time, the speed range under constant power is desired as wide as possible. For general electric motor drives in industrial applications, their output performances are shown in Figure 1.6a [11] and desired performance in EV application in Figure 1.6b. Under the normal mode of operation, the electric motor drive can provide constant rated torque up to its base or rated speed. At this speed, the motor reaches its rated power limit.

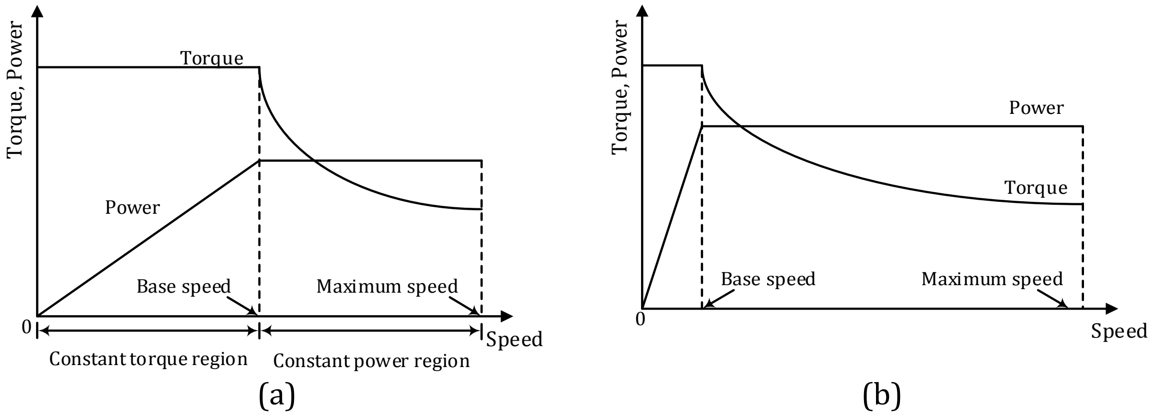

Figure 1.6 Typical performances of electric motor drives (a) performance in industrial applications, (b) desired performance in EV applications [11]

The operation beyond the base speed up to the maximum speed is limited to this constant power region. The range of the constant power operation depends primarily on the particular motor type and its control strategy.

B. EV motor requirements:

The important characteristics of a motor for an EV include flexible drive control, fault tolerance, high efficiency, and low acoustic noise. The motor drive must be capable of handling voltage fluctuations from the source. Another important requirement of the electric motor is acceptable mass production costs, which is to be achieved through technological advancement. The requirements of an EV motor, not necessarily in order of importance, are itemized in the following [9, 11]: *1*) Ruggedness; *2*) High torque-to-inertia ratio; large ratios results in "good" acceleration capabilities; *3*) Peak torque capability of about 200 to 300% of continuous torque rating; *4*) High power-to-weight ratio; *5*) High-speed operation, ease of control; *6*) Low acoustic noise, low electromagnetic interference (EMI), low maintenance, and low cost; *7*) Wide speed range with constant-power region; *8*) Fast torque response; *9*) High efficiency over the wide speed range with constant torque and constant power regions; *10*) High efficiency for regenerative braking; *11*) Downsizing, weight reduction, and lower moment of inertia; *12*) High reliability and robustness for various vehicle operating conditions; *13*) Fault tolerance;

1.1.2 Electrical Machines and Drives for EVs

Every electric vehicle has at least one electric machine, and some have several similar motors working in unison, sharing the load and operating under the same conditions of speed and shaft torque, depending on their drivetrain architecture [1, 13]. The motor responds to the drive control signals fed through the power converter and they both determine the behaviour and characteristics of the propulsion system, the power ratings of the power semiconductors and devices present in the power converter.

As earlier established, the electric machine delivers processed power or torque to the transaxle for propulsion. The machine also processes the power flow in the reverse direction during regeneration, when the vehicle is braking, converting mechanical energy from the wheels into electrical energy. The term “motor” is used for the electric machine when energy is converted from electrical to mechanical, and the term “generator” is used when power flow is in the opposite direction, with the machine converting mechanical energy into electrical energy [9].

Motor drives for EVs can be classified into two main groups, namely the commutator motors and commutatorless motors as illustrated in Figure 1.7 [6]. Commutator motors are traditionally DC machines, DC motor drives have been widely used in applications where dc voltages are available and variable-speed operation, good speed regulation, frequent starting, braking and reversing are required. The DC machines have two sets of windings, one in the rotor and the other in the stator, which establish the two fluxes; hence, the magnetomotive forces (mmfs) that interact with each other produce the torque. The orthogonality of the two mmfs, which is essential for maximum torque production, is maintained by a set of mechanical components called commutators and brushes [9]. They require brushes and commutators to feed current to their armatures making them less reliable and not suitable for maintenance-free operation and high speed [6], they are usually not suitable choices for use in hazardous/explosive environments and are very susceptible to wear and tear [14]. The associated limitation especially due to their commutator and brushes make them a less attractive option for the EV. Compared to DC machines, AC machines have none of these limitations, thus emphasis will be laid on AC machines in EVs.

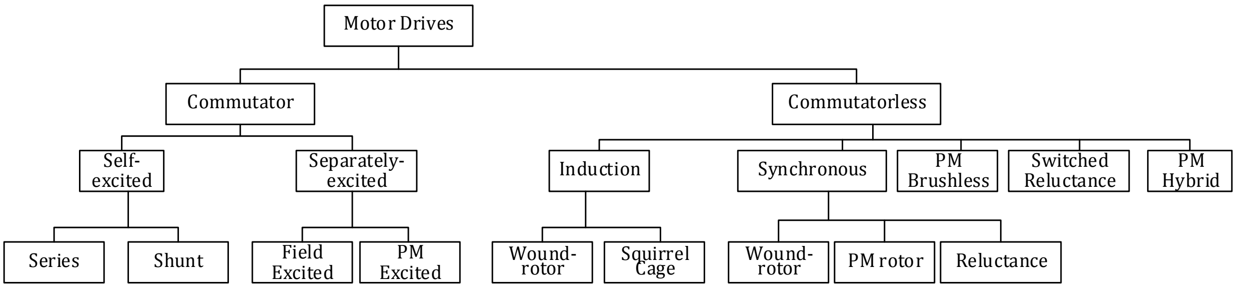

Figure 1.7 Classification of electric motor drives for EV applications [6]

1.1.2.1 AC Machines and Drives

In the DC motor, there exists friction between the brushes and commutator which will cause both to gradually wear down, which is a limitation. Also the heat losses are generated in the middle of the motor (in the rotor) [5]. AC motors are so designed that the heat is generated on the outside (stator) enabling easy cooling, brushes and commutators are also eliminated making it maintenance free and applicable in industrial and volatile environments.

The induction motor (IM) is widely recognized as commutatorless or brushless motor type for EVs [6, 7, 11]. They are reliable, rugged and maintenance free with highly mature and proven technology. Conventional control such as the variable voltage variable frequency control does not provide desired performance in EV applications, but with the advent of power electronics and the microprocessor, vector control techniques such as the field oriented control (FOC) have evolved which have been accepted to overcome the IM control complexities. However, they still suffer from low efficiencies at light loads and limited constant power operating range [6].

By replacing the field windings of a conventional synchronous motor with permanent magnets (PMs), the PM synchronous motor, also referred to as the PM brushless AC motor or sinusoidal-fed PM brushless motor, is obtained. These eliminates slip rings, brushes and field copper losses [15]. When PMs are mounted on the surface of the rotor, they behave as non-salient synchronous motors because the permeability of the magnets is similar to that of air. When PMs are buried inside the rotor magnetic circuit, the saliency causes an additional reluctance torque which facilitates a wider speed range at constant power operation. On the other hand, by neglecting the field windings or PMs, making use only of the rotor saliency, the synchronous reluctance motor (SRM) is obtained. These motors are simple, inexpensive but with relatively low output power. These motors will be introduced here.

A. Induction Motor

The IM is well recognized as the workhorse of industry [16], and most widely used motor [14, 17, 18]. Unlike the DC motor, the IMs derive their name from the way the rotor magnetic field is created. The IM rotor current is induced by the induction between the stator and rotor windings. These interaction produces torque, which is the useful mechanical output of the machine. The bars forming the conductors along the rotor axis linked at their ends. Sinusoidal stator phase currents fed into the stator coils create a magnetic field rotating at the speed of the stator frequency (ω_s). The changing field induces a current in the cage conductors, which results in the creation of a second magnetic field around the rotor conductors. As a consequence of the forces created by the interaction of these two fields, the rotor experiences a torque and starts rotating in the direction of the stator field.

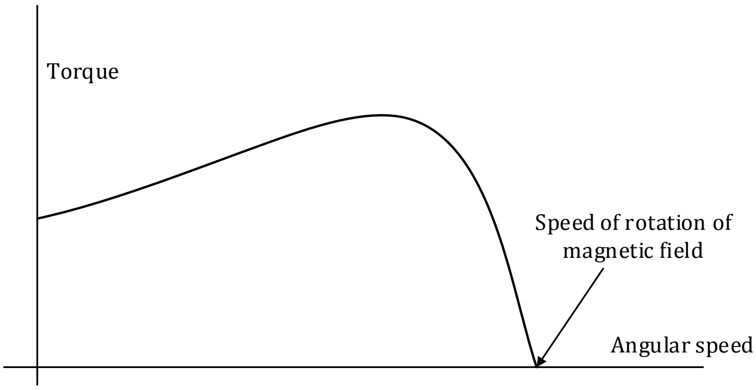

Figure 1.8 Typical torque/speed curve for an induction motor [5]

As the rotor begins to speed up and approach the synchronous speed of the stator magnetic field, the relative speed between the rotor and the stator flux decreases, decreasing the induced voltage in the stator and reducing the energy converted to torque. This causes the torque production to drop off, and the motor will reach a steady state at a point where the load torque is matched with the motor torque. This point is an equilibrium reached depending on the instantaneous loading of the motor. Figure 1.8 illustrates the torque-speed graph for an IM. Control strategies include: *1*) *Constant volts/hertz control*, a scalar control method in which the flux is kept constant by keeping the ratio between the stator voltage and frequency constant. This technique is explained later on in this work; *2*) *Field Orientation Control (FOC):* Depending on the EV design considerations and type the performance of the volt/hertz scheme may not be satisfactory, this is because it is more suitably applied to motors that operate with slow speed regulation. However, this approach shows poor response to frequent and fast speed varying resulting in poor operating efficiency due to poor power factor [6]. The concept of field orientation was proposed by Hasse in 1969 and Blaschke in 1972 [17]. Generally speaking, the objective of FOC is to make the IM emulate the separately excited dc machine to always produce adjustable or maximum torque [6, 17]. It relies on the dynamic analysis of IMs in terms of *dq*-windings (analysed in chapter 3). The general block diagram of a vector control system for an IM is shown in Figure 1.9. A field orientation system produces reference signals i^*_{as}, i^*_{bs}, and i^*_{cs}, of the stator currents, based on the input reference values, i^*_{as} and T^*, of the rotor flux and motor torque respectively and the signals corresponding to selected variables of the motor. An inverter supplies the motor currents i_{as}, i_{bs}, and i_{cs}, such that their waveforms follow the reference waveform, i^*_{as}, i^*_{bs}, and i^*_{cs}.

Other control methods such as the sensorless control techniques which decouple the torque and flux, combined with the use of observers [19, 20] to achieve desired control objectives, rotor position control by quadrature inversion (QI) technique [21] that eliminates the decoupling problems and the need for torque controllers, are well documented in literature.

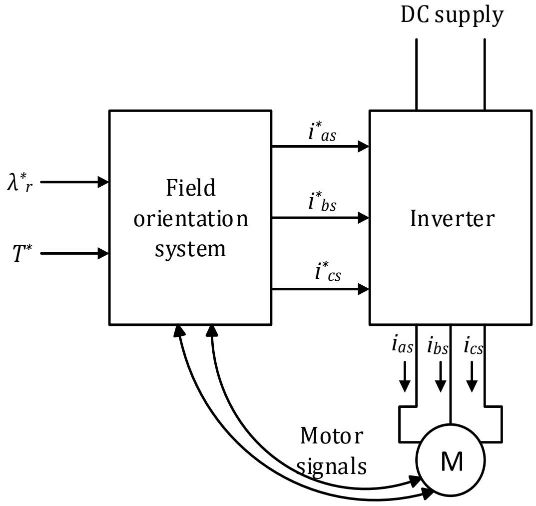

Figure 1.9 General block diagram of a vector control system for an induction motor [6].

B. Permanent Magnet Brushless DC Motor (PM BLDC)

It was earlier explained that by using high-energy PMs as field excitation mechanisms, one can achieve a drive with high power density, high speed and high operating frequency, these advantage makes it quite attractive for EV applications. Pros and cons associated with BLDC motors is shown in Table 1.1.

Table 1.1 Advantages and disadvantages of BLDC motors

Advantages	*Disadvantages*
High efficiency: BLDC motors are very efficient, the PMs used for excitation consume no power, absence of mechanical brushes and commutators also imply low mechanical friction losses	*Cost*: Rare-earth magnets are very expensive and increases cost implications of the machine considerably.
Compactness: BLDC motors have the advantage of being small and light because of the recent introduction of high density rare-earth magnets [6] achieving high flux densities, thus high torque.	*Safety*: They are not easy handle due to very large forces that come into play when anything ferromagnetic gets close to them [22], also, in the case of a vehicle wreck and the wheel is spinning freely, the motor is still excited by the magnets and high voltages could be present [6].
Ease of control: The BLDC motor can be controlled easily as a DC motor, the control variables are constant throughout operation of the motor	*Magnet demagnetization*: Magnets can be demagnetized by large opposing mmfs and high temperatures.
Ease of cooling: No current circulation in the rotor, hence it does not heat up, the only heat generates in on the stator which is easier to cool.	*High-speed capabilities*: Surface-mounted PM motors cannot achieve high speeds because of the limited mechanical strength between the rotor yoke and PMs
Low maintenance, great longevity and reliability: The absence of commutators and brushes suppresses the need for maintenance and risk of failure associated with these elements. The longevity is only a function of winding insulation, bearings and magnet life-length.	*Inverter failures in BLDC motor drives*: Because of the PMs on the rotor, they pose a major risk in the case of short-circuit failures of the inverter. The rotating rotor is always energized, constantly inducing large EMFs in the short-circuited windings. Large current circulates in those windings and according large torque tends to block the rotor [6].
Low noise: There is no noise associated with the commutation because it is electronic and not mechanical, switching frequencies are high enough so that the harmonics are not audible.	

Figure 1.10a shows the simplified equivalent circuit for the BLDC motor and their speed-torque curves in steady state with constant and variable voltage supplies, where V_t is the voltage of the power supply, R_s is the resistance of the winding, L_s is the leakage inductance ($L_s = L_l - L_m$, where L_l is the self-inductance of the winding and L_m the mutual inductance), and E_s is the back EMF induced by the winding of the rotating motor. Based on the equivalent circuit of Figure 1.10a, the performance of the BLDC can be described by the following equations [6]:

$$V_t = R_s I_s + L_s \frac{dI_s}{dt} + E_s \tag{1.2}$$

$$E_s = k_E \omega_r \tag{1.3}$$

$$T_e = k_T I_s \tag{1.4}$$

$$T_e = T_L + J\frac{d\omega_r}{dt} + B\omega_r \tag{1.5}$$

where k_E is the back EMF constant associated with the PMs and rotor structure, ω_r is the angular velocity of rotor, k_T is the torque constant, T_L is the load torque and B is the viscous resistance coefficient.

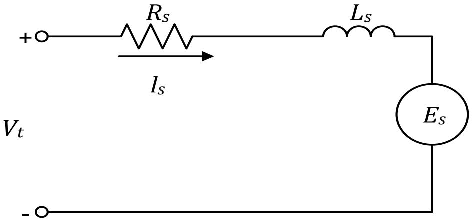

(a) *Equivalent circuit of BLDC motor*

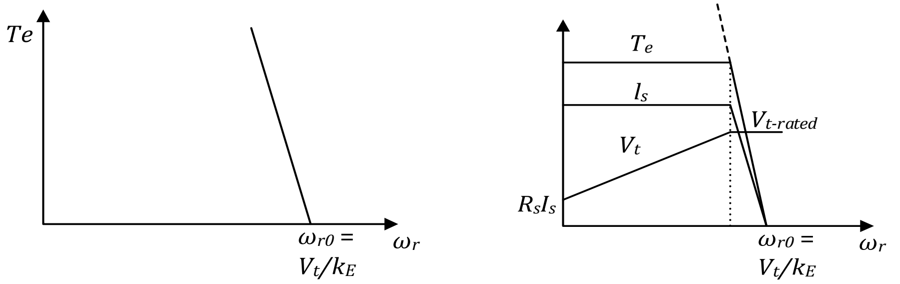

(b) speed-torque performance with constant voltage

(c) speed-torque performance with constant voltage

Figure 1.10 BLDC motor circuit and speed-torque curves [6]

For steady state operation, Equations 1.2 to 1.4 can simply be reduced to

$$T_e = \frac{(V_t - k_E\omega_r)k_T}{R_s} \tag{1.6}$$

The speed-torque performance with constant voltage is shown in Figure 1.10b, it is noticeable that at starting, very high torque is produced resulting in high currents due to low back EMF (this would damage the stator windings). The speed-torque performance with variable voltage is shown in Figure 1.10c, here the winding current can be restricted to its maximum by actively controlling the voltage; thus maximum torque can be produced.

C. SRM Drives

The SRM drive is considered a competitor for EV applications, due to its low cost rugged structure, reliable converter topology, higher efficiency over wide speed ranges and control ease, it is an attractive candidate for variable speed motor drives. These drives are suitable for EVs, HEV traction applications, aircraft starter/generator systems, door actuators, etc. [23, 24]. The SRM has a simple rugged, low cost structure with no PM or windings on the rotor. Unlike the IM and PM machines, the SRM is capable of high –speed operation without the concern of mechanical failures that result from high-level centrifugal force [6].

A conventional SRM drive, illustrated in Figure 1.11 consists of the SRM, power inverter, sensors (voltage, current, position, etc.) and control circuitry. Through proper control, high performance can be achieved in the SRM drive system.

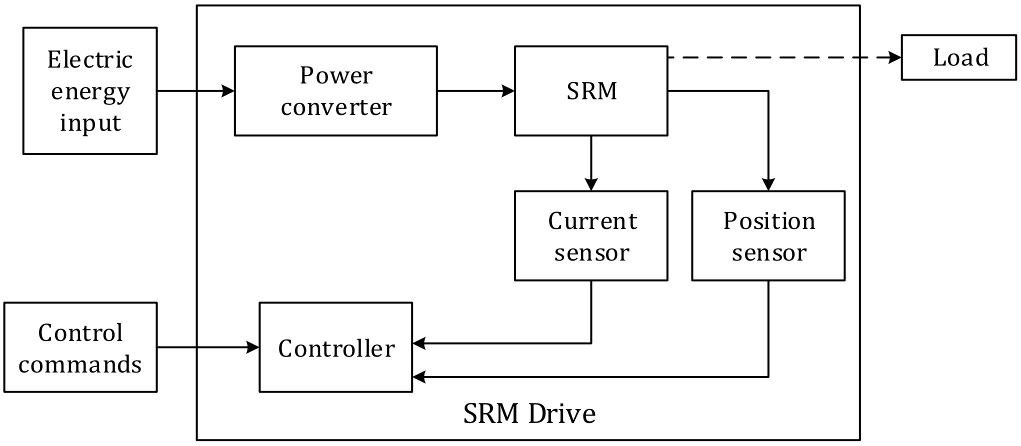

Figure 1.11 SRM drive system [6].

Control of SRM Drives: Excitation of the SRM phases needs to be properly synchronized with the rotor position for effective control of speed, torque and torque pulsation. Shaft position sensors are usually used to provide rotor position but this adds to the complexity and cost of the system and tends to reduce the reliability of the drive system. Sensorless control strategies can be employed to solve this problem and are reported in literature. Some of them are the phase flux linkage-based method [25], phase inductance-based method [26], modulated signal injection methods [23, 27, 28], observer-based methods [29] among others. Most of these techniques are based on the fact that the magnetic status of the SRM is a function of the angular position of the rotor. As the rotor moves from the unaligned position towards the aligned position, the phase inductance increases from the minimum value to the maximum value [6]. Some sensorless techniques do not use the magnetic characteristics or voltage equations, rather they are based on observer theory or synchronous operation method similar to that applied to conventional AC machines.

1.1.2.2 A Case for the Induction Motor

There is no general consensus as to the type of electric machine best suited for vehicles, according to [13]. Table 1.2 compares four types of electric motor drives listing weight factors in efficiency, weight, and cost of four types of motor drives, where 5 marks represent the highest efficiency, lowest weight, and lowest cost, respectively.

Table 1.2 Comparison of four types of electric motor drives [11]

Index	DC motor drives	IM drives	PM BLDC motor drives	SRM drives
Efficiency	2	4	5	4.5
Weight	2	4	4.5	5
Cost	5	4	3	4
Total	9	12	12.5	13.5

The SRM seems to have the edge in EV applications, they have the simplest design but these machines are generally extremely noisy during operation, have higher torque pulsations and the design has not been advanced to the same extent as the PM or induction motor [30]. However, they are applied in heavy-duty vehicles and research is in progress to apply them in light-weight vehicles [13]. The induction and permanent magnet machines are the two types currently used in EVs and are expected to dominate the market. Table 2.1 highlighted the advantages and disadvantages of the PM. The major disadvantage lies in the soaring price and supply disruptions of magnets due to geopolitical issues [13, 30], hence they are not readily available and expensive.

Table 1.3 easily helps in the choice of motor, it shows information for electric cars produced (for commercial purposes) and for prototype or experimental versions. The induction has been successfully applied in production vehicles as seen in Table 1.3. One cannot help but notice the dominance of the IM in prototype vehicles (Table 1.4) implying its low cost, mature technology and ability to meet vehicle propulsion requirements.

The motor is a part of the propulsion system required in EV, as discussed in earlier, it provides traction power to the wheels required for moving the vehicle. Taking advantage of electric motors in vehicles could help design more compact, lightweight efficient drivetrains.

Several types of electric machine technologies have been investigated for automotive propulsion. Most of the commercially available electric vehicles use either induction or PM machines for propulsion and are expected to dominate the market [13, 30]. In this research work, the induction motor (IM) was selected as choice of propulsion motor. As discussed above, it meets the propulsion requirements for electric vehicles. At present, IM drives are among the more mature technology in commutatorless motor drives. Compared with DC motor drives, the induction motor drive has additional advantages such as lightweight, small volume, low cost, high efficiency [6], capable of substantially higher speeds than DC motors [8]. Induction machines are a better option over PM machines when you consider the cost of magnetic components in the motor and supply disruptions of magnets due to some recent geopolitical issues [30]. Conventional induction motors use aluminium rotors, however, electrical conductivity of copper is 60% more than aluminium, using copper can also reduce the motor operating temperature by 5-32^{0}C, suggesting increased life-time [13, 30].

At this juncture, it should be noted that the term “induction machine” and “induction motor” are used interchangeably in this report.

Table 1.3 Production electric cars [8]

Manufacturer	Citroen	Daihatsu	Ford	GM	GM	Honda	Nissan	Nissan	Nissan	Peugeot	Renault
Model name	AX/Saxo Electrique	Hijet EV	Th!nk City	EV1	EV1	EV Plus	Hypermini	Altra EV	106 Electric	Clio Electric	RAV4
Drive type	Seperately excited DC	PM synch	IM	IM	IM	PM synch	PM synch	PM synch	Separately excited DC	PM synch	PM synch
Max power O/P (kW)	20		27	102	102	49	24	62	20	22	50
Top speed (km/h)	91	100	90	129	129	129	100	120	90	95	125
Claimed max range (km)	80	100	85	95	130	190	115	190	150	80	200

Table 1.4 Prototype and experimental electric cars [8]

Manufacturer	BMW	Daimler Chrysler	Daimler Chrysler	Fiat	Ford	Ford	GM	GM	Lada	Mazda	Mazda	Peugeot	Toyota
Model name	BMW Electric	Zytek Smart EV	A-Class Electric	Seicento	Th!nk Neighbor	e-Ka	Impulse3	Impulse3	Rapan	Roadster-EV	Demio-EV	Ion	E-com
Drive type	PM Synch	BLDC	IM	IM	DC	IM	2x3 Ø IM	2x3 Ø IM	Separately Excited DC	AC	PM Synch	Separately excited DC	PM Synch
Max power O/P (kW)	45	30	50	30	5	65	45	42		30		20	19
Top speed (km/h)	130	97	130	100	40	130	120	120	90	130			100
Claimed max range (km)	155	160	200	90	48	150	80	150	100	180		150	100

1.2 Motivation and Purpose

The vehicle is a very dynamic environment subjected to different conditions such as, varying road profiles/conditions, vibrations, high temperatures, exposure to the elements, among other factors, impressing stress on the materials and components that make up the system. The components in the electric vehicle will be subjected to these conditions and are expected to perform as desired. As mentioned earlier, the propulsion system is the heart of the electric vehicle, hence, adequate choice and high performance control of the electric motor (in this case the induction motor) invariably results in high performance and efficiency of the electric vehicle. Efforts are to find suitable control strategy that will not only optimize available energy but provide smooth, precise and efficient control of the IM in all four quadrants. Actually, the idea is to ensure the driver does not have to "learn" to drive the vehicle, it responds to normal driving actions such as accelerating, reversing and braking. It is for the designer to implement control methods for smooth operation of the IM.

The Variable Structure System (VSS) Sliding Mode(SM) technique will be employed in the Direct Torque Control (DTC) of encoder-less IM drive. This reduces the cost of the drive system and provides high performance control of the IM considering the continually varying load conditions in the system, interferences and disturbances. Objectives of this research is discussed next.

1.3 Objectives of the Study

Two control methodologies for the IM will be investigated: the constant volts/hertz (*v/f*) and the direct torque control (DTC) methods. The objective is to design a SM – based DTC, first, the design and implementation of *v/f* will be discussed and its model results presented and then compared with that of the DTC. The performances of these schemes will be evaluated, compared and conclusions will be drawn from the results.

Thus, the main objective of this study, which is the contribution of this thesis, is to develop encoder-less operation of a Sliding Mode Direct Torque Controlled IM drive suitable for application in electric vehicles. In order to achieve this, the main objective is broken down to the following sub-objectives:

1) Analysis and modelling of the electric vehicle.
2) Mathematical analysis of the Induction Motor.
3) Design and implementation of the v/f control strategy for the Induction Motor.
4) Development of sliding mode direct torque control (SM-DTC) strategy and algorithm for the Induction Motor.
5) Performance comparisons and inference between the v/f and DTC.

1.4 Scope of the Study

The study of electric vehicles is vast, embodying different disciplines. This work centres on control strategies for propulsion of an electric vehicle. The performances of the v/f and DTC schemes will be evaluated and compared, but the core of the research is to establish the SM-DTC strategy for the motor providing tractive power to the wheels. Other components such as vehicle body shape, chassis, gearing, battery, charging units, tire specifications, nature of terrain will not be given preference or priority. They will be mentioned where necessary for completion.

1.5 Organization of the Thesis

This thesis is divided into 7 chapters, brief overview of these chapters are presented below:

- **Chapter 2:** Preliminary concepts are explained. Basic concepts of electric vehicle, propulsion systems and vehicle modelling are presented, including various electric machines deployed in EV drives and a case is made for the induction motor. Also, control of induction machines, v/f, VSS and DTC is introduced.

- **Chapter 3:** The mathematical analysis of the induction motor in different coordinates and using space vectors is presented. These equations are a requirement for the development of the control techniques and observers for the SM-DTC scheme discussed in later chapters.
- **Chapter 4:** A review of scalar control methods and schemes of IM is discussed. The v/f control strategy, operating principles, equations and system design are presented. Behaviour of the IM under this technique is also presented and compared with VSS control.
- **Chapter 5:** DTC methodology is discussed and application of VSS theory is applied for improved performance. Mathematical equations are also developed.
- **Chapter 6:** The simulation results of the encoder-less DTC scheme is discussed and compared to the experimental and simulated v/f control.
- **Chapter 7:** A summary is presented, conclusions from the research work are drawn and scope of future work is outlined.

Chapter 2

2 Preliminary Concepts

2.1 Modelling the EV

Computers are very useful tools for modelling real world systems. Mathematical models will be developed for the dynamics of the EV. During simulation, effects of varying the model parameters can be seen as it affects acceleration, top speed, motor sizing, vehicle range, etc. Data produced from the model equations will be used to predict vehicle behaviour.

A. *Tractive Effort*

Consider a vehicle of mass m, moving at a velocity v up a slope of angle α_g as shown in Figure 2.1. The force propelling the vehicle forward has to accomplish the following:

i. Overcome rolling resistance,

ii. Overcome aerodynamic drag,

iii. Provide the force needed to overcome the vehicle's weight acting down the slope,

iv. Accelerate the vehicle if the velocity is not constant.

Considering each of these in turn:

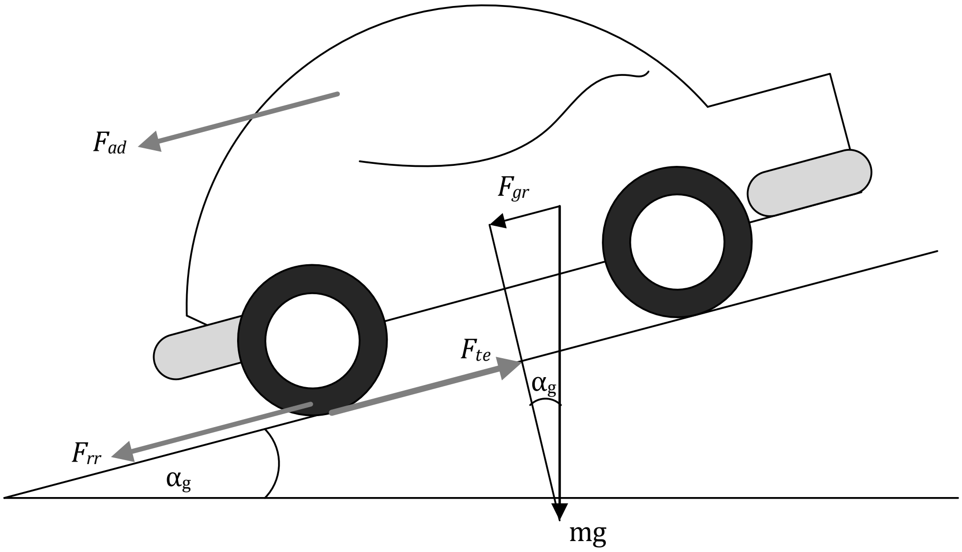

Figure 2.1 Forces acting on a vehicle moving up a slope

Rolling Resistance: This is primarily due to hysteresis loss in the vehicle tyres [5, 6, 31]. According to [5], rolling resistance is approximately constant and hardly depends on vehicle speed. It is dependent on vehicle weight and expressed by the equation:

$$F_{rr} = \mu_{rr} mg \tag{2.1}$$

where μ_{rr} is the coefficient of rolling resistance, which is a function of tire material, tire structure, tire temperature, tire inflation pressure, tread geometry, road roughness, road material, and presence or absence of liquids on the road [6].Equation (2.7) is valid for flat surfaces, when the EV is operated on a slope, the normal load (mg) should be replaced by the component perpendicular to road surface ($mgcos\alpha_g$). Table 2.1 [32] shows typical values of rolling resistance on various roads obtained by experimental and empirical methods.

Table 2.1 Rolling resistance coefficients

Conditions	Rolling Resistance Coefficient, μ_{rr}
Car tires on concrete or asphalt road	0.013
Car tires on rolled gravel road	0.02
Tar macadam road	0.025
Unpaved road	0.05
Field	0.1 – 0.35
Truck tire on concrete or asphalt road	0.006 – 0.01
Wheels on iron rail	0.001 – 0.002

Aerodynamic Drag: This can be described as the resistance offered to a vehicle body moving at a particular speed through the air. It is a function of vehicle speed u, vehicle frontal area A, shape of the vehicle body and air density ρ:

$$F_{ad} = \frac{1}{2}\rho A C_d u^2 \tag{2.2}$$

where C_d is a constant known as aerodynamic drag coefficient that characterizes the shape of the vehicle body. C_d can be reduced by good vehicle design. Typical values for saloon cars is between 0.25 and 0.4 [6], for some vehicles such as motorcycles or buses it can be up to 0.7 [5]. The density of air varies with temperature, altitude and humidity, however a value of 1.25kg/m^{-3} is a reasonable value to use in most cases. The value of F_{ad} is given in Newton provided SI units are used (m^2 for A, ms^{-1} for u)

Hill Climbing Force: Also referred to as grading resistance, this is the force needed to drive a vehicle up a slop. It is simply the component of the vehicle weight that acts along the slope. By resolving the forces acting on the EV in Figure 2.10, the following expression can be obtained:

$$F_{gr} = mg\, sin\, \alpha_g \tag{2.3}$$

Acceleration Force of the Vehicle: If the velocity is changing, then additional force will need to be applied in addition to the forces in Figure 2.1. This force will provide linear acceleration of the vehicle and is derived from Newton's third law:

$$F_{la} = ma \tag{2.4}$$

However, for completeness and accuracy of the forces needed to accelerate the vehicle, the forces required to make the rotating parts turn faster need to be considered i.e. rotational and linear acceleration. Referring to Figure 2.2, the axle torque equal $F_{te}\cdot r$, where r is radius of the tire and F_{te} is the tractive effort delivered to the powertrain. If G is the gear ratio of the system connecting the motor to the axle and T is the motor torque, it can be said that [5]:

$$T = \frac{F_{te} r}{G} \;\; so\ that\;\; F_{te} = \frac{G}{r} T \tag{2.5}$$

This equation will be useful when developing final equations for the vehicle performance.

It should be noted that axle angular speed is u/r radians per second, so motor angular speed is:

$$\omega = G\frac{u}{r} rad\ s^{-1} \tag{2.6}$$

and, similarly motor angular acceleration is:

$$\dot{\omega} = G\frac{a}{r}\ rad\ s^{-2} \tag{2.7}$$

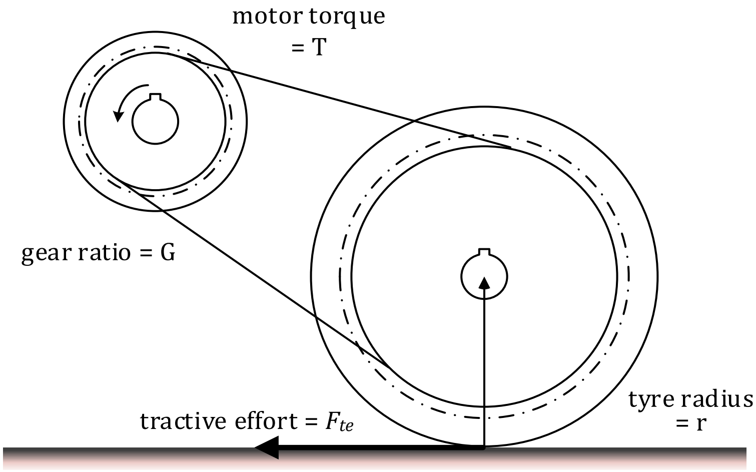

Figure 2.2 A simple arrangement for connecting a motor to a drive wheel [5].

Torque required for this angular acceleration is:

$$T = J \times G\frac{a}{r} \tag{2.8}$$

where *J* is the moment of inertia of the rotor of the motor. The force at the wheels needed to provide angular acceleration $F_{\omega a}$ is found by combining Equations (2.5) and (2.8), giving

$$F_{\omega a} = \frac{G}{r} \times J \times G\frac{a}{r} \equiv F_{\omega a} = J\frac{G^2}{r^2}a \tag{2.9}$$

Note that for this simple equation, it is assumed that the gear system is 100% efficient, it causes no loss. The equation can be refined to incorporate gear system efficiency η_g. The force required will be slightly larger. Hence, Equation (2.9) becomes:

$$F_{\omega a} = J\frac{G^2}{\eta_g r^2}a \tag{2.10}$$

For the purpose of modelling, typical values will be used, the following example is obtained from Ref *[5]*. Typical values for the constants here are 40 for *G/r* and 0.025kgm^2 for *J*. These are for 30kW motor, driving a car reaching 60kph at motor speed of 7000rpm. Such a car would probably weigh 800kg. The JG^2/r^2 term in Equation (2.10) will have a value of about 40kg in this case. Implying that the angular acceleration force in Equation (2.10) will typically be much smaller than the linear force in Equation (2.4). In this specific (but reasonably typical) case, it will be smaller by the ratio

$$\frac{40}{800} = 0.05 = 5\%$$

Often, it turns out that the moment of inertia of the motor J will not be known, in such cases, a reasonable approximation is to simply increase the mass by 5% (in this case) in Equation (2.4) and ignore the $F_{\omega a}$ term.

The total tractive effort F_{te} is the sum of all these forces.

$$F_{te} = F_{rr} + F_{ad} + F_{gr} + F_{la} + F_{\omega a} \tag{2.11}$$

where

F_{rr} = rolling resistance force, given by Equation (2.1)

F_{ad} = aerodynamic drag, given by Equation (2.2)

F_{gr} = grading resistance force, given by Equation (2.3)

F_{la} = force required to give linear acceleration, given by Equation (2.4)

$F_{\omega a}$ = force required to give angular acceleration to the rotating motor given by Equation (2.10)

Note that F_{la} and $F_{\omega a}$ will be negative if vehicle is slowing down and F_{gr} will be negative if vehicle is going downhill.

In case of the EV, the relation between vehicle speed (m/s) to motor speed (rpm) is given by [6, 33]:

$$u = \frac{\pi N_m r}{30 G \eta_g} \tag{2.12}$$

where, N_m is the transmission rotating speed (rpm).

To determine the electric battery capacity, we need to estimate energy required of EV platform, the requested power, P_{te} in kW that the EV platform must develop at stabilized speed can be determined by multiplying the total force with the speed of the EV, and given by [34]:

$$P_{te} = F_{te} \times u \tag{2.13}$$

This equation can be used to estimate the total power required for propelling the EV and thus determine the induction motor power requirements. The total tractive effort obtained in Equation (2.11) becomes the torque introduced into the motor as a reference.

Parameters used to model the acceleration and distance covered for the electric vehicle designed in the Department of Electrical Engineering Laboratory, are shown on Table 2.2.

Table 2.2 EV model parameters

Aerodynamic drag coefficient, C_d = 0.25	Coeffiicient of rolling resistance u_{rr} = 0.013
Gear ratio 11:1, $G = 11$	Tyre radius, r = 0.30m
Frontal area, A = 1m^2	Efficiency of gear coupling η_g = 0.90
Estimated vehicle mass =1000kg	IM type
Battery weight (25kg each) for 10 batteries = 250kg	20hp = 15kW
	Full load torque = 29.8lb-ft = 39N-m
Passengers (4) at 70kg each = 280kg	Full load RPM = 3525
Total vehicle load = 1530kg	*only relevant data are listed

The model is for the EV on a flat surface. The MATLAB® code is presented in Appendix A. Figure 2.3 shows the acceleration of the EV, it can be seen that the time taken to reach 60kph is about 25.5 seconds, might seem slow but this is compatible with safe city driving. The model assumes that beyond 16.6ms^{-1} the controller limits the acceleration of the vehicle. Figure 2.4 shows the total distance travelled within the period.

Thus, the developed equations can be computed and simulated using MATLAB® to obtain predictions for the vehicle performance, acceleration, range, motor power, torque, efficiency even current out of (or into) the battery.

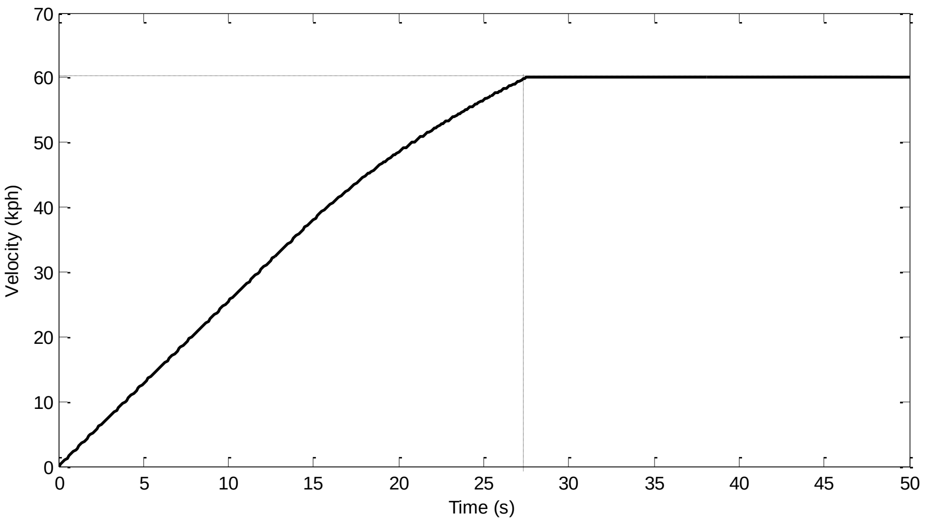

Figure 2.3 Graph showing the acceleration of a design of electric vehicle, being the solution of model with a 0.1 second time step

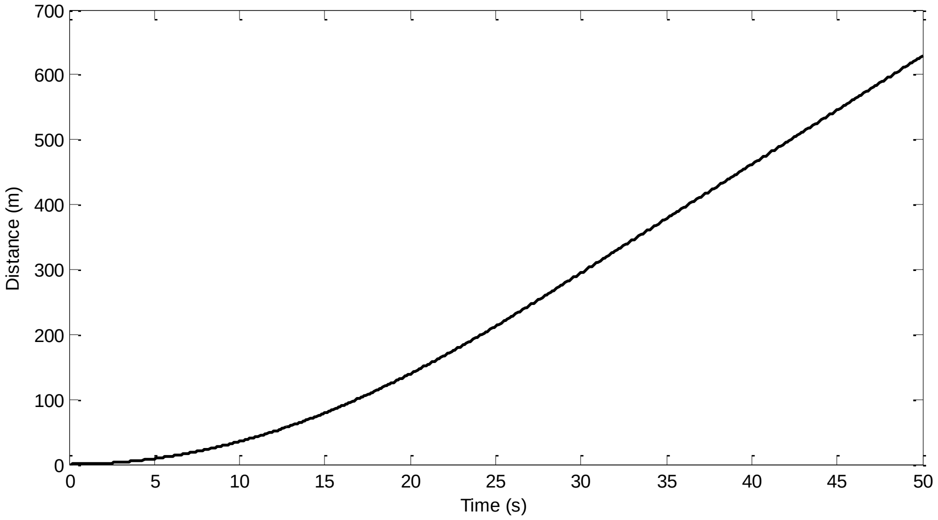

Figure 2.4 Distance/time graph for the electric vehicle, showing the distance versus time from a standing start

2.2 Induction Motor Control

Many control algorithms and methods have been developed for the induction motor for application in electric vehicles [35, 36, 37, 38, 39, 40] such as the v/f control both open loop and closed loop with slip regulation to improve its performance Some v/f control schemes are also implemented with the aid of space vector modulation and even direct torque control. These combinations improves the overall control system. The advancement in microprocessors and microcomputers have made vector control techniques realizable. For example, dynamic analysis of the IM, decoupling of flux and machine torque, etc., can be computationally intensive and is a mandatory requirement for vector control. Faster torque response of the IM is achieved through field oriented control, which is a vector control technique for high performance applications. There are various techniques for the implementations of the FOC along with sensors and observers to further increase its precision. There is also the sensorless or encoder-less variant of IM control where the sensed parameters are estimated by computational knowledge of the motor characteristics. Sliding mode control [36] is also gaining recognition in IM drives because of its performance stability even in the presence of perturbations. In error feedbacks, it is particularly efficient and usually applied in combination with other control methods to achieve near zero error. Discussing all of these control is beyond the scope of this report, in achieving the objective of this research, three control methodologies, *v/f*, SMC and DTC are taken into consideration and are discussed in the following sub-sections.

2.2.1 *V/f* Control

This scheme is sometimes called the scalar control because it focuses only on the steady state dynamic. A simple per phase equivalent circuit model of an IM is a very important tool for the analysis and prediction at steady-state condition. The synchronously rotating air gap flux wave generates a counter emf V_m which is then converted to slip voltage $V_r' = nSV_m$ in rotor phase, where n = rotor-to-stator turns ratio and S = per unit slip. The stator terminal voltage V_s differs from voltage V_m by the drops in stator resistance R_s and stator leakage inductance L_{ls}. The excitation current I_0 consists of two components: a core loss component $I_c = V_m/R_m$ and a magnetizing component $I_m = V_m/\omega_e L_m$, where R_m = equivalent resistance for core loss and L_m = magnetizing inductance. The rotor-induced voltage V_r' causes rotor current I_r' at slip frequency ω_{sl}, which is limited by the rotor resistance R_r' and the leakage reactance $\omega_{sl}L_{lr}'$. The stator current I_s consists of excitation component I_0 and the rotor reflected current I_r. Figure 2.5a shows the development of a per phase transformer-like equivalent circuit and 2.5b shows the equivalent circuit with respect to the stator [16].

In the *v/f* control, the speed of induction motor is controlled by simultaneously adjusting the magnitude of stator voltages and frequency in such a way that the air gap flux is always maintained at the desired value at the steady-state. This principle is explained thus: Assume the voltage applied to a three phase IM is sinusoidal and neglect the voltage drop across the stator resistor. Then, at steady state, with the equivalent circuit further simplified to that shown in Figure 2.5c. Since resistor R_s is assumed to be zero, V_s is equal to V_m, thus:

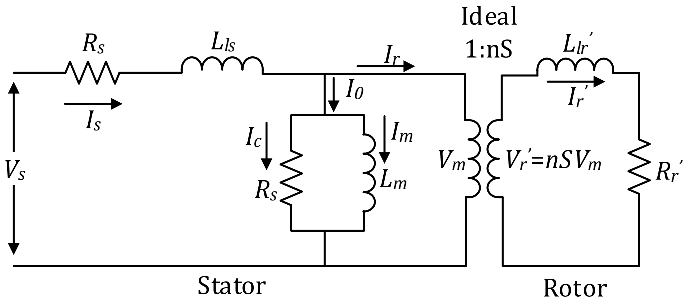

(a) Equivalent circuit with transformer coupling

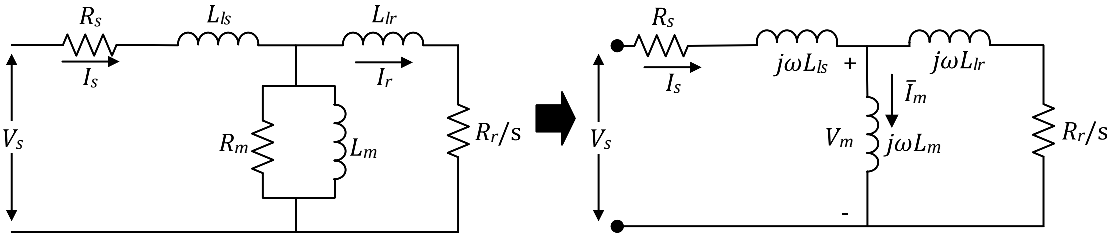

(b) Equivalent circuit with respect to the stator

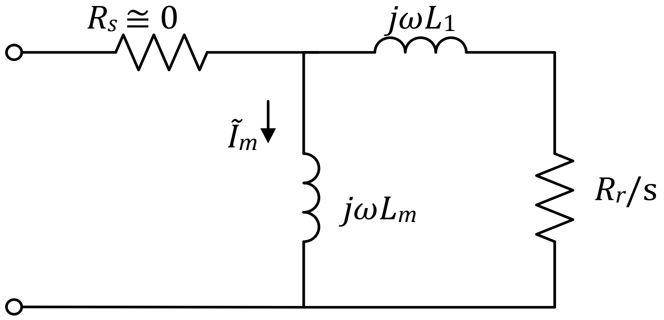

(c) Simplified steady-state equivalent circuit of IM

Figure 2.5 Steady-state equivalent circuit of IM

$$\tilde{V}_s = \bar{I}_m j\omega L_m \qquad (2.14)$$

where $\tilde{V}_s$ is the stator voltage phasor.

Let $\bar{I}_m L_m = \hat{\lambda}_s$ represent the stator flux phasor, it then follows that,

$$\tilde{V}_s = j\omega\hat{\lambda}_s \qquad (2.15)$$

i.e. $V = \omega\lambda_s$, where $\hat{V}$ and $\hat{\lambda}_s$ are the phasors of stator voltage and stator flux and V and λ_s are their magnitudes.

So that,

$$\lambda_s \approx \frac{V}{\omega} = \frac{1}{2\pi}\frac{V}{f} \qquad (2.16)$$

from which it follows that if the ratio v/f remains constant with the change in f then flux (λ_s) remains constant too and the torque is independent of the supply frequency. In actual implementation, the ratio between the magnitude and frequency of the stator voltage is usually based on the rated values of these variables, or motor ratings. However, when the frequency and hence also the voltage are low, the voltage drop across the stator resistance cannot be neglected and must be compensated. At frequencies higher than the rated value, the constant V/Hz principle have to be violated because, to avoid insulation break down, the stator voltage must not exceed its rated value. This principle is illustrated in Figure 2.6 showing the typical V/Hz profile.

Basically, there are three speed ranges in the v/f profile.

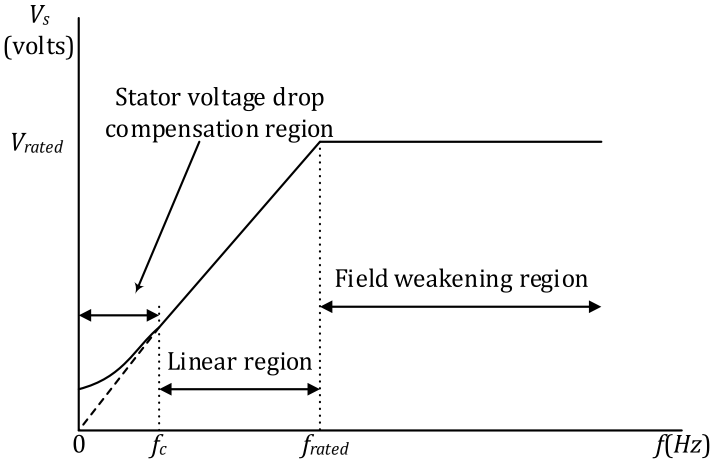

Figure 2.6 Operating variables varying with motor speed under Volt/Hertz control [18].

At 0-fc Hz, a voltage is required, so the voltage drop across the stator resistance cannot be neglected and must be compensated for by increasing the V_s. So, the v/f profile is not linear. The cut-off frequency (f_c) and the suitable stator voltages may be analytically computed from the steady-state equivalent circuit with $R_s \neq 0$ (Figure 2.6). At $f_c - f_{rated}$ Hz, it follows the constant v/f relationship. The slope actually represents the air gap flux quantity as seen in Equation 2.16. At higher f_{rated} Hz, the constant v/f ratio cannot be satisfied because the stator voltages would be limited at the rated value in order to avoid insulation breakdown at stator windings. Therefore, the resulting air gap flux would be reduced, and this will unavoidably cause the decreasing developed torque correspondingly. This region is usually called the “field weakening region”.

Since the stator flux is constantly maintained (independent of the change in supply frequency), the torque developed depends only on the slip speed. This is shown in Figure 2.7. By regulating the slip speed, the torque and speed of an induction motor can be controlled with the constant v/f principle.

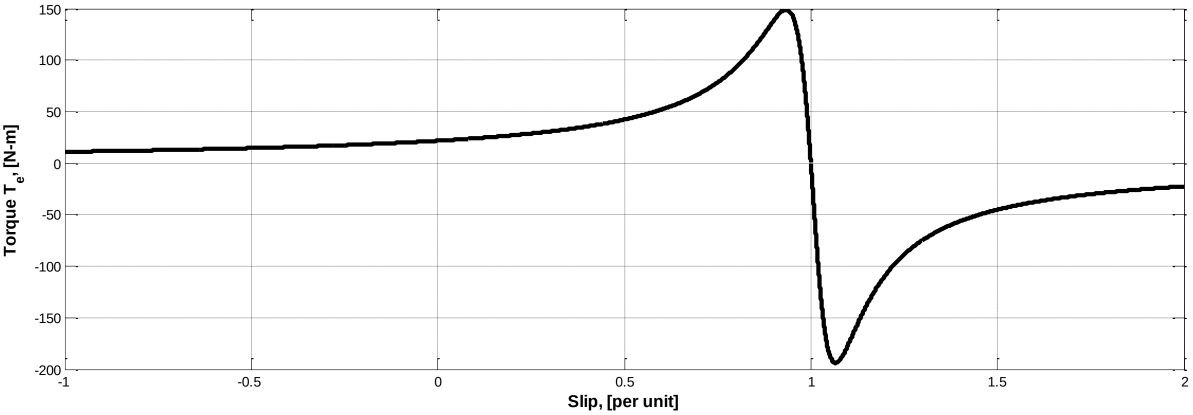

Figure 2.7 Torque versus slip speed of an induction motor with constant stator flux

For constant volt/hertz control of an induction motor, one method is to implement sinusoidal pulse width modulation [41, 42], harmonic control [2, 43], also microcontrollers are useful tools in accomplishing this strategy [19, 20, 21, 44]. Some of these will be discussed in detail in Chapter 4.

2.2.2 Encoderless Direct Torque Control

DTC was developed more than two decades ago by Japanese and German researchers [45]. Instantaneous torque control yielding fast torque response can be obtained by employing this scheme.

In a DTC drive, flux linkage and electromagnetic torque are controlled directly and independently by the selection of optimum inverter switching modes. The selection is made to restrict the flux-linkage and electromagnetic torque errors within the respective torque and flux hysteresis bands to obtain fast torque response, low inverter switching frequency and low harmonic losses. Unlike vector-control techniques, the DTC scheme requires no *dq*-axis transformation and the electromagnetic torque and the stator flux are estimated and directly controlled by applying the appropriate stator voltage vector. It is possible to estimate the rotor speed thus eliminating the need for rotor speed encoder. Figure 2.8 shows the schematic of a simple form of DTC IM drive which uses the stator flux-linkages, thus referred to as stator flux-based DTC IM drive. Other forms are also possible based on rotor flux linkages or magnetizing flux linkages.

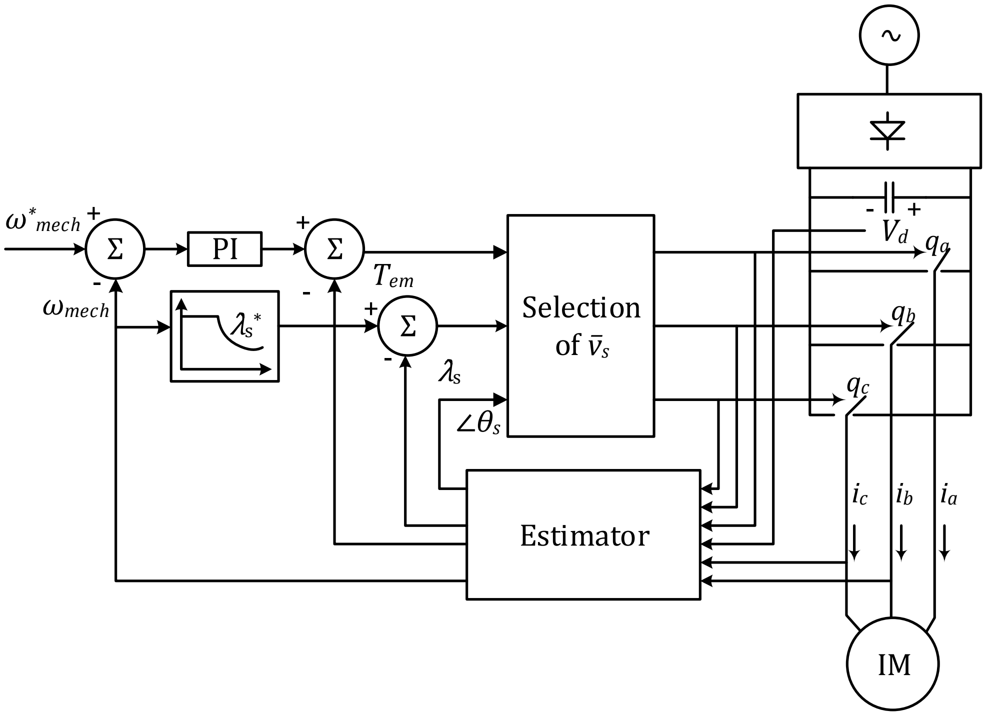

Figure 2.8 Block diagram of DTC [46]

The diagram includes the speed and the torque feedback loops, without a speed encoder The estimated speed $\omega_{mech,est}$ is subtracted from the reference speed ω^*_{mech} and the error between the two acts on a PI-controller to generate the torque reference signal T^*_{em}. The estimated speed generates the reference signal for the stator flux linkage $\hat{\lambda}_s^*$ (thus allowing flux weakening for extended range of speed operation), which is compared with the estimated stator flux linkage $\hat{\lambda}_{s,est}$. The errors in the electromagnetic torque and the stator flux, combined with the angular position $\angle\theta_s$ of the stator flux linkage space vector determine the stator voltage space vector $\vec{v}_s$ that is applied to the motor during each sampling interval ΔT.

Estimating the electromagnetic torque and the stator flux linkage vector requires measuring the stator currents and the stator phase voltages. The phase voltages, as shown in the figure above, are indirectly calculated by measuring the dc-bus voltage and knowing within the digital controller the status of the inverter switches.

2.2.2.1 Principle of Encoder-less DTC Operation

Below is enumerated the various steps in the estimator block of Figure 2.17 culled from Ref. [46] as follows, where all space vectors are implicitly expressed in electrical radians with respect to the stator a-axis as the reference axis:

1) From the measured stator voltages and currents, calculate the stator flux linkage space vector $\hat{\lambda}_s$:

$$\vec{\lambda}_s(t) = \vec{\lambda}_s(t-\Delta T) + \int_{t-\Delta T}^{t} (\vec{v}_s - R_a\vec{i}_s).d\tau = \vec{\lambda}_s e^{j\theta_s} \tag{2.17}$$

2) From $\vec{\lambda}_s$ and $\vec{i}_s$, calculate the rotor flux space vector $\vec{\lambda}_r$ and hence the speed of the rotor flux linkage vector, where ΔT_ω is a sampling time for speed calculation:

$$\vec{\lambda}_r = \frac{L_r}{L_m}\left(\vec{\lambda}_s - \sigma L_s \vec{i}_s\right) = \vec{\lambda}_r e^{j\theta_r} \tag{2.18}$$

and

$$\omega_r = \frac{d}{dt}\theta_r = \frac{\theta_r(t) - \theta_r(t-\Delta T_\omega)}{\Delta T_\omega} \tag{2.19}$$

3) From $\vec{\lambda}_s$ and $\vec{i}_s$, calculate the estimated electromagnetic torque T_{em}:

$$T_{em} = \frac{p}{2} Im\left(\vec{\lambda}_s^{conj} \vec{i}_s\right) \tag{2.20}$$

4) From $\vec{\lambda}_r$ and $T_{em,est}$, estimate the slip speed ω_{slip} and the rotor speed ω_m:

$$\omega_{slip} = \frac{2}{p}\left(\frac{3}{2} R_r \frac{T_{em}}{\hat{\lambda}_r^2}\right) \tag{2.21}$$

and

$$\omega_m = \omega_r - \omega_{slip} \tag{2.22}$$

In the stator voltage selection block, an appropriate stator voltage vector is calculated to be applied for the next sampling time interval ΔT based on the errors in the torque and the stator flux, in order to keep them within a hysteretic band.

However, at low frequencies, large errors can occur due to the variation of the stator resistances, integrator drift and noise. A common technique in DTC is to control the torque and stator flux amplitude with a hysteretic band around their desired values, other techniques can be used (e.g. flux observers) [45, 46]. It is at this point that application of VSS control theory comes into play.

The main features of DTC are [45]: direct control of stator and electromagnetic torque; indirect control of stator current and voltages; approximately sinusoidal stator fluxes and stator currents; reduced torque oscillations; excellent torque dynamics; inverter switching frequency depending on flux and torque hysteresis bands.

The main advantages of DTC are: absence of co-ordinate transformations (which are required in most vector-controlled implementations); absence of separate voltage modulation bock (required in vector drives) absence of voltage decoupling circuits (required in VSI fed vector drives); reduced number of controllers etc. However, in general, the main disadvantages of a conventional DTC can be: possible problems during starting and low-speed operation and during changes in torque command; requirement for flux-linkage and electromagnetic torque estimators (same problem exists for vector drives); variable switching frequency (the inverter is in a bang-bang switching fashion and then has a variable switching frequency) [47].

2.2.3 Variable Structure Systems and Control

Variable structure systems (VSS) are discontinuous dynamic systems whose control structures are changed according to some chosen state variable so as to achieve certain control objectives [48, 49]. In simplest terms, the sliding mode (SM) control is a kind of nonlinear control which has been developed primarily for the control of variable structure systems. Technically, it consists of a time-varying state-feedback discontinuous control law that switches at a high frequency from one continuous structure to another according to the present position of the state variables in the state space, the objective being to force the dynamics of the system under control to follow exactly what is desired and pre-determined [50]. Variable structure systems which operate in sliding mode have the advantages of: *1*) robustness against a large class of perturbations or model uncertainties *2*) reduced amount of information in comparison to classical control techniques. SM control allows the possibility of stabilizing some nonlinear systems which are not stabilizable by continuous state feedback laws [51]. SMC systems are designed to drive the system states onto a particular surface in the state space, named sliding surface. Once the sliding surface is reached, sliding mode control keeps the states on the close neighbourhood of the sliding surface. Hence the sliding mode control is a two part controller design. The first part involves the design of a sliding surface so that the sliding motion satisfies design specifications. The second is concerned with the selection of a control law that will make the switching surface attractive to the system state [52]. The analysis and synthesis of the general dynamic VSS is discussed in the following subsections

2.2.3.1 Definition of the General VSS Control Problem

This explanation and analysis is based on the report in Ref [49]. Consider the general dynamic system given as:

$$\frac{dx}{dt} = F(x,t,u) \tag{2.23}$$

where the state vector $x = [x_1(t)\ x_2(t) \ldots x_n(t)]^T$, the continuously differentiable continuous function

$$F = [F_1(x,t)\ F_2(x,t) \ldots F_n(x,t)]^T,\ u(x,t) = [u_1(x,t)\ u_2(x,t) \ldots u_m(x,t)]^T.$$

The general VSS control synthesis problem can then be stated as follows:

1) Find a switching surface $\sigma(x) = [\sigma_1, \sigma_2, \dots, \sigma_m]^T = 0$ which is of lower order than that of the given plant and represents the desired system dynamics.
2) Design a variable structure control $u(x,t)$ such that starting at $t = 0$, the state vector is driven to reach the surface $\sigma(x) = 0$ at $t = t_0$, and afterwards never leave it.

The variable structure control is in the form,

$$\begin{aligned} u_1(x,t) &= u^+(x,t) \qquad when\ \sigma_1(x) > 0, i = 1, 2, \dots, m \\ u_1(x,t) &= u^-(x,t) \qquad when\ \sigma_1(x) < 0, i = 1, 2, \dots, m \end{aligned} \tag{2.24}$$

where $u_1(x,t)$ are components of the control vector $u(x,t)$ each of which is switched across their respective surface $\sigma_1(x,t)$, such that away from the surface, the i^{th} control is either $u_1^+(x,t)$ or $u_1^-(x,t)$, both of which are continuous functions.

The switching surfaces $\sigma_1(x) = 0, \sigma_2(x) = 0, \dots, \sigma_m(x) = 0$ are components of the $(n\text{-}m)$ dimensional switching surface $\sigma(x) = 0$. The switching surfaces are designed such that if the state vector is restricted to $\sigma(x) = 0$, the resulting dynamics will satisfy desired control objectives such as tracking, stability, regulation, etc. When the control $u(x,t)$ is able to restrict the state vector dynamics to that of the switching surface, the system is said to be in the sliding mode. The switching surface can then be referred to as sliding surfaces.

The analysis of VSS involving the examination of the criteria for the *existence*, *reachability* and *stability* of the sliding mode, is investigated in the next subsections.

2.2.3.2 Existence and Stability Conditions of the Sliding Mode

Existence conditions in the sliding mode requires the convergence of the state trajectories to the surface $\sigma(x) = 0$. This implies that existence and stability conditions of the sliding mode are closely related.

Three methods are outlined below for establishing the existence of the sliding mode [49].

A. The Direct Switching Function Method:

A sufficient condition for the existence of the sliding mode can be ascertained by determining the behaviour of the state trajectories on the switching surface $\sigma(x) = 0$. The objective here is to verify the possibility of the state vector coming back to the intersection, if deviations occur in the neighbourhood of the intersection of the switching surfaces (i.e. $\sigma(x) = 0$):

$$\begin{matrix} d\sigma(x)/dt > 0 & when\ \sigma(x) < 0 \\ d\sigma(x)/dt < 0 & when\ \sigma(x) > 0 \end{matrix} \quad (2.25)$$

Condition (2.25) can alternatively be stated as,

$$\sigma(x)\,d\sigma(x)/dt < 0 \quad (2.26)$$

This existence condition is global. A similar sufficient condition, local in nature is [53]:

$$\lim_{\sigma(x)\to 0^+} \sigma(x)/dt < 0 \quad (2.27)$$

B. The Ljapunov Function Method

If a continuously differentiable Ljapunov function $V(x, \sigma, t)$ exists that satisfy the following conditions, then the sliding mode exists hence is stable:

1) $V(x, \sigma, t)$ is positive definite with respect to σ, for example

$$V(x, \sigma, t) = 0.5\sigma^T\sigma \quad (2.28)$$

2) The time derivative of the function,

$$dV(x, \sigma, t)/dt < 0 \qquad when\ \sigma(x) \neq 0 \quad (2.29)$$

1) and 2) are global sliding mode reaching conditions. The choice of a suitable Ljapunov function might be difficult, especially for non-linear systems [49].

C. The Reaching Law Method:

The reaching law is a differential equation which specifies the dynamics of the switching surface, thus, establishes the sliding mode condition as well as the dynamics during the reaching mode.

The general switching law proposed in Ref [54] is as follows:

$$d\sigma/dt = -Rsign(\sigma) - PF(\sigma) \tag{2.30}$$

where:

$sign(\sigma) = [sign(\sigma_1), sign(\sigma_2), \dots, sign(\sigma_m)]^T$,

$R = diag[r_1, r_2, \dots, r_m], r_i > 0$,

$P = diag[p_1, p_2, \dots, p_m], p_i > 0$,

$F(\sigma) = [f_1(\sigma_1), f_2(\sigma_2), \dots, f_m(\sigma_m)]^T$,

$\sigma_i f_i(\sigma_i) > 0,\ when\ \sigma_i \neq 0,\ i = 1, 2, \dots, m$,

Choice of R and P will result in the desired reaching law. For example,

(a) for $P = 0$, Equation (2.30) results in a constant reaching law,

$$d\sigma/dt = -Rsign(\sigma) \tag{2.31}$$

(b) for $P = 0$ and $r_1 = -k_1|\sigma_1|^q, 0 < q < 1, i = 1, 2, \dots, m$, the reaching law becomes a power rate reaching law:

$$d\sigma_i/dt = -k_1|\sigma_1|^q sign(\sigma_i) \tag{2.32}$$

An illustration is presented to further explain the concepts that have been described.

2.2.3.3 Main Concepts of Sliding Mode Control

For illustration purposes, the single-dimensional motion of a unit mass (Figure 2.16) is considered.

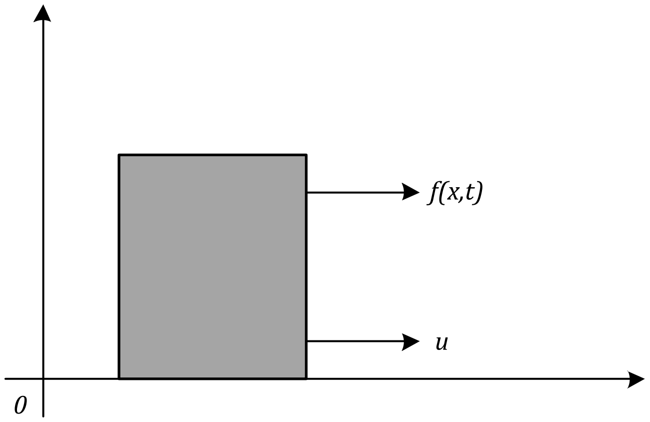

Figure 2.9 Single-dimensional motion of a unit mass

A state-variable description is easily obtained by introducing variables for the position and the velocity $x_1 = x$, $x_2 = \dot{x}_1$ so that

$$\begin{cases} \dot{x}_1 = x_2 & x_1(0) = x_{10} \\ \dot{x}_2 = u + f(x_1, x_2, t) & x_2(0) = x_{20}, \end{cases} \qquad (2.33)$$

where u is the control force, and the disturbance term $f(x_1, x_2, t)$, which may comprise dry and viscous friction as well as any other unknown resistance forces, is assumed to be bounded, i.e., $|f(x_1,x_2, t)| \leq L > 0$. The problem is to design a feedback control law $u = u(x_1,x_2)$ that drives the mass to the origin asymptotically. In other words, the control $u = u(x_1,x_2)$ is supposed to drive the state variables to zero: i.e. $\lim_{t\to\infty} x_1, x_2 = 0$. This control problem requires asymptotic convergence to be achieved in the presence of the unknown bounded disturbance $f(x_1,x_2, t)$. For instance, a linear state-feedback control law

$$u = -k_1x_1 - k_2x_2, \quad k_2 > 0 \qquad (2.34)$$

provides asymptotic stability of the origin only for $f(x_1,x_2, t) \equiv 0$ and typically only drives the states to a bounded domain $\Omega(k_1,k_2,L)$ for $|f(x_1,x_2, t)| \leq L > 0$.

The desired compensated dynamics for the system (Equation 2.33) can be introduced, such as the homogeneous linear time-invariant differential equation:

$$\dot{x}_1 + cx_1 = 0, \quad c > 0 \qquad (2.35)$$

Since $x_2(t) = \dot{x}_1(t)$, a general solution of Equation (2.35) and its derivative is given by

$$\begin{aligned} x_1(t) &= x_1(0)\, exp(-ct) \\ x_2(t) &= \dot{x}_1(t) = -cx_1(0)\, exp(-ct) \end{aligned} \qquad (2.36)$$

Both $x_1(t)$ and $x_2(t)$ converge to zero asymptotically (note, no effect of the disturbance $f(x_1, x_2, t)$ on the state compensated dynamics is observed). To achieve these compensated dynamics, firstly a new variable is introduced in the state space system in Equation (2.33):

$$\sigma = \sigma(x_1, x_2) = x_2 + cx_1, \;\; c > 0 \qquad (2.37)$$

In order to achieve asymptotic convergence of the state variables x_1,x_2 to zero ($\lim_{t\to\infty} x_1, x_2 = 0$) with a given convergence rate as in Equation (2.36), in the presence of the bounded disturbance $f(x_1, x_2, t)$, the variable σ in Equation (2.37) has to be driven to zero in finite time by means of the control u. This can be achieved by applying the Ljapunov function techniques to the σ – dynamics that are derived using Equations (2.33) and (2.37):

$$\dot{\sigma} = cx_2 + f(x_1, x_2, t) + u, \quad \sigma(0) = \sigma_0 \tag{2.38}$$

For the σ – dynamics (2.38), a candidate Ljapunov function is introduced taking the form

$$V = \frac{1}{2}\sigma^2 \tag{2.39}$$

In order to provide the asymptotic stability of Equation (2.38) about the equilibrium point $\sigma = 0$, the following conditions must be satisfied:

(a) $\dot{V} < 0 \; for \; \sigma \neq 0$

(b) $\lim_{\lceil\sigma\rceil \to \infty} V = \infty$

Condition (b) is obviously satisfied by V in Equation (2.39). In order to achieve finite-time convergence (global finite-time stability), condition (a) can be modified to be

$$\dot{V} \leq -\alpha V^{1/2}, \quad \alpha > 0 \tag{2.40}$$

Separating variables and integrating inequality (2.40) over the time interval $0 \leq \tau \leq t$, we obtain

$$V^{1/2}(t) \leq -\frac{1}{2}\alpha t + V^{1/2}(0) \tag{2.41}$$

Consequently, $V(t)$ reaches zero in a finite time t_r that is bounded by

$$t_r \leq \frac{2V^{1/2}(0)}{\alpha}. \tag{2.42}$$

Therefore, a control u that is computed to satisfy Equation (2.40) will drive the variable σ to zero infinite time and will keep it at zero thereafter.

The derivative of V is computed as

$$\dot{V} = \sigma\dot{\sigma} = \sigma(cx_2 + f(x_1, x_2, t) + u) \tag{2.43}$$

Assuming $u = -cx_2 + v$ and substituting it into Equation (2.43) we obtain

$$\dot{V} = \sigma(f(x_1, x_2, t) + v) = \sigma f(x_1, x_2, t) + \sigma v \leq |\sigma|L + \sigma v \tag{2.44}$$

Selecting $v = -\rho\text{sign}(\sigma)$ where

$$sign(x) = \begin{cases} 1 & if\ x > 0 \\ -1 & if\ x < 0 \end{cases} \tag{2.45}$$

and

$$sign(0) \in [-1 \quad 1] \tag{2.46}$$

with $\rho > 0$ and substituting it into Equation (2.44) results in

$$\dot{V} \leq |\sigma|L - |\sigma|\rho = -|\sigma|(\rho - L) \tag{2.47}$$

Taking into account Equation (2.39), condition (2.40) can be rewritten as

$$\dot{V} \leq -\alpha V^{1/2} = -\frac{\alpha}{\sqrt{2}}|\sigma|, \qquad \alpha > 0 \tag{2.48}$$

Combining Equations (2.47) and (2.48), the result obtained is

$$\dot{V} \leq -|\sigma|(\rho - L) = -\frac{\alpha}{\sqrt{2}}|\sigma| \tag{2.49}$$

Finally the control gain ρ is computed as

$$\rho = L + \frac{\alpha}{\sqrt{2}} \tag{2.50}$$

Consequently a control law u that drives σ to zero in finite time (Equation 2.42) is

$$u = -cx_2 - \rho sign(\sigma) \tag{2.51}$$

Obviously, $\dot{\sigma}$ must be a function of control u in order to successfully design the controller in Equation (2.40) or (2.51), this should be taken into account while designing the variable given in Equation (2.37). The first component of the control gain (Equation 2.50) is designed to compensate for the bounded disturbance $f(x_1, x_2, t)$ while the second term $\frac{\alpha}{\sqrt{2}}$ is responsible for determining the sliding surface reaching time given by Equation (2.42). The larger α, the shorter reaching time.

Some definitions will be made to interpret the variable (2.37), the desired compensated dynamic (2.35), and the control function (2.51) in a new paradigm.

Definition 1: The variable (2.37) is called a *sliding variable*

Definition 2: Equations (2.35) and (2.37) rewritten in a form

$$\sigma = x_2 + cx_1 = 0, \qquad c > 0 \tag{2.52}$$

corresponds to a straight line in the state space of the system (2.33) and are referred to as a *sliding surface*.

Condition (2.40) is equivalent to

$$\sigma\dot{\sigma} \leq -\frac{\alpha}{\sqrt{2}}|\sigma| \tag{2.53}$$

and is often termed the *reachability condition*. Meeting the *reachability* or existence condition (2.53) means the trajectory of the system in Equation (2.33) is driven towards the *sliding surface* (2.52) and remains on it thereafter.

Definition 3: the control $u = u(x_1, x_2)$ in Equation (2.51) that drives the state variable x_1, x_2 to the sliding surface (2.52) in finite time t_r, and keeps them on the surface afterwards in the presence of the bounded disturbance $f(x_1, x_2, t)$, is called a *sliding mode controller* and *an ideal sliding mode* is said to be taking place in the system (2.33) for all $t > t_r$.

Chapter 3

3 The Induction Motor: Mathematical Analysis

3.1 Induction Motor Analysis using Space Vectors

Usually referred to as the workhorse of industry, the induction machine has many applications. In this case, it is applied in traction for EV propulsion, and as the sole unit of propulsion, deep understanding of its principles of operation, its behaviour under different conditions and mathematical analysis of its operation is fundamental. In the following analysis, it is assumed that the magnetic material in the stator and the rotor: *1)* is operated in its linear region, and *2)* has an infinite permeability, i.e. there is no magnetic saturation.

3.1.1 Space Vectors

At any instant of time, each phase winding produces a sinusoidal flux-density distribution (mmf) in the air gap. This is one of the most fundamental principles of the IM, the creation of a rotating and sinusoidally distributed magnetic field in the air gap. Figure 3.1a shows an idealized three-phase, two-pole IM where each phase winding in the stator and rotor is represented by a concentrated coil. This three-phase windings (either in wye or delta form) are distributed sinusoidally in space and embedded in slots [16, 17]. Neglecting the effect of slots and space harmonics due to winding distribution, it can be shown that a sinusoidal three-phase balanced power supply in the three-phase stator windings creates a synchronously rotating magnetic field.

Consider that three-phase sinusoidal currents are impressed in the three-phase stator windings, which are given as

$$\begin{aligned} i_a &= I_m \cos \omega_e t \\ i_b &= I_m \cos\left(\omega_e t - \tfrac{2\pi}{3}\right) \\ i_c &= I_m \cos\left(\omega_e t + \tfrac{2\pi}{3}\right) \end{aligned} \qquad (3.1)$$

Each phase winding will independently produce a sinusoidally distributed mmf wave, which pulsates about the respective axes. Figure 3.1b shows the mmf waves at time $t = 0$ when $i_a = I_m$, $i_b = -I_m/2$, and $i_c = -I_m/2$.

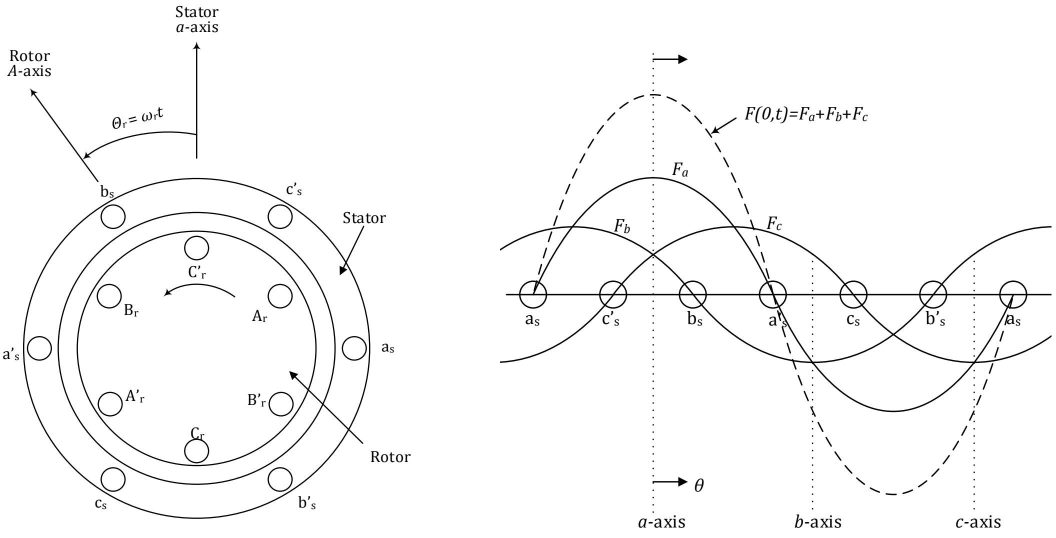

(a) Idealized three-phase 2-pole IM *(b) MMF distribution in three-phase winding of stator*

Figure 3.1 Principle of rotating magnetic field in IM

This sinusoidal mmf distribution can be represented by a space vector (of the appropriate length) along the magnetic axis of that phase (or opposite to if the phase current at that instant is negative). These mmf space vectors are $\vec{F}_a^a(t)$, $\vec{F}_b^a(t)$, and $\vec{F}_c^a(t)$, as shown in Figure 3.2a. The "→" represents an instantaneous quantity while the subscript "a" indicates that the space vectors are expressed as complex numbers with the stator a–axis chosen as the reference axis with an angle 0^0. Assuming no magnetic saturation, the resultant mmf distribution in the air gap due to all three phases at that instant can simply be represented using vector addition by the resultant space vector shown in Figure 3.2b where the subscript "s" represents the combined stator quantities:

$$\vec{F}_s^a(t) = \vec{F}_a^a(t) + \vec{F}_b^a(t) + \vec{F}_c^a(t) \tag{3.2}$$

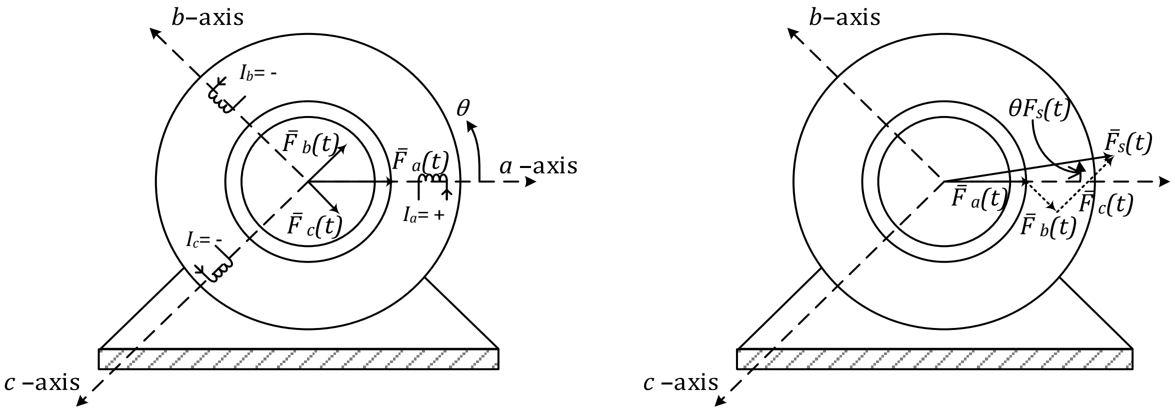

(a) mmf space vectors for the three phases $\vec{F}_a^a(t)$, $\vec{F}_b^a(t)$, and $\vec{F}_c^a(t)$ with reference to the a-axis at 0^0

(b) mmf space vectors showing the resultant space vector, $\vec{F}_s(t)$, dues to all three phases

Figure 3.2 Space vector representation of mmf

Field distributions (i.e. flux density, *B*, and magnetic field strength, *H*) are also distributed sinusoidally in the air gap at any instant of time, however, unlike the field quantities, the currents, voltages and the flux linkages of phase windings are treated as terminal quantities. The resultant current, voltage and flux linkage space vectors for the stator are calculated by multiplying instantaneous phase values by the stator winding orientation.

$$\vec{i}_s^a(t) = i_a(t)e^{j0} + i_b(t)e^{j2\pi/3} + i_c(t)e^{j4\pi/3} = \hat{I}_s(t)e^{j\theta_{i_s}(t)} \qquad (3.3)$$

$$\vec{v}_s^a(t) = v_a(t)e^{j0} + v_b(t)e^{j2\pi/3} + v_c(t)e^{j4\pi/3} = \hat{V}_s(t)e^{j\theta_{v_s}(t)} \qquad (3.4)$$

and,

$$\vec{\lambda}_s^a(t) = \lambda_a(t)e^{j0} + \lambda_b(t)e^{j2\pi/3} + \lambda_c(t)e^{j4\pi/3} = \hat{I}_s(t)e^{j\theta_{\lambda_s}(t)} \qquad (3.5)$$

The stator current space vector $\vec{i}_s^a(t)$ is very useful, noting that in Equation (3.2) $\vec{F}_s^a(t) = (N_s/p)\vec{i}_s^a(t)$:

> Explanation: At a time instant *t*, the three stator phase currents result in the same mmf (hence same flux-density distribution) acting on the air gap as that produced by $\vec{i}_s^a$, i.e. by a current equal to its peak value $\hat{I}_s$ flowing through a sinusoidally-distributed winding with magnetic axis orientation at $\theta_{i_s}(\theta_{F_s})$, this winding has the same number of turns *N_s* sinusoidally-distributed as any of the phase windings [46].

This simplifies the derivation of the electromagnetic torque which can be calculated on this winding, rather than having to calculate it separately on each of the phase windings and then summing it. Similar space vector equations can be written in the rotor circuit with the rotor axis-A as the reference.

Under a balanced sinusoidal steady state condition, the voltage and current phasors in phase-a have the same orientation as the stator voltage and current space vectors at time $t = 0$, the amplitudes are related by a factor of 3/2:

$$\vec{i}_s^{\,a}|_{t=0} = \frac{3}{2}\bar{I}_a \left(\hat{I}_s = \frac{3}{2}\hat{I}_a\right) \tag{3.6}$$

Equation (3.6) comes in handy in the dynamic analyses of the induction machine usually beginning with operation in a balanced, sinusoidal steady state.

3.1.2 Flux Linkages of the Stator and Rotor

Using the Kirchhoff's current law, the currents in the stator windings sum to zero. The flux-linkage equation for each phase is obtained by multiplying each equation with its winding orientation (phase shift):

$$\left[\lambda_{a,i_s}(t) = L_{ls}i_a(t) + L_m i_a(t)\right] \times e^{j0} \tag{3.7a}$$

$$\left[\lambda_{b,i_s}(t) = L_{ls}i_b(t) + L_m i_b(t)\right] \times e^{j2\pi/3} \tag{3.7b}$$

and,

$$\left[\lambda_{c,i_s}(t) = L_{ls}i_c(t) + L_m i_c(t)\right] \times e^{j4\pi/3} \tag{3.7c}$$

Note that in these equations, stator flux linkage due to the rotor currents is not included. Substituting Equations (3.7a) through (3.7c) into Equation (3.5), we obtain the stator flux linkage space vector to be:

$$\vec{\lambda}_{s,i_s}^{\,a}(t) = \underbrace{L_{ls}\vec{i}_s^{\,a}(t)}_{due\ to\ leakage\ flux} + \underbrace{L_m\vec{i}_s^{\,a}(t)}_{due\ to\ magnetizing\ flux} = L_s\vec{i}_s^{\,a}(t) \tag{3.8}$$

where $L_s = L_{ls} + L_m$. As in the case of stator current and voltage space vectors, the projection of the stator flux-linkage space vector along a phase axis, multiplied by a factor of 2/3, equals the flux linkage of that phase.

As obtained for the stator, the expression for the rotor flux-linkage space vector is:

$$\vec{\lambda}^{a}_{r,i_r}(t) = L_{lr}\vec{i}^{A}_{r}(t) + L_m\vec{i}^{A}_{r}(t) = L_r\vec{i}^{A}_{r}(t) \tag{3.9}$$

where the superscript "*A*" indicates the reference to phase-*A* of the rotor, and $L_r = L_{lr} + L_m$. When the stator and rotor currents are present simultaneously, the flux linking any of the stator phases is due to the stator currents as well as the mutual magnetizing flux due to the rotor currents. The magnetizing flux densities of the stator and rotor currents add up as vectors when the currents are simultaneously present. For the stator circuit,

$$\vec{\lambda}^{a}_{s}(t) = L_s\vec{i}^{a}_{s}(t) + L_m\vec{i}^{a}_{r}(t) \tag{3.10}$$

and for the rotor circuit,

$$\vec{\lambda}^{A}_{r}(t) = L_m\vec{i}^{A}_{s}(t) + L_r\vec{i}^{a}_{r}(t) \tag{3.11}$$

3.1.3 Stator and Rotor Voltage Equations in terms of Space Vectors

The individual phase equations can be combined to obtain the space vector equation as follows:

$$\left[v_a(t) = R_s i_a(t) + \frac{d}{dt}\lambda_a(t)\right] \times e^{j0} \tag{3.12a}$$

$$\left[v_b(t) = R_s i_b(t) + \frac{d}{dt}\lambda_b(t)\right] \times e^{j2\pi/3} \tag{3.12b}$$

and,

$$\left[v_c(t) = R_s i_c(t) + \frac{d}{dt}\lambda_c(t)\right] \times e^{j4\pi/3} \tag{3.12c}$$

Applying the definition of space vectors, we can re-write the stator voltages as a resultant voltage vector with reference to the stator *a* – axis as

$$\vec{v}^{a}_{s}(t) = R_s\vec{i}^{a}_{s}(t) + \frac{d}{dt}\vec{\lambda}^{a}_{s}(t) \tag{3.13}$$

and for the rotor

$$\vec{v}_r^A(t) = R_r \vec{\imath}_r^A(t) + \frac{d}{dt}\vec{\lambda}_r^A(t) \tag{3.14}$$

where in a squirrel-cage rotor, all the equivalent phase voltages are individually zero and $\vec{v}_r^A(t) = 0$ [46].

Note that these voltage equations include the time-derivatives of flux linkages that depend on rotor position. For this reason, the voltage equations in phase quantities expressed in space vector form in Equations (3.13) and (3.14), which contain time-derivatives of flux-linkages are complicated to solve. By using *dq* transformation, it is possible to make these equations easier. Also, the power of *dq*-winding analysis lies in the fact that it allows the torque and the flux in the machine to be controlled independently under dynamic conditions.

3.2 Dynamic Analysis of Induction Motor

Four frames of reference are normally used for describing the dynamic behaviour of the motor. The phase frame in *abc* coordinates, the stator frame in *αβ* coordinates, the rotor frame in *xy* coordinates and the field-oriented frame in *dq* coordinates [55]. Equations will be developed to analyse the induction motor operation under dynamic conditions. Space vectors will make transformation easier from *a-b-c* phase winding quantities into equivalent *dq*-winding quantities useable for dynamic (non-steady state) analysis.

3.2.1 *dq*-Winding Representation

In Figure 3.3a at time t, phase currents $i_a(t)$, $i_b(t)$, and $i_c(t)$ are represented by a stator current space vector $\bar{\imath}_s(t)$. A collinear mmf space vector $\bar{F}_s(t)$ is related to $\bar{\imath}_s(t)$ by a factor of (N_s/p), where N_s equals the number of turns per phase and p equals the number of poles:

$$\vec{\imath}_s^a(t) = i_a(t) + i_b(t)e^{j2\pi/3} + i_c(t)e^{j4\pi/3} \tag{3.15}$$

and,

$$\vec{F}_s^a(t) = \frac{N_s}{p}\vec{\imath}_s^a(t) \tag{3.16}$$

However, for dynamic analysis and control of ac machines, two orthogonal windings are required such that the torque and flux within the machine can be controlled independently. These two orthogonal windings will produce the same resultant mmf distribution as the three phase winding, each sinusoidally-distributed with $\sqrt{3/2}\,N_s$ turns: one winding along the d-axis and the other along the q-axis. This is illustrated in Figure 3.3b. This dq-winding set may be at an arbitrary angle θ_{da} with respect to the phase-a axis, however, the currents i_{sd} and i_{sq} in these windings must have specific values which can be obtained by equating the mmf produced by the dq-windings to that produced by the three phase windings and represented by a single winding with N_s turns in Equation (3.16)

$$\frac{\sqrt{3/2}N_s}{p}\left(i_{sd} + ji_{sq}\right) = \frac{N_s}{p}\vec{i}_s^d \;\;\therefore\;\; \left(i_{sd} + ji_{sq}\right) = \sqrt{\frac{2}{3}}\vec{i}_s^d \qquad (3.17)$$

Implying that the dq-winding currents are $\sqrt{2/3}$ times the projections of $\vec{i}_s(t)$ vector along the d- and q-axis as shown in Figure 3.3c. The factor $\sqrt{2/3}$ ensure that the dq winding currents produce the same mmf distribution as the three-phase winding currents. In Figure 3.3b, the d and the q windings are mutually decoupled magnetically due to their orthogonality. Choosing $\sqrt{3/2}\,N_s$ turns for each of these windings results in their magnetizing inductance to be L_m. Each of these equivalent windings has a resistance R_s and leakage inductance L_{ls} similar to the a-b-c phase windings, i.e. if a 3-phase machine were to be converted to a 2-phase machine using the same stator shell to deliver the same output power and speed, the number of turns for each of the 2-phase windings will be $\sqrt{3/2}\,N_s$.

Same analogy is applicable in the rotor, the mmf $\vec{F}_r(t)$ and the rotor current $\vec{i}_r(t)$ can also be produced by the components $i_{rd}(t)$ and $i_{rq}(t)$ flowing through their respective windings. Similar to the stator, each of the dq windings on the rotor has $\sqrt{3/2}\,N_s$ turns and a magnetizing inductance of L_m, and same magnetic path for flux lines. Each of the rotor equivalent windings have resistance R_r and leakage inductance L_{lr}. The mutual inductance between these two orthogonal windings is zero.

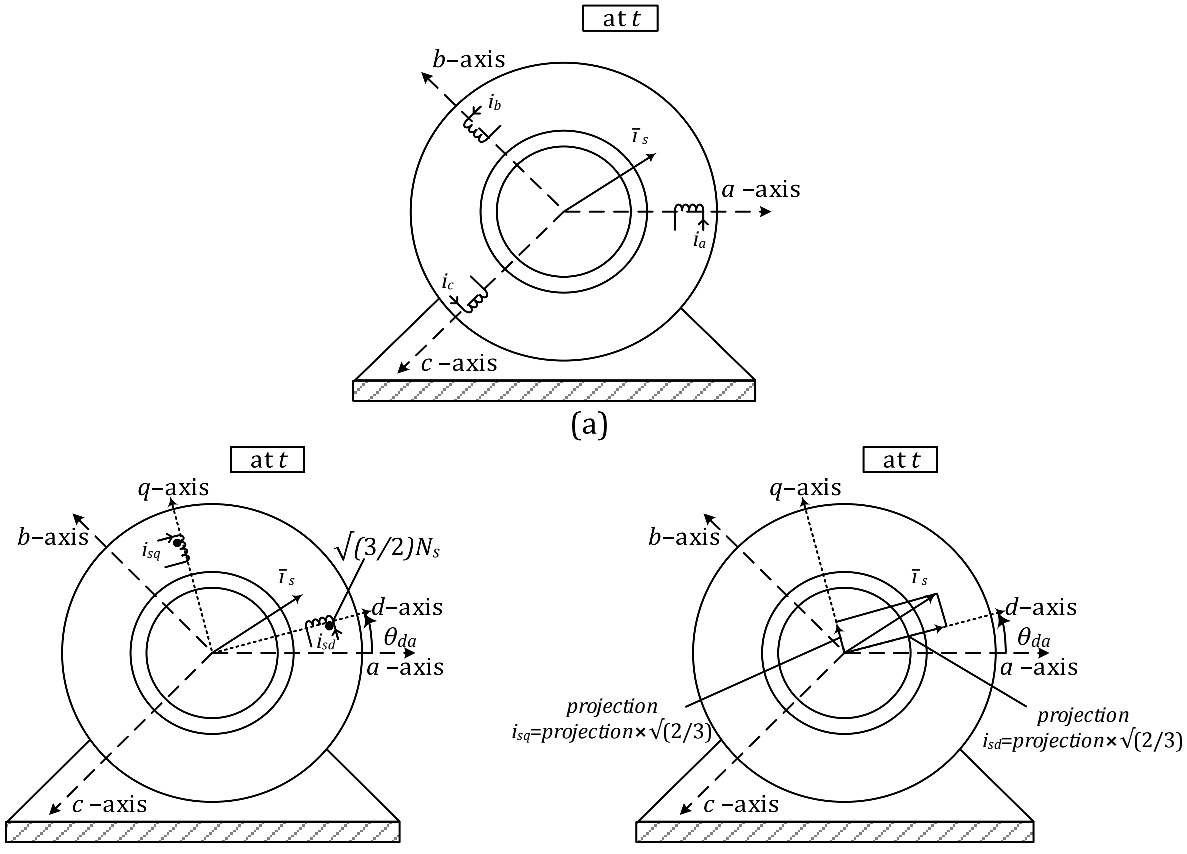

(b) (c)

Figure 3.3 Representation of stator mmf by equivalent dq windings

The equivalent *dq* windings for the stator and the rotor are shown in Figure 3.4. The mutual inductance between the stator and the rotor *d*-axis windings is equal to L_m due to the magnetizing flux crossing the air gap. Similarly, the mutual inductance between the stator and rotor *q*-axis windings equals L_m. The mutual inductance between and *d*-axis winding and any *q*-axis winding is zero because of their orthogonal orientation resulting in zero mutual magnetic coupling of flux.

3.2.2 Mathematical Relationships of the dq Windings (at an arbitrary speed ω_d)

Relationship between the stator and the rotor quantities and their equivalent *dq* winding components in Figure 3.4, which in combination produce the same mmf as the actual three phase windings will be described. Hereafter, the *d*-axis will be used as reference to any space vector.

From Figure 3.4, at time t, the d-axis is shown at an angle θ_{da} with respect to the stator a-axis. Therefore

$$\vec{i}_s(t) = \vec{i}_s^{\,a}(t)e^{-j\theta_{da}(t)} \tag{3.18}$$

Substituting for $\vec{i}_s^{\,a}$ from Equation (3.15),

$$\vec{i}_s(t) = i_a e^{-j\theta_{da}} + i_b e^{-j(\theta_{da}-2\pi/3)} + i_c e^{-j(\theta_{da}-4\pi/3)} \tag{3.19}$$

Equating the real and imaginary components on the right side of Equation (3.19) to i_{sd} and i_{sq} in Equation (3.15)

$$\begin{bmatrix} i_{sd}(t) \\ i_{sq}(t) \end{bmatrix} = \underbrace{\sqrt{\frac{2}{3}}\begin{bmatrix} cos(\theta_{da}) & cos\left(\theta_{da}-\frac{2\pi}{3}\right) & cos\left(\theta_{da}-\frac{4\pi}{3}\right) \\ -sin(\theta_{da}) & -sin\left(\theta_{da}-\frac{2\pi}{3}\right) & -sin\left(\theta_{da}-\frac{4\pi}{3}\right) \end{bmatrix}}_{[T_s]_{abc\to dq}} \begin{bmatrix} i_a(t) \\ i_b(t) \\ i_c(t) \end{bmatrix} \tag{3.20}$$

where $[T_s]_{abc\to dq}$ is the transformation matrix to transform stator a-b-c phase winding currents to the corresponding dq-winding currents. The same transformation matrix relates the stator flux linkages and the stator voltages in phase windings to those in the equivalent stator dq windings.

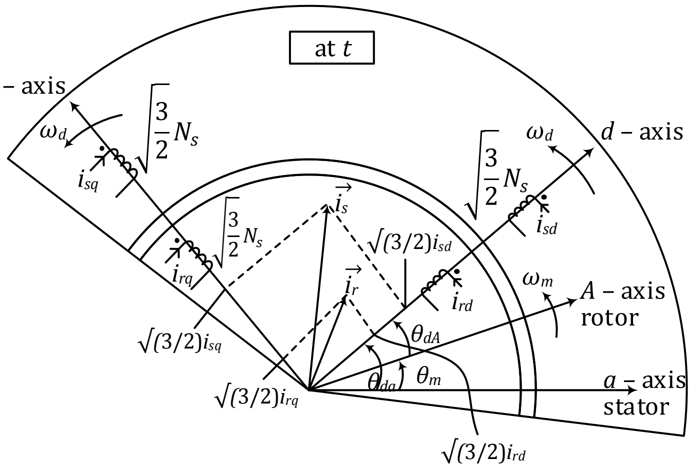

Figure 3.4 Stator and rotor representation by equivalent dq winding currents. The dq winding voltages are defined as positive at the dotted terminals. Note that the relative positions of the stator and the rotor current space vectors are not actual, rather only for definition purposes.

A similar procedure to that in the stator case is followed for the rotor where in terms of the phase currents, the current space vector is

$$\vec{i}_r^A(t) = i_A(t) + i_B(t)e^{j2\pi/3} + i_C(t)e^{j4\pi/3} \tag{3.21}$$

From Figure 3.4, at time t, d-axis is at an angle θ_{dA} with respect to the rotor A-axis. Therefore,

$$\vec{i}_r(t) = \vec{i}_r^A(t)e^{-j\theta_{dA}(t)} \tag{3.22}$$

The currents in the dq rotor windings must be i_{rd} and i_{rq} where these two current components are also $\sqrt{2/3}$ times the projections of $\vec{i}_r(t)$ vector along the d- and q-axis as shown in Figure 3.4.

Similar to Equation (3.20), replacing θ_{da} by θ_{dA}

$$\begin{bmatrix} i_{rd}(t) \\ i_{rq}(t) \end{bmatrix} = \underbrace{\sqrt{\frac{2}{3}} \begin{bmatrix} cos(\theta_{dA}) & cos\left(\theta_{dA} - \frac{2\pi}{3}\right) & cos\left(\theta_{dA} - \frac{4\pi}{3}\right) \\ -sin(\theta_{dA}) & -sin\left(\theta_{dA} - \frac{2\pi}{3}\right) & -sin\left(\theta_{dA} - \frac{4\pi}{3}\right) \end{bmatrix}}_{[T_r]_{ABC\to dq}} \begin{bmatrix} i_A(t) \\ i_B(t) \\ i_C(t) \end{bmatrix} \tag{3.23}$$

where $[T_r]_{ABC\to dq}$is the transformation matrix for the rotor. The same transformation matrix relates the stator flux linkages and the stator voltages in phase windings to those in the equivalent stator dq windings.

In case of an isolated neutral where all three phase currents add up to zero at any time, the variables a-b-c phase windings can be calculated in terms of the dq winding variables. A row can be added at the bottom of Equation (3.20) to represent the condition that all three phase currents sum up to zero. Inverting the resulting matrix and discarding the last column whose contribution is zero, we obtained the desired relationship

$$\begin{bmatrix} i_a(t) \\ i_b(t) \\ i_c(t) \end{bmatrix} = \underbrace{\sqrt{\frac{2}{3}} \begin{bmatrix} cos(\theta_{da}) & -sin(\theta_{da}) \\ cos\left(\theta_{da} + \frac{4\pi}{3}\right) & -sin\left(\theta_{da} + \frac{4\pi}{3}\right) \\ cos\left(\theta_{da} + \frac{2\pi}{3}\right) & -sin\left(\theta_{da} + \frac{2\pi}{3}\right) \end{bmatrix}}_{[T_s]_{dq\to abc}} \begin{bmatrix} i_{sd} \\ i_{sq} \end{bmatrix} \tag{3.24}$$

where $[T_s]_{dq\to abc}$ is the transformation matrix in the reverse direction (dq to abc). A similar transformation matrix $[T_r]_{dq\to ABC}$ for the rotor can be written by replacing θ_{da} in Equation (3.24).

Recalling Figure 3.4, there is a set of four *dq* windings. There is no mutual coupling between the windings on the *d*-axis and those on the *q*-axis. The flux linking any winding is due to its own current and that due to the other winding on the same axis. Take the *d*-winding as an example. Due to i_{sd}, both the magnetizing flux as well as the leakage flux link this winding, however, due to i_{rd}, only the magnetizing flux links this stator winding (leakage flux does not cross the air gap). Using this logic, the following expression can be written for all four windings:

For the stator windings:

$$\lambda_{sd} = L_s i_{sd} + L_m i_{rd} \tag{3.25}$$

and

$$\lambda_{sq} = L_s i_{sq} + L_m i_{rq} \tag{3.26}$$

where in Equations (3.25) and (3.26), $L_s = L_{ls} + L_m$.

Similar equations are obtainable for the rotor windings:

$$\lambda_{rd} = L_r i_{rd} + L_m i_{sd} \tag{3.27}$$

and

$$\lambda_{rq} = L_r i_{rq} + L_m i_{sq} \tag{3.28}$$

where in Equations (3.27) and (3.28), $L_r = L_{lr} + L_m$.

3.2.2.1 *dq*-Winding Voltage Equations

To derive the *dq* winding voltages,

$$\vec{v}_{s\_dq} \cdot e^{j\theta_{da}} = R_s \vec{i}_{s\_dq} \cdot e^{j\theta_{da}} + \frac{d}{dt}\left(\vec{\lambda}_{s\_dq} \cdot e^{j\theta_{da}}\right) \tag{3.29}$$

By method of differentiating a product of functions,

$$\vec{v}_{s\_dq} \cdot \cancel{e^{j\theta_{da}}} = R_s \vec{i}_{s\_dq} \cdot \cancel{e^{j\theta_{da}}} + \frac{d\vec{\lambda}_{s\_dq}}{dt} \cdot \cancel{e^{j\theta_{da}}} + j \underbrace{\frac{d\theta_{da}}{dt}}_{\omega_d} \cdot \vec{\lambda}_{s\_dq} \cdot \cancel{e^{j\theta_{da}}} \text{ then,}$$

$$\vec{v}_{s\_dq} = R_s \vec{i}_{s\_dq} + \frac{d}{dt}\vec{\lambda}_{s\_dq} + j\omega_d \vec{\lambda}_{s\_dq} \tag{3.30}$$

where $\frac{d}{dt}\theta_{da} = \omega_d$ is the instantenous speed (in electrical radians per second) of the *dq* winding set in the air gap as shown in Figure 3.4. Separating the real and imaginary components in Equation (3.30),

$$v_{sd} = R_s i_{sd} + \frac{d}{dt}\lambda_{sd} - \omega_d \lambda_{sq} \tag{3.31}$$

and,

$$v_{sq} = R_s i_{sq} + \frac{d}{dt}\lambda_{sq} + \omega_d \lambda_{sd} \tag{3.32}$$

In Equations (3.31) and (3.32), the speed terms are the components that are proportional to ω_d (the speed of the dq reference frame relative to the actual physical stator winding speed) and to the flux-linkage of the orthogonal winding.

Equations (3.31) and (3.32) can be written in vector form as follows,

$$\begin{bmatrix} v_{sd} \\ v_{sq} \end{bmatrix} = R_s \begin{bmatrix} i_{sd} \\ i_{sq} \end{bmatrix} + \frac{d}{dt}\begin{bmatrix} \lambda_{sd} \\ \lambda_{sq} \end{bmatrix} + \omega_d \underbrace{\begin{bmatrix} 0 & -1 \\ 1 & 0 \end{bmatrix}}_{[M_{rotate}]} \begin{bmatrix} \lambda_{sd} \\ \lambda_{sq} \end{bmatrix} \tag{3.33}$$

The 2×2 matrix $[M_{rotate}]$ in Equation (3.33) in the vector form corresponds to the operator (j) in Equation (3.30), where $j(= e^{j\pi/2})$ has the role of rotating the space vector $\vec{\lambda}_{s\_dq}$ by an angle of $\pi/2$.

Similar to the stator analysis, $\alpha\beta$ windings are affixed to the rotor at an angle θ_{dA} with respect to A-axis. The same procedures are followed replacing θ_{da} by θ_{dA} to obtain the following results for the rotor winding voltages

$$v_{rd} = R_r i_{rd} + \frac{d}{dt}\lambda_{rd} - \omega_{dA} \lambda_{rq} \tag{3.34}$$

and,

$$v_{rq} = R_r i_{rq} + \frac{d}{dt}\lambda_{rq} + \omega_{dA} \lambda_{rd} \tag{3.35}$$

where $\frac{d}{dt}\theta_{dA} = \omega_{dA}$ is the instantaneous speed (in electrical radians per second) of the dq winding set in the air gap with respect to the rotor A-axis speed (rotor speed), i.e.

$$\omega_{dA} = \omega_d - \omega_m \tag{3.36}$$

In Equation (3.36), ω_m is the rotor speed in electrical radians per second. It is related to ω_{mech}, the rotor speed in actual radians per second, by the pole-pairs as follows:

$$\omega_m = (p/2)\omega_{mech} \tag{3.37}$$

In Equations (3.34) and (3.35), the speed terms are the components that are proportional to ω_{dA}, and to the flux-linkage of the orthogonal winding. Equations (3.34) and (3.35) can be written in vector form as:

$$\begin{bmatrix} v_{rd} \\ v_{rq} \end{bmatrix} = R_r \begin{bmatrix} i_{rd} \\ i_{rq} \end{bmatrix} + \frac{d}{dt}\begin{bmatrix} \lambda_{rd} \\ \lambda_{rq} \end{bmatrix} + \omega_{dA} \underbrace{\begin{bmatrix} 0 & -1 \\ 1 & 0 \end{bmatrix}}_{[M_{rotate}]} \begin{bmatrix} \lambda_{rd} \\ \lambda_{rq} \end{bmatrix} \tag{3.38}$$

Re-arranging, Equations (3.33) and (3.38) can be written in state space form (obtaining fluxes with voltages as inputs) as follows:

$$\frac{d}{dt}\begin{bmatrix} \lambda_{sd} \\ \lambda_{sq} \end{bmatrix} = \begin{bmatrix} v_{sd} \\ v_{sq} \end{bmatrix} - R_s \begin{bmatrix} i_{sd} \\ i_{sq} \end{bmatrix} - \omega_d \underbrace{\begin{bmatrix} 0 & -1 \\ 1 & 0 \end{bmatrix}}_{[M_{rotate}]} \begin{bmatrix} \lambda_{sd} \\ \lambda_{sq} \end{bmatrix} \tag{3.39}$$

and

$$\frac{d}{dt}\begin{bmatrix} \lambda_{rd} \\ \lambda_{rq} \end{bmatrix} = \begin{bmatrix} v_{rd} \\ v_{rq} \end{bmatrix} - R_r \begin{bmatrix} i_{rd} \\ i_{rq} \end{bmatrix} - \omega_{dA} \underbrace{\begin{bmatrix} 0 & -1 \\ 1 & 0 \end{bmatrix}}_{[M_{rotate}]} \begin{bmatrix} \lambda_{rd} \\ \lambda_{rq} \end{bmatrix} \tag{3.40}$$

Any arbitrary value for the *dq*-winding speed ω_d would suffice, however, there is one value (out of three) that usually is suitable: $\omega_d = \omega_{sync}$, 0 or ω_m, where ω_{sync} is the synchronous speed in electrical radians per second. The corresponding values for ω_{dA} equal ω_{slip}, $-\omega_m$ or 0, respectively where $\omega_{slip} = \omega_{syn} - \omega_m$ in electrical radians per second. Under a balanced sinusoidal steady state, the choice of $\omega_d = \omega_{syn}$ (hence $\omega_{dA} = \omega_{slip}$) results in the hypothetical *dq*-windings rotating at the same speed as the field distribution in the air gap. Therefore all the currents, voltages and flux linkages associated with the stator and the rotor *dq* windings are dc in a balanced sinusoidal steady state. It is easy to design *PI* controllers for dc quantities, hence ω_{syn} is often the choice for ω_d.

3.2.3 Electromagnetic Torque

On the rotor *d*-axis winding, the torque produced is due to the flux density produced by the *q*-axis windings, likewise on the rotor *q*-axis winding, the torque produced is due to the flux density produced by the *d*-axis windings.

Torque on the *d*-axis rotor winding can be shown to be [46],

$$T_{d,rotor} = \frac{P}{2} \underbrace{\left(L_m i_{sq} + L_r i_{rq}\right)}_{\lambda_{rq}} i_{rd} = \frac{P}{2} \lambda_{rq} i_{rd} \tag{3.41}$$

while torque expression on the q-axis rotor winding is:

$$T_{q,rotor} = \frac{P}{2} \underbrace{\left(L_m i_{sq} + L_r i_{rq}\right)}_{\lambda_{rd}} i_{rq} = \frac{P}{2} \lambda_{rd} i_{rq} \tag{3.42}$$

3.2.3.1 Net Electromagnetic Torque T_{em} on the Rotor

By superposition, adding the torques acting on the d-axis and the q-axis of the rotor windings, the instantaneous torque is:

$$T_{em} = T_{d,rotor} + T_{q,rotor} \tag{3.43}$$

which, using Equation (3.41) and (3.42) results in

$$T_{em} = \frac{P}{2} L_m \left(\lambda_{rq} i_{rd} - \lambda_{rd} i_{rq}\right) \tag{3.44}$$

Substituting for flux linkages in Equation (3.44), the electromagnetic torque can be expressed in terms of inductances as

$$T_{em} = \frac{P}{2} L_m \left(i_{sq} i_{rd} - i_{sd} i_{rq}\right) \tag{3.45}$$

3.2.3.2 Electrodynamics

The acceleration is determined by the difference of the electromagnetic torque and the load torque (including friction torque acting on J_{eq}, the combined inertia of the load and motor. In terms of actual (mechanical) speed of the rotor, ω_{mech} in rad/sec, where $\omega_{mech} = (2/P)\omega_m$,

$$\frac{d}{dt} \omega_{mech} = \frac{T_{em} - T_L}{J_{eq}} \tag{3.46}$$

3.2.4 d- and q-Axis Equivalent Circuits

Substituting for flux-linkage derivatives in terms of inductances into the voltage equations (Equations 3.31 and 3.32 for the stator and Equations 3.34 and 3.35 for the rotor),

$$v_{sd} = R_s i_{sd} - \omega_d \lambda_{sq} + L_{ls} \frac{d}{dt} i_{sd} + L_m \frac{d}{dt} (i_{sd} + i_{rd}) \tag{3.47}$$
$$v_{sq} = R_s i_{sq} + \omega_d \lambda_{sd} + L_{ls} \frac{d}{dt} i_{sq} + L_m \frac{d}{dt} \left(i_{sq} + i_{rq}\right) \tag{3.48}$$

and,

$$\underbrace{v_{rd}}_{=0} = R_r i_{rd} - \omega_{dA}\lambda_{rq} + L_{lr}\frac{d}{dt}i_{rd} + L_m\frac{d}{dt}(i_{sd} + i_{rd}) \tag{3.49}$$

$$\underbrace{v_{rq}}_{=0} = R_r i_{rq} + \omega_{dA}\lambda_{rd} + L_{lr}\frac{d}{dt}i_{rq} + L_m\frac{d}{dt}\left(i_{sq} + i_{rq}\right) \tag{3.50}$$

For each axis , the stator and rotor winding equations are combined to result in the *dq* equivalent circuits shown in Figure 3.5a and b. Using Equations 3.31 the terminals can be labelled across which the voltage is $d\lambda_{sd}/dt$ in Figure 3.5a. Similarly, using Equations 3.32, 3.34 and 3.35 respectively, the terminals can be labelled in Figure 3.5a and b with $d\lambda_{sq}/dt$, $d\lambda_{rd}/dt$ and $d\lambda_{rq}/dt$.

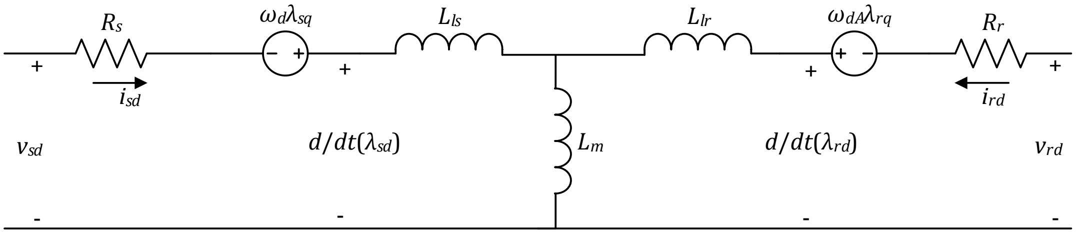

(a) d-axis

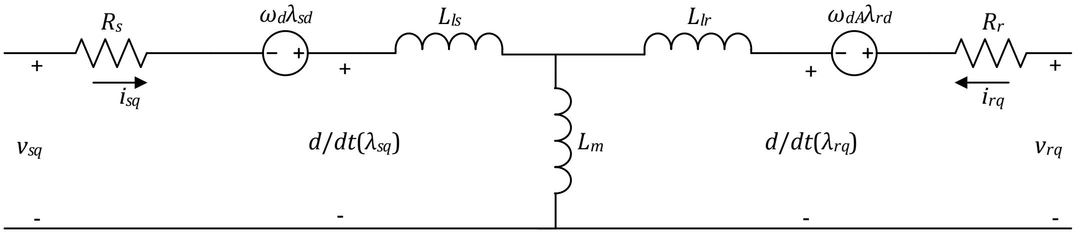

(b) q-axis

Figure 3.5 dq-winding equivalent circuits [46]

Under a balanced sinusoidal steady state condition, the *dq*-winding equations combine to result in the per-phase equivalent circuit of an induction machine. The reference $\omega_d = \omega_{syn}$ will be used so that the *dq*-winding quantities are dc and their time derivatives are zero under a balanced sinusoidal steady state condition. Therefore in the stator voltage equation, Equation (3.30), in steady state

$$\vec{v}_{s\_dq} = R_s\vec{i}_{s\_dq} + j\omega_{syn}\vec{\lambda}_{s\_dq} \qquad \textit{(steady state)} \tag{3.51}$$

Similarly, the voltage equation for the rotor *dq* windings under a balanced sinusoidal steady state with $\omega_d = \omega_{syn}$ (thus, $\omega_{dA} = \omega_{slip} = s\omega_{syn}$) results in

$$0 = \frac{R_r}{s}\vec{\imath}_{r\_dq} + j\omega_{syn}\vec{\lambda}_{r\_dq} \qquad \textit{(steady state)} \qquad (3.52)$$

where s is the slip. Substituting for flux linkage space vectors in Equations 3.51 and 3.52 results in

$$\vec{v}_{s\_dq} = R_s\vec{\imath}_{s\_dq} + j\omega_{syn}L_{ls}\vec{\imath}_{s\_dq} + j\omega_{syn}L_m\left(\vec{\imath}_{s\_dq} + \vec{\imath}_{r\_dq}\right) \qquad (3.53)$$

and,

$$0 = \frac{R_r}{s}\vec{\imath}_{r\_dq} + j\omega_{syn}L_{lr}\vec{\imath}_{r\_dq} + j\omega_{syn}L_m\left(\vec{\imath}_{s\_dq} + \vec{\imath}_{r\_dq}\right) \qquad (3.54)$$

The above space vector equations in a balanced sinusoidal steady state correspond to the following phasor equations for phase a:

$$\bar{V}_a = R_s\bar{I}_a + j\omega_{syn}L_{ls}\bar{I}_a + j\omega_{syn}L_m(\bar{I}_a + \bar{I}_A) \qquad (3.55)$$

and,

$$0 = \frac{R_r}{s}\bar{I}_A + j\omega_{syn}L_{lr}\bar{I}_A + j\omega_{syn}L_m(\bar{I}_a + \bar{I}_A) \qquad (3.56)$$

The above two equations combined correspond to the per-phase equivalent circuit of Figure 3.6.

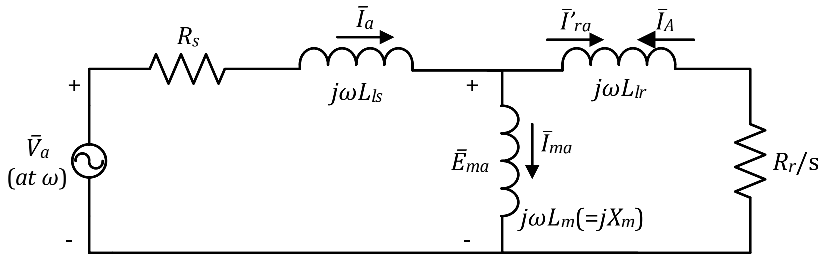

Figure 3.6 Per-phase equivalent circuit in steady state

3.3 Mathematical Analysis with respect to Sliding Mode Direct Torque Control

The analysis of the IM described in the previous section transformed the voltages from the *abc* coordinates to the *dq* coordinates, with similar process obtainable for current and flux. As earlier mentioned, DTC does not require *dq* transformation, and keeping the objectives of this thesis in perspective, the drive system illustrated in Figure 3.7 will be investigated. Research in the control of IMs is characterized by a great variety of control methodologies with different control/observation/adaptation algorithms combined with different coordinate systems, different state variables and different notations. For the sliding mode direct torque control design described in this section, the dynamic model given in the orthogonal stator coordinate frame (α,β coordinates) with stator current components and rotor flux components as state variables, complemented by the mechanical equation is discussed. At this point, the drive system is visualized and introduced so that inferences and references can be made without losing the objective of establishing the equations required for sliding mode direct torque control. From here on, equations will be developed to serve this purpose solely and not in general terms.

The structure of an IM drive system is presented in Figure 3.7. For sliding mode control design, it is convenient if the control inputs track values from the discrete set {$-u_0$, u_0} instead of On-Off signals from the discrete set {0, 1}.

Let the six On-Off signals be $S_w = [s_{w1}s_{w2}s_{w3}s_{w4}s_{w5}s_{w6}]^T$ with $s_{w4} = 1 - s_{w1}$, $s_{w5} = 1 - s_{w2}$, $s_{w6} = 1 - s_{w3}$ and the control inputs for sliding mode control design be $U_{gate} = [u_1 u_2 u_3]^T$ then the following relation holds [55]:

$$U_{gate} = u_0 L_w s_w \;\; with\; L_w = \begin{bmatrix} 1 & 0 & 0 & -1 & 0 & 0 \\ 0 & 1 & 0 & 0 & -1 & 0 \\ 0 & 0 & 1 & 0 & 0 & -1 \end{bmatrix} \qquad (3.57)$$

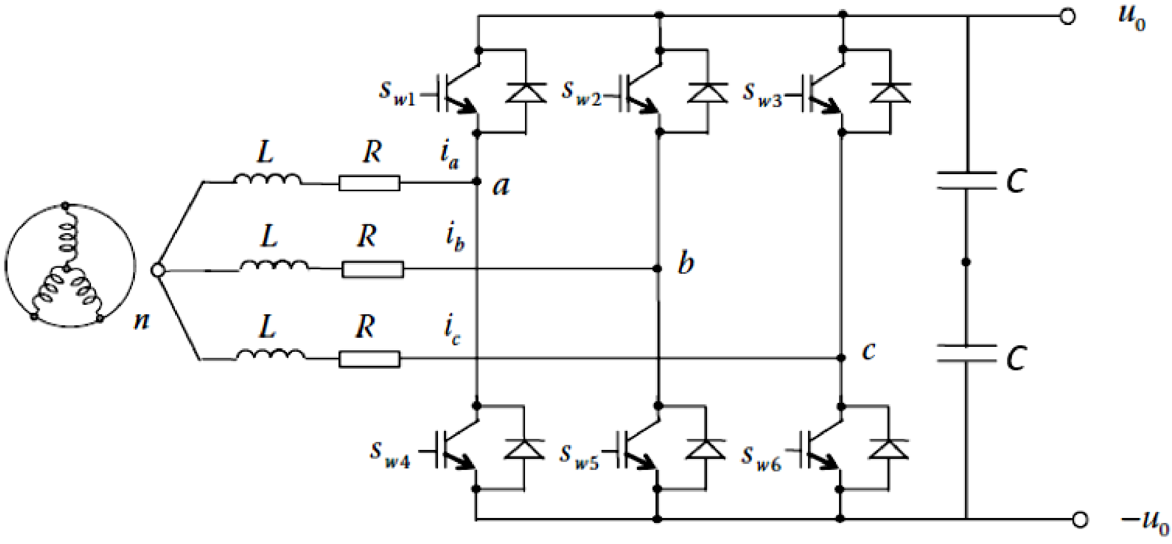

Figure 3.7 Structure of an IM drive system. n is the neutral point of the stator windings; v_a, v_b and v_c are the potential difference between points a, b, c and the neutral point n, respectively. i_a, i_b and i_c are the phase currents

The backward transformation can be obtained as

$$\begin{aligned} s_{w1} &= 0.5(1+u_1/u_0), \quad s_{w4} = 1 - s_{w1} \\ s_{w2} &= 0.5(1+u_2/u_0), \quad s_{w5} = 1 - s_{w2} \\ s_{w3} &= 0.5(1+u_3/u_0), \quad s_{w6} = 1 - s_{w3} \end{aligned} \tag{3.58}$$

The relationship between the phase voltages v_a, v_b, v_c and the discontinuous controls u_1, u_2, u_3 is given as

$$[v_a \quad v_b \quad v_c]^T = G[u_1 \quad u_2 \quad u_3]^T \tag{3.59}$$

Where G is defined as

$$G = \frac{1}{3}\begin{bmatrix} 2 & -1 & -1 \\ -1 & 2 & -1 \\ -1 & -1 & 2 \end{bmatrix} \tag{3.60}$$

Matrix G is a singular matrix implying that the phase voltages v_a, v_b, v_c are not linearly dependent. The motor model in $\alpha\beta$ coordinates is important for our control design and can be written as

$$\begin{aligned} \frac{di_\alpha}{dt} &= \beta\eta\lambda_\alpha + \beta\omega_e\lambda_\beta - \gamma i_\alpha + \frac{1}{\sigma L_s}v_\alpha, \\ \frac{di_\beta}{dt} &= \beta\eta\lambda_\beta - \beta\omega_e\lambda_\alpha - \gamma i_\beta + \frac{1}{\sigma L_s}v_\beta, \\ \frac{d\lambda_\alpha}{dt} &= -\eta\lambda_\alpha - \omega_e\lambda_\beta + \eta L_m i_\alpha, \\ \frac{d\lambda_\beta}{dt} &= -\eta\lambda_\beta + \omega_e\lambda_\alpha + \eta L_m i_\beta, \\ T &= \frac{3P}{2}\frac{L_m}{L_r}\left(i_\beta\lambda_\alpha - i_\alpha\lambda_\beta\right), \\ \frac{d\omega_r}{dt} &= \frac{1}{J}(T - T_l), \end{aligned} \tag{3.61}$$

with

$$\eta = \frac{R_r}{L_r}, \sigma = 1 - \frac{{L_m}^2}{L_s L_r}, \beta = \frac{L_m}{\sigma L_s L_r}, \gamma = \frac{1}{\sigma L_s}\left(R_s + \frac{{L_m}^2}{{L_r}^2} + R_r\right) \tag{3.62}$$

where the parameters are defined in Table 3.1

Stator currents i_α, i_β and stator voltages v_α, v_β are transformed from the phase currents i_a, i_b, i_c and phase voltages v_a, v_b, v_c by

$$\begin{aligned} [i_\alpha \quad i_\beta]^T &= A_{\alpha\beta}^{abc}[i_a \quad i_b \quad i_c]^T \\ [v_\alpha \quad v_\beta]^T &= A_{\alpha\beta}^{abc}[v_a \quad v_b \quad v_c]^T \end{aligned} \tag{3.63}$$

Table 3.1 Notations for the mathematical analysis of IM

v_α, v_β	Stator voltages in $\alpha\beta$ coordinates
i_α, i_β	Stator current in $\alpha\beta$ coordinates
λ_α, λ_β	Rotor flux components in $\alpha\beta$ coordinates
L_r, L_s, L_m	Rotor, stator and mutual inductance
R_r, R_s	Rotor and stator resistance
P	Number of pole pairs
ω_e	Electrical rotor speed
Σ	Leakage induction factor [56]
J	Mass of inertia
T	Motor torque
T_l	Load torque

where $A_{\alpha\beta}^{abc}$ denotes the transformation matrix

$$A_{\alpha\beta}^{abc} = \frac{2}{3}\begin{bmatrix} 1 & -\frac{1}{2} & -\frac{1}{2} \\ 0 & \frac{\sqrt{3}}{2} & -\frac{\sqrt{3}}{2} \end{bmatrix} \tag{3.64}$$

And the pseudo-inverse of matrix $A_{\alpha\beta}^{abc}$ denoted as ${A_{\alpha\beta}^{abc}}^{-1}$is

$${A_{\alpha\beta}^{abc}}^{-1} = \frac{3}{2}\left(A_{\alpha\beta}^{abc}\right)^T = \begin{bmatrix} 1 & -\frac{1}{2} & -\frac{1}{2} \\ 0 & \frac{\sqrt{3}}{2} & -\frac{\sqrt{3}}{2} \end{bmatrix}^T \tag{3.65}$$

The inverse transformation of stator currents/voltages to phase currents/voltages can be given as

$$\begin{aligned} [i_a \quad i_b \quad i_c]^T &= \left(A_{\alpha\beta}^{abc}\right)^{-1}[i_\alpha \quad i_\beta]^T \\ [v_a \quad v_b \quad v_c]^T &= \left(A_{\alpha\beta}^{abc}\right)^{-1}[v_\alpha \quad v_\beta]^T \end{aligned} \tag{3.66}$$

The motor model in dq coordinates which fixes on the rotor flux vector, can also be obtained by transforming the motor model from $\alpha\beta$ coordinates to dq using the rotor flux angle $\rho = arctg\left(\lambda_\beta/\lambda_\alpha\right)$:

$$\begin{aligned}
&\frac{di_d}{dt} = -\gamma i_d + \eta\beta\lambda_d + \omega_e i_q + \eta\frac{L_m {i_q}^2}{\lambda_d} + \frac{1}{\sigma L_s} v_d,\\
&\frac{di_q}{dt} = -\gamma i_q - \omega_e\beta\lambda_d - \omega_e i_d - \eta\frac{L_m i_d i_q}{\lambda_d} + \frac{1}{\sigma L_s} v_q,\\
&\frac{d\lambda_d}{dt} = -\eta\lambda_d + \eta L_m i_d,\\
&\frac{d\rho}{dt} = \omega_\rho = \omega_e + \omega_s,\ \ with\ \omega_s = \eta\frac{L_m i_q}{\lambda_d},\\
&T = \frac{3P}{2}\frac{L_m}{L_r}\lambda_d i_q,\\
&\frac{d\omega_r}{dt} = \frac{1}{J}(T - T_l),
\end{aligned} \tag{3.67}$$

where i_d and i_q are the stator currents in dq coordinates, v_d and v_q are the associated stator voltages, and λ_d is the d component of the rotor flux ($\lambda_q = 0$). Currents i_d, i_q and voltages v_d, v_q are transformed from $\alpha\beta$ coordinates by

$$\begin{aligned}
[i_d \quad i_q]^T &= [T]_{\alpha\beta\rightarrow dq}[i_\alpha \quad i_\beta]^T\\
[v_d \quad v_q]^T &= [T]_{\alpha\beta\rightarrow dq}[v_\alpha \quad v_\beta]^T
\end{aligned} \tag{3.68}$$

where transformation matrix $[\mathrm{T}]_{\alpha\beta\rightarrow dq}$ is defined as

$$[T]_{\alpha\beta\rightarrow dq} = \begin{bmatrix} \cos\rho & \sin\rho \\ -\sin\rho & \cos\rho \end{bmatrix} \tag{3.69}$$

This is an orthogonal matrix whose inverse is equal to its transpose, as a result, the backward transformation can be written as:

$$\begin{aligned}
[i_\alpha \quad i_\beta]^T &= \left([T]_{\alpha\beta\rightarrow dq}\right)^T[i_d \quad i_q]^T\\
[v_\alpha \quad v_\beta]^T &= \left([T]_{\alpha\beta\rightarrow dq}\right)^T[v_d \quad v_q]^T
\end{aligned} \tag{3.70}$$

The relationship between dq coordinates and abc coordinates can also be established. Phase currents $i_a \quad i_b \quad i_c$ and phase voltages $v_a \quad v_b \quad v_c$ can be transformed by

$$\begin{aligned}
&[i_d \quad i_q]^T = [\mathrm{T}]_{abc\rightarrow dq}[i_a \quad i_b \quad i_c]^T\\
&[v_d \quad v_q]^T = [T]_{abc\rightarrow dq}[v_a \quad v_b \quad v_c]^T
\end{aligned} \tag{3.71}$$

where transformation matrix $[\mathrm{T}]_{abc\rightarrow dq}$ depends on rotor flux angle ρ. Its pseudo-inverse $\left([\mathrm{T}]_{abc\rightarrow dq}\right)^{-1}$, required for backward transformation is given as

$$\left([T]_{abc\rightarrow dq}\right)^{-1} = \frac{3}{2}\left([T]_{abc\rightarrow dq}\right)^T \tag{3.72}$$

Leading to the backward transformation

$$[i_a \quad i_b \quad i_c]^T = \left([\mathrm{T}]_{abc\to dq}\right)^{-1}[i_d \quad i_q]^T$$

$$[v_a \quad v_b \quad v_c]^T = \left([T]_{abc\to dq}\right)^{-1}[v_d \quad v_q]^T \tag{3.73}$$

Relationship between the control voltages $v_d,\ v_q$ and discontinuous controls u_1, u_2, u_3 can be established as

$$[v_d \quad v_q]^T = [T]_{123\to dq}[u_1 \quad u_2 \quad u_3]^T \tag{3.74}$$

Note that $[\mathrm{T}]_{123\to dq} = [\mathrm{T}]_{abc\to dq}$, but to maintain clarity, $[\mathrm{T}]_{123\to dq}$ is used denoting transformation between discontinuous control u_1, u_2, u_3 and control voltages $v_d,\ v_q$. Its backward transformation is written as

$$[u_1 \quad u_2 \quad u_3]^T = \left([T]_{123\to dq}\right)^{-1}[v_d \quad v_q]^T \tag{3.75}$$

Thus far, the induction motor model in the (α, β) and in the (d, q) coordinate systems has been presented. Current and voltage transformations between the different coordinate systems were also given. They are very important for the control design of induction motors.

In DTC control of the IM, the rotor flux angle ρ is used instead of the electrical rotor angle θ_e. It is recognized that, for high control performance, angle ρ should be available, for sliding mode-based control design, this angle is required.

3.4 Classification of Induction Motor Control Methods

Induction motor control methods can be divided into scalar and vector control. The general classification of the frequency controllers is presented in Figure 3.8.

It is characteristic for scalar control that—based on a relation valid for steady states—only the magnitude and frequency (angular speed) of voltage, currents, and flux linkage of space vectors are controlled. Thus, the control system does not act on space vector position during transients. In contrast, in vector control—based on a relation valid for dynamic states—not just magnitude and frequency (angular speed), but also instantaneous positions of voltage, current, and flux space vectors are controlled [57].

In subsequent chapters, the scalar and vector based controls is discussed. The scope of this thesis is limited to *v/f* technique for scalar control and DTC in the vector regime. The *v/f* principles and method will be discussed for the voltage-fed inverter, this system will be modelled using MATLAB® and laboratory implementation of this scheme will be presented. Consequently, the DTC will be discussed with mathematical analysis and then modelled. The results of the *v/f* and DTC control schemes will be compared and discussed in the chapter on results.

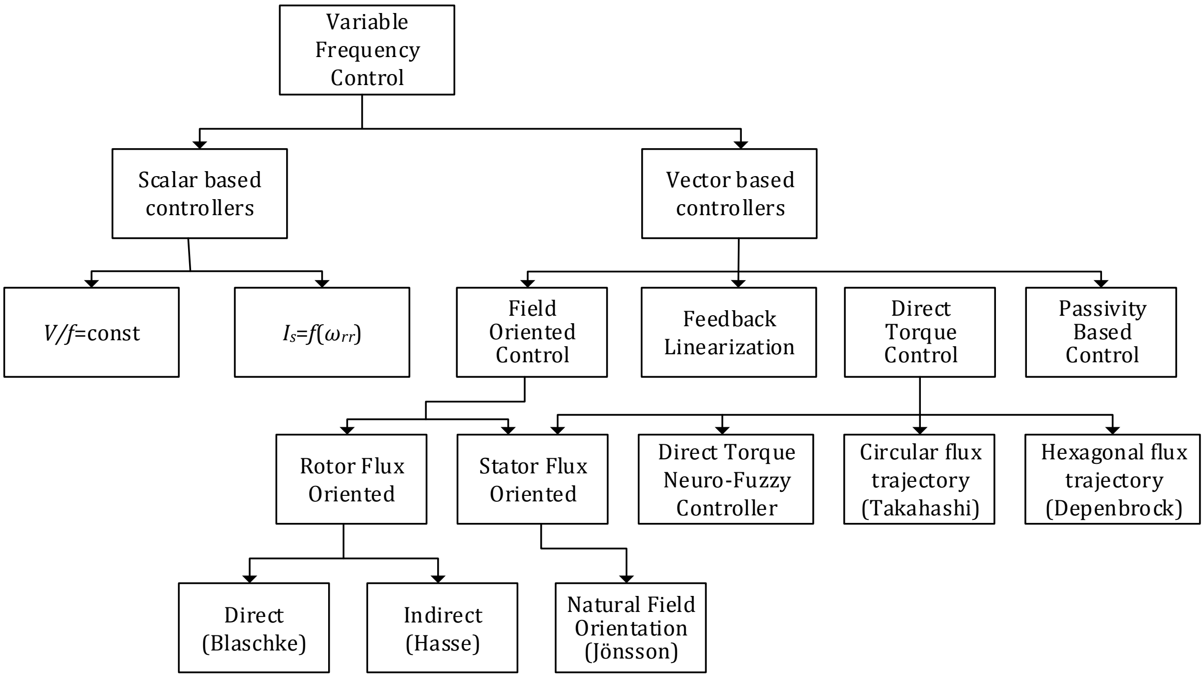

Figure 3.8 Classification of IM control Methods [57]

Chapter 4

4 Scalar Based Control Schemes

4.1 Scalar Control

Induction motors have different ways they can be controlled. The simplest methods are based on changing the structure of stator winding such as the *wye-delta* switching to change or reduce the starting current, pole changing, i.e. changing the number of magnetic poles on the stator etc. However in modern adjustable speed drives (ASDs), it is the stator voltage and current that are subject to control and in the steady state, are defined by the magnitude and frequency; and if these are the parameters that are adjusted, the control technique belongs in the class of scalar control [17]. Kazmierkowski [57] further explains that the control scheme is based on steady-state characteristics, which allows stabilization of the stator flux magnitude λ_s for different speed and torque values.

4.2 Control of Voltage-Fed Inverters for Induction Machines

There are different scalar control techniques of induction motor using voltage-fed inverter control, current-fed inverter control, constant flux operation with programmable current control and slip power recovery control [58]. For the purpose of this report, discussions will be limited to the voltage-fed inverter and the constant volts/hertz control method.

The power circuit of a voltage-fed inverter consists of a rectifier and inverter. In voltage-fed inverter control, one of the most widely recognized technique is the v/f control, where the voltage and frequency are maintained at a constant ration to achieve constant flux in the air gap, thus full torque up to zero speed. Before the v/f can be described in detail, it is expedient to understand the principle of inverter control.

4.2.1 Square-Wave or Six-Step Operation

The circuit in Figure 4.1 consists of three half-bridges, which are mutually phase-shifted by 2π/3 angle to generate the three-phase voltage wave. The input dc supply is usually obtained from a single-phase or three phase utility power supply through a diode-bridge rectifier and *LC* or *C* filter as shown [16]. Three binary switching variables *a*, *b*, and *c*, one per phase of the inverter are sufficient. Both switches in an inverter leg cannot be on simultaneously (shoot-through fault) because that would effectively short the dc supply source. The situation when both switches are off does not pose any problem but the voltage at the corresponding output terminal is undetermined [17].

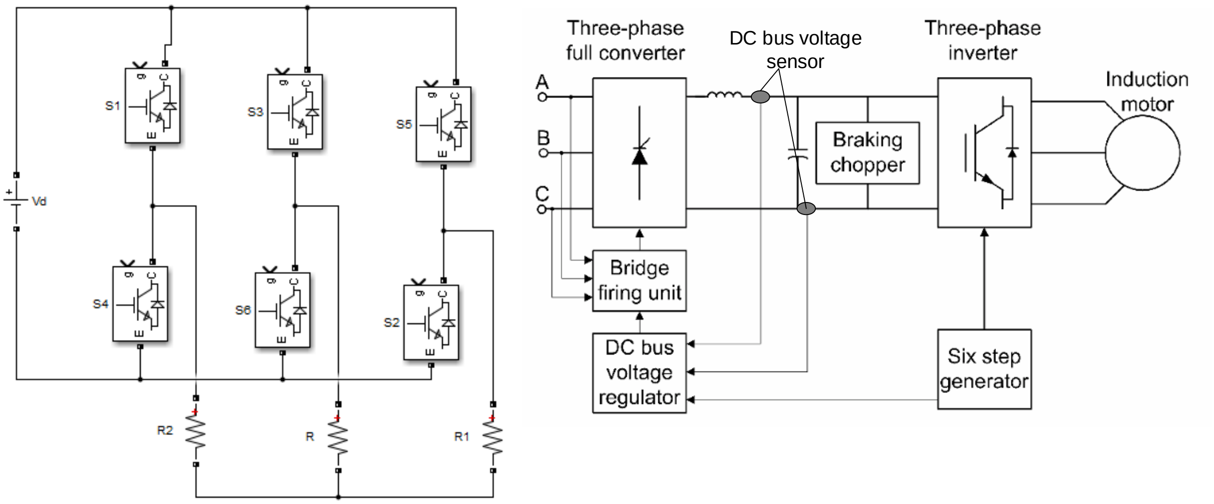

three-phase inverter

Square-wave v/f drive schematic

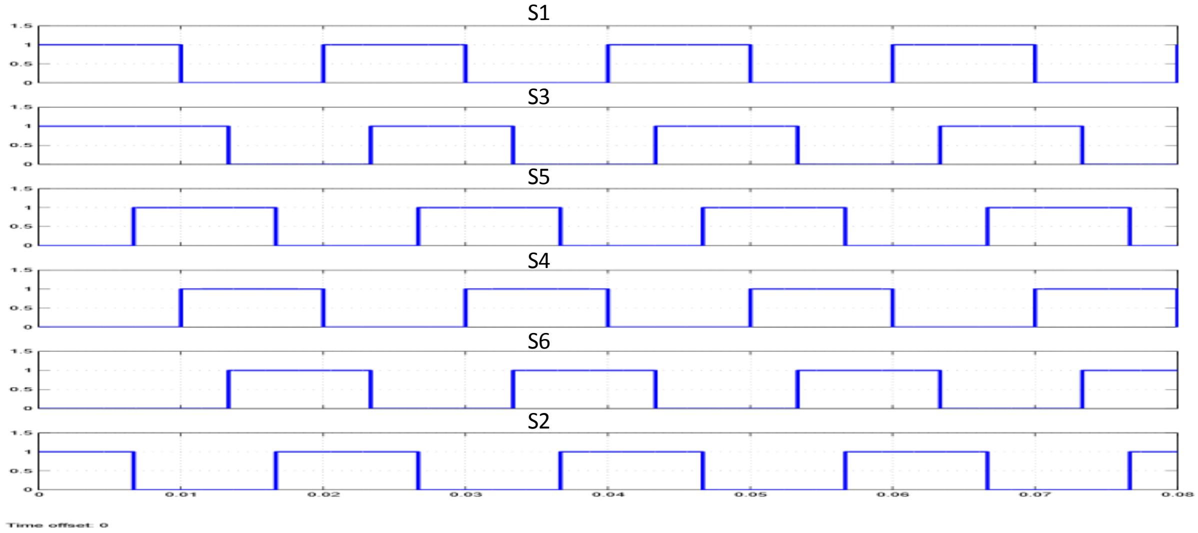

control signals (from six step generator)

Figure 4.1 Three-phase bridge inverter and complete square-wave drive system

In practice, a *dead-time* is designed to delay the signal (typically a few μs) to prevent a shoot-through fault [16]. Except for the very short delay (impressed by the dead-time), one switch in each phase is on, and the other is off. Consequently, each inverter leg can assume two states only, and the number of states of the whole inverter is eight (2^3).

The square-wave phase voltages with respect to the fictitious dc centre tap can be expressed by Fourier series as [16]

$$v_{ao} = \frac{2V_d}{\pi}\left[cos\,\omega t - \frac{1}{3} cos\,3\omega t + \frac{1}{5} cos\,5\omega t - \cdots\right] \tag{4.1}$$

$$v_{bo} = \frac{2V_d}{\pi}\left[cos\left(\omega t - \frac{2\pi}{3}\right) - \frac{1}{3} cos\,3\left(\omega t - \frac{2\pi}{3}\right) + \frac{1}{5} cos\,5\left(\omega t - \frac{2\pi}{3}\right) - \cdots\right] \tag{4.2}$$

$$v_{co} = \frac{2V_d}{\pi}\left[cos\left(\omega t + \frac{2\pi}{3}\right) - \frac{1}{3} cos\,3\left(\omega t + \frac{2\pi}{3}\right) + \frac{1}{5} cos\,5\left(\omega t + \frac{2\pi}{3}\right) - \cdots\right] \tag{4.3}$$

The line voltages v_{ab}, v_{bc}, and v_{ca}, can be constructed from Equations (4.1) – (4.3). When the three-phase load neutral *n* is connected, we have the following relations:

$$v_{ao} = v_{an} + v_{no} \tag{4.4}$$

$$v_{bo} = v_{bn} + v_{no} \tag{4.5}$$

$$v_{co} = v_{cn} + v_{no} \tag{4.6}$$

Since the load phase voltages are balanced, $v_{an} + v_{bn} + v_{cn} = 0$, adding these equations results in

$$\frac{1}{3}(v_{ao} + v_{bo} + v_{co}) = v_{no} \tag{4.7}$$

Therefore, substituting Equation (4.7) in (4.4) – (4.6) respectively,

$$v_{an} = \frac{2}{3}v_{ao} - \frac{1}{3}v_{bo} - \frac{1}{3}v_{co} \tag{4.8}$$

$$v_{bn} = \frac{2}{3}v_{bo} - \frac{1}{3}v_{ao} - \frac{1}{3}v_{co} \tag{4.9}$$

$$v_{cn} = \frac{2}{3}v_{co} - \frac{1}{3}v_{ao} - \frac{1}{3}v_{bo} \tag{4.10}$$

These isolated neutral-phase voltage can be described by Fourier series, or the waveforms constructed graphically as shown in Fig 4.2. This is the simplest control strategy for the inverter [17], the magnitude of voltage is $V/3$ across the parallel branches and $2V/3$ across the series branches. The phase voltages are six-stepped waveforms and line to line voltages are 120^0 quasi square waves shown in Figure 4.2. Phase and line voltages are displaced by 120^0 and the switches are triggered in the sequence 561-612-123-234-345-456 [2] effectively turning each switch on/off once per cycle only. Although the square-wave mode of operation has the advantage of outputting the maximum possible voltage, it possesses certain drawbacks such as poor load current quality due to high content of low-order voltage harmonics, also the magnitude of output voltage cannot be controlled within the inverter [17]. Laboratory design and implementation is discussed in later sections of this chapter and outputs presented in the experimental results section of chapter 6.

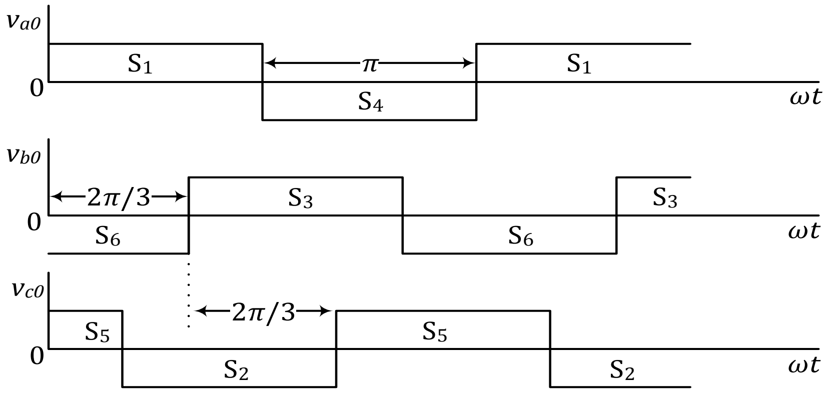

(a) switching logic signals to the power circuit

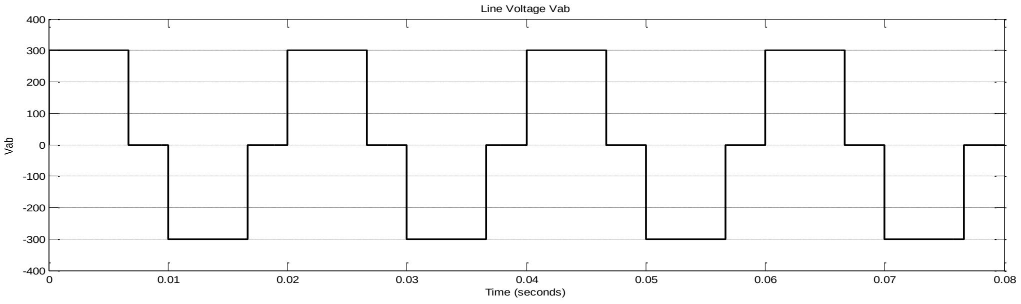

(b) line voltage output

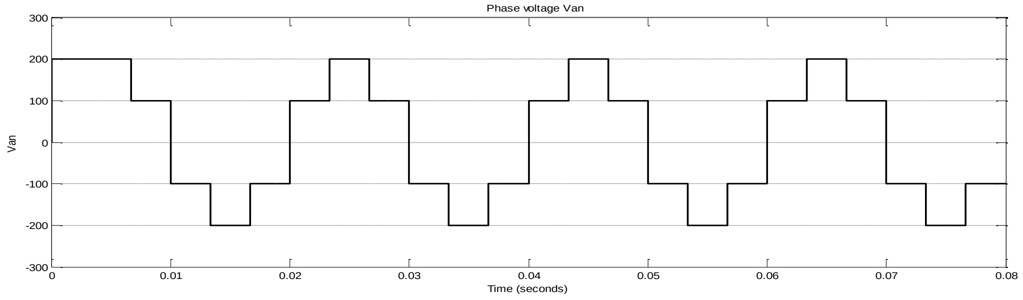

(c) phase voltage output

Figure 4.2 Output voltage waveforms in square wave mode

4.2.2 Pulse Width Modulation

The principle of the PWM is explained as follows: Because an inverter contains electronic switches, it is possible to control the output voltage as well as optimize the harmonics by performing multiple switching within the inverter with the constant dc input voltage v_d. The PWM principle to control the output voltage is explained in Figure 4.3. The fundamental voltage v_1 has the maximum amplitude ($4V_d/\pi$) at square wave, but by creating two notches as shown, the magnitude can be reduced. If the notch widths are increased, the fundamental voltage will be reduced.

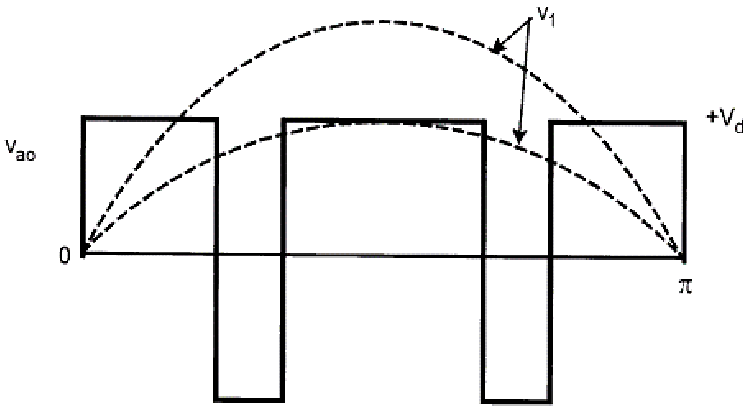

Figure 4.3 PWM principle to control output voltage [16]

Below are listed different possible PWM techniques:

a. Sinusoidal PWM (SPWM)
b. Random PWM
c. Selected harmonic elimination (SHE) PWM
d. Hysteresis band current control PWM
e. Minimum ripple current PWM
f. Delta modulation
g. Space-Vector PWM (SVM)
h. Sigma-delta modulation
i. Sinusoidal PWM with instantaneous current control

Discussing each of this techniques would be beyond the scope of this report, the SPWM and SV-PWM are priorities and their principles are explained in the next sections.

4.2.2.1 Sinusoidal PWM (SPWM)

Three-phase reference voltages v_a, v_b, and v_c of a variable amplitude A are compared in three separate comparators with a common isosceles triangular carrier wave v_T of a fixed amplitude A_T as shown in Figure 4.4a. The output of comparators 1, 2 and 3 form the gating control signals for the three legs of the inverter formed by switch pairs (S_1, S_4), (S_3, S_6), and (S_5, S_2) which controls the voltage of machine phases. This is shown in Figure 4.4b, the dead-time, to prevent shoot-through fault, is ignored in the figure. The modulation is called sinusoidal PWM because the pulse-width is a sinusoidal function of its angular position in the cycle.

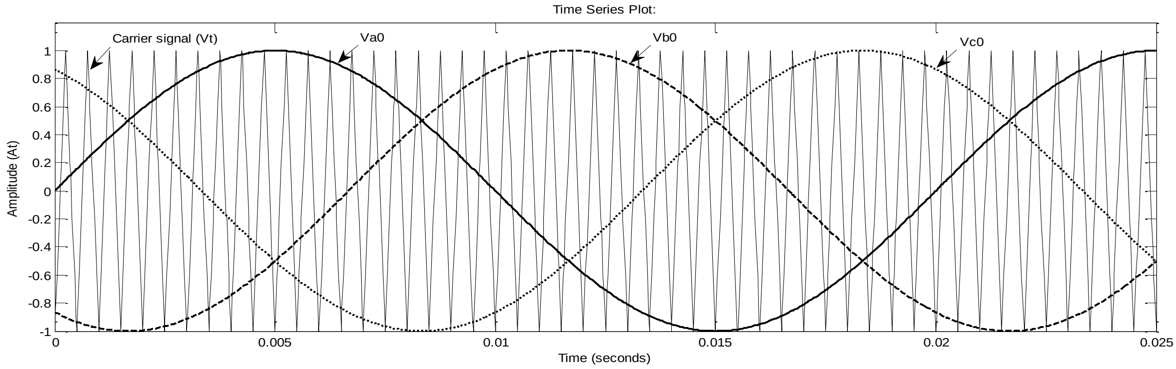

(a) comparison of sinusoidal modulating and carrier wave

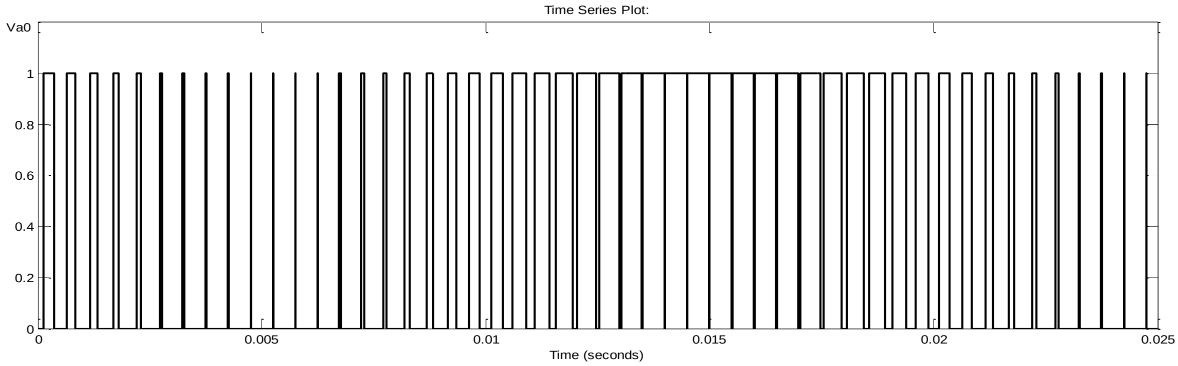

(b) PWM signals

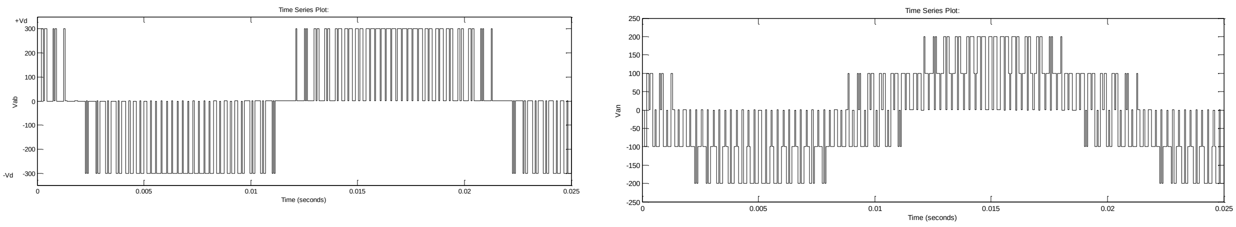

(c) Line and phase voltage waveforms in the MATLAB® environment for v_{ab} and v_{an} respectively

Figure 4.4 Principle of sinusoidal pulse-width modulation

The frequency of the fundamental component of the motor terminal voltage is the same as that of the reference sinusoidal voltages and its amplitude is proportional to the command modulating voltage, hence the frequency of the motor voltage can be changed by changing the frequency of the reference voltages. The typical wave shape of line and phase voltages for an isolated neutral load can be plotted graphically as shown in Figure 4.4c. The Fourier analysis of the v_{ao} wave can be shown to be of the following form [16]:

$$v_{ao} = 0.5mV_d \sin(\omega t + \varphi) + high - frequency(M\omega_c + N\omega)terms \qquad (4.11)$$

where m = modulation index, ω = fundamental frequency (r/s), ω_c = carrier frequency (r/s) and φ = phase shift of output. The modulation index m is defined as

$$m = \frac{A}{A_T} \qquad (4.12)$$

The fundamental (rms) component in the waveform v_{ao} is given by

$$V_1 = \frac{0.5mV_d}{\sqrt{2}} \qquad (4.13)$$

Thus, the fundamental voltage increases linearly with m until m = 1 (i.e. when the amplitude of the reference wave becomes equal to that of the carrier wave). For m > 1 (referred to as overmodulation), the number of pulses in v_{ao} becomes less and the modulation ceases to be sinusoidal PWM. Note that the selection of a carrier frequency depends on the trade-off between inverter loss and the machine loss. Higher carrier frequency increases inverter switching loss but decreases machine harmonic loss. An optimum carrier frequency must be selected such that the total system loss is minimal [16].

The block diagram of laboratory implemented SPWM firing scheme is shown in Figure 4.5a and associated waveforms for the different stages are shown in Figure 4.5b. The circuit schematic in Figure 4.5c shows the generation of the 50Hz sinusoidal wave (designed using modified example parameters for a quadrature oscillator circuit, that generates a simultaneous pair of equal-amplitude sine waves 90^0 out of phase, in Ref [59]) compared with a 4kHz triangular carrier wave. The circuitry was designed using Proteus 8

Professional. The output of the comparator drives gate *S1* and the inverted output drives gate *S2*. The same triangular wave is be used for all three phases. The output of the comparator is high for a duration where the triangular wave is greater than the sinusoidal wave. Output pulses from the comparator is given to switch S_1 and switch S_4 gets the complemented signal.

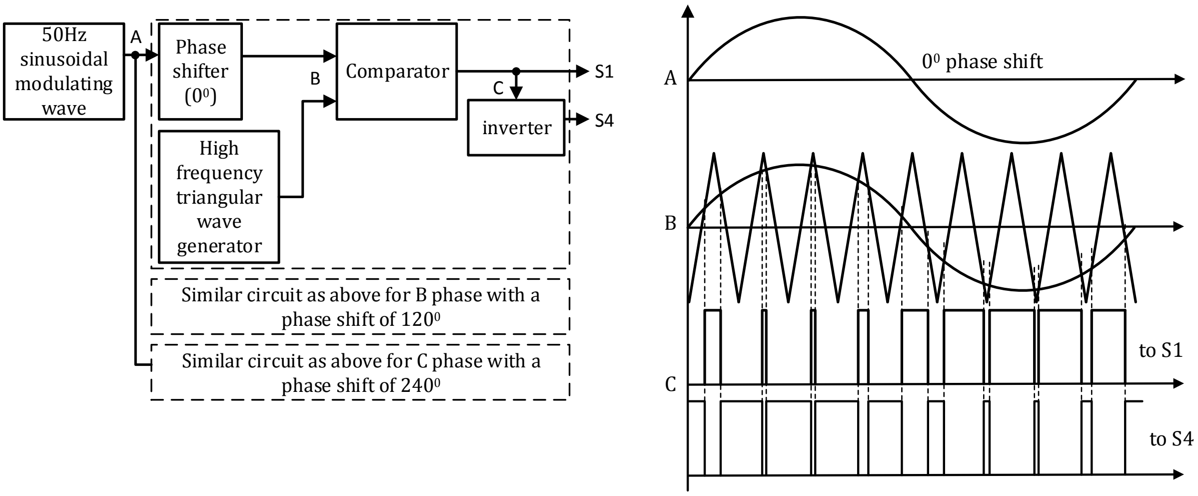

(a) Block diagram (b) Waveforms

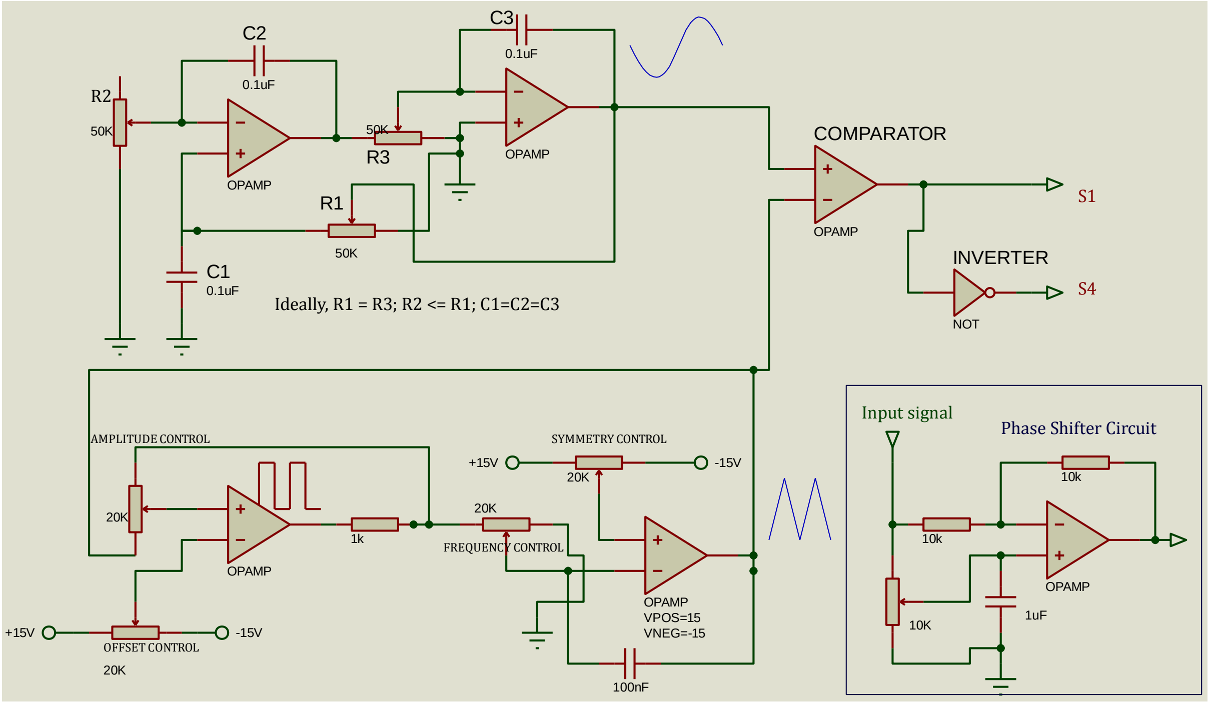

(c) Circuit diagram

Figure 4.5 Laboratory-implemented SPWM circuit

Figure 4.6 shows the PWM signal as captured by an oscilloscope for a single phase of the circuit, line and phase voltages are also illustrated. The oscilloscope graphs show a 50Hz sinusoidal (modulating) wave compared with a high frequency (4kHz) triangular (carrier) wave. Three of these modulating signals phase-shifted by $\frac{2\pi}{3}$, are generated and compared with the carrier signal resulting in PWM gating signals for the top switches and the inverted signals for the bottom set of switches. Output waveforms of the line and phase voltage for a single phase is shown in Figure 4.6c and d respectively. The signal comparison, waveforms and output voltage agree with PWM theory and simulation already discussed.

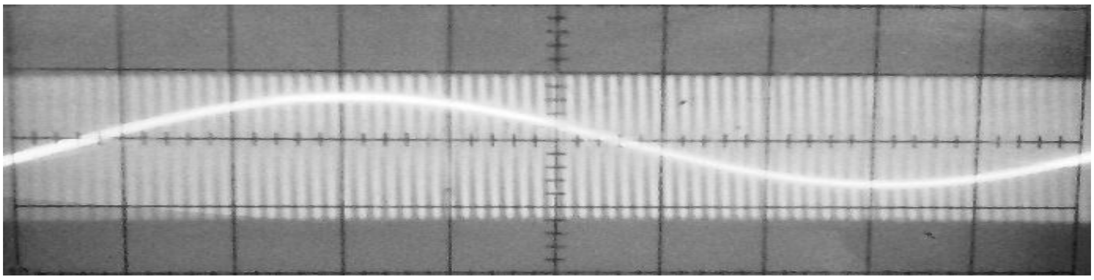

(a) comparison of sinusoidal modulating and carrier wave (shown for 1st phase)

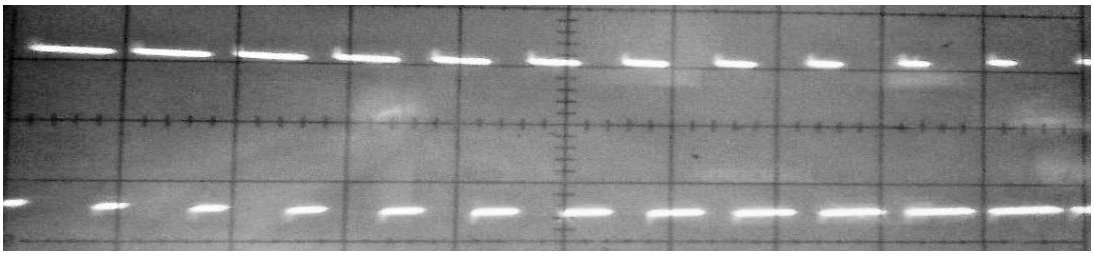

(b) PWM signals

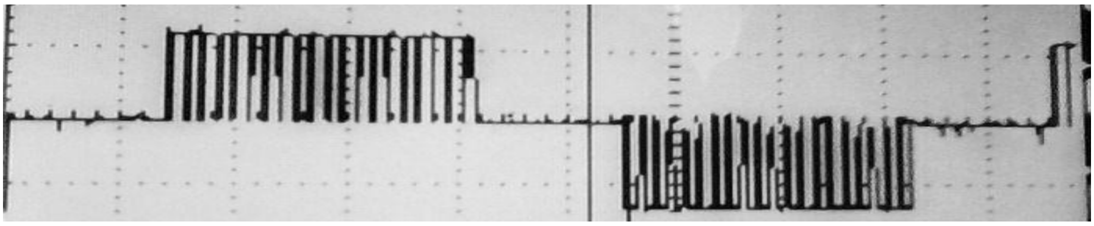

(c) output line voltage

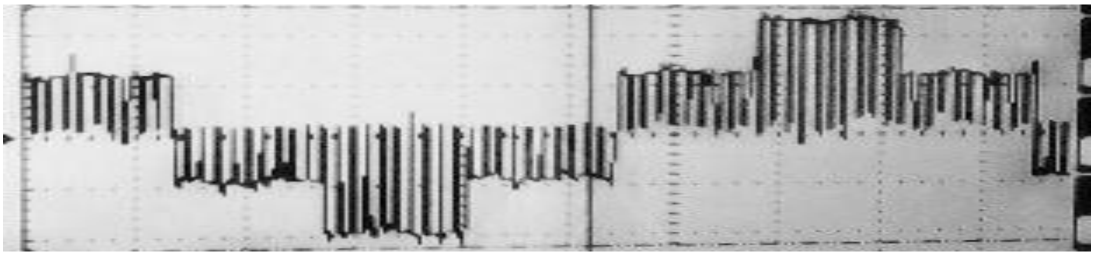

(d) output phase voltage

Figure 4.6 laboratory implemented SPWM signals and waveforms

4.2.2.2 Space Vector PWM (SV-PWM)

The SV-PWM is based on the idea of voltage space vectors which was discussed earlier in the previous chapter in the analysis of the induction machine. In terms of the instantaneous stator phase voltages, the stator space voltage vector is

$$\vec{v}_s^a(t) = v_a(t)e^{j0} + v_b(t)e^{j2\pi/3} + v_c(t)e^{j4\pi/3} \tag{4.14}$$

In terms of the inverter output voltages and assuming the stator neutral as a reference ground, $v_a = v_{aN} + v_N$; $v_b = v_{bN} + v_N$; $v_c = v_{cN} + v_N$; substituting these into Equation (4.14) and recognizing that $e^{j0} + e^{j2\pi/3} + e^{j4\pi/3} = 0$, the instantaneous stator voltage space vector can be written in terms of inverter output voltages as

$$\vec{v}_s^a(t) = v_a N e^{j0} + v_b N e^{j2\pi/3} + v_c N e^{j4\pi/3} \tag{4.15}$$

A switch in an inverter pole of Figure 4.7 is in the "up" position if the pole switching function q = 1, otherwise in the "down" position if q = 0. In terms of the switching functions, the instantaneous voltage space vector can be written as

$$\vec{v}_s^a(t) = v_d\left(q_a e^{j0} + q_b e^{j2\pi/3} + q_c e^{j4\pi/3}\right) \tag{4.16}$$

With three poles, eight switching combinations are possible. In Equation (4.16) the stator voltage vector $\vec{v}_s^a(t)$ can take one of the following seven distinct instantaneous values where in a digital representation, phase "a" represents the least significant digit and phase "c" the most significant digit (i.e. switch combination $\underbrace{011}_{=3}$ is represented as $\vec{v}_3$):

$$\begin{aligned}
\vec{v}_s^a(000) &= \vec{v}_0 = 0\\
\vec{v}_s^a(001) &= \vec{v}_1 = V_d e^{j0}\\
\vec{v}_s^a(010) &= \vec{v}_2 = V_d e^{j2\pi/3}\\
\vec{v}_s^a(011) &= \vec{v}_3 = V_d e^{j\pi/3}\\
\vec{v}_s^a(100) &= \vec{v}_4 = V_d e^{j4\pi/3}\\
\vec{v}_s^a(101) &= \vec{v}_5 = V_d e^{j5\pi/3}\\
\vec{v}_s^a(110) &= \vec{v}_6 = V_d e^{j\pi}\\
\vec{v}_s^a(111) &= \vec{v}_7 = 0
\end{aligned} \tag{4.17}$$

$\vec{v}_0$ and $\vec{v}_7$ are zero vectors, while the resulting instantaneous stator voltage vectors are plotted in Figure 4.7.

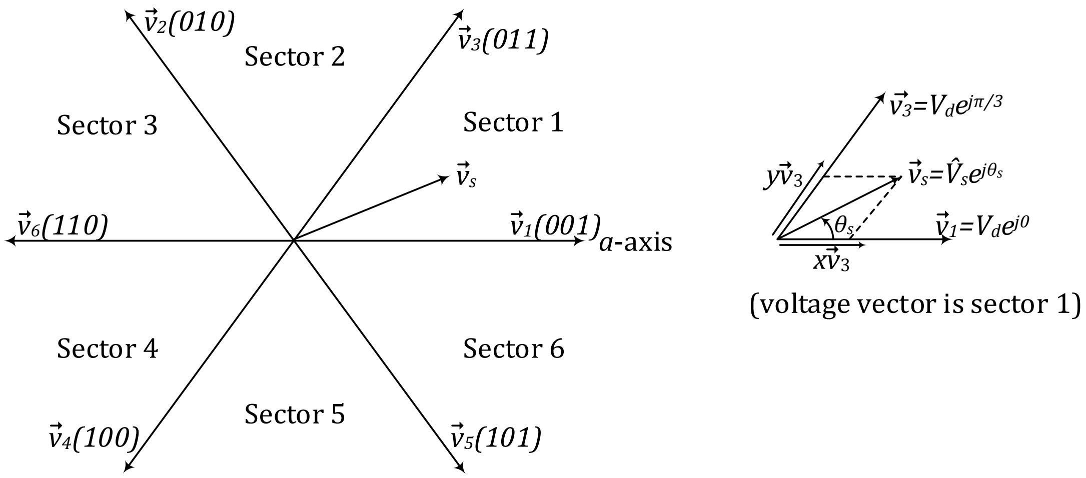

(voltage vector is sector 1)

Figure 4.7 Space vector representation of line-to-neutral voltages in the three-phase voltage-fed inverter [46]

The objective of the PWM control of the inverter switches is to synthesize the desired reference stator voltage space vector in an optimum manner with the following objectives: 1) constant switching frequency f_s, 2) smallest instantaneous deviation from its reference value, 3) maximum utilization of the available dc-bus voltages, 4) lowest ripple in the motor current, and 5) minimum switching loss in the inverter.

The above conditions are generally met if the average voltage space vector is synthesized by means of the two instantaneous non-zero voltage vectors that form the sector and both the zero voltage vectors, such that each transition causes change of only one switch to minimize inverter switching loss.

From Figure 4.7, to synthesize an average voltage vector $\vec{v}_s^a\left(\hat{V}_se^{j\theta_s}\right)$, the adjoining vectors $\vec{v}_1$ and $\vec{v}_3$ are applied with the zero vectors $\vec{v}_0$ and $\vec{v}_7$. Expressing the voltage vectors in terms of their amplitude and phase angles results in:

$$\hat{V}_se^{j\theta_s} = xV_de^{j0} + yV_de^{j\pi/3} \qquad (4.18)$$

By equating the real and imaginary terms on both sides of Equation (4.18) x and y can be solved for to synthesize the desired average space vector in sector 1.

4.3 Constant *V/f* Control

Constant v/f control is well documented in literature, different methods and algorithms has been used in achieving this technique. As early as the late twentieth century microprocessors were used to implement the v/f method of control for the IM [60, 61] with current-limiting features that automatically stops the inverter as soon as the current exceeds a preset upper limit. V/f drives continually gained popularity in adjustable speed applications such as in fans and pumps. Methods and algorithms were developed to effectively apply v/f down to very low frequency ranges with voltage boost capabilities [43, 62, 63, 64] and slip regulation [65]. The twenty-first century witnessed advances in the v/f method and its application combined with other methods such as disturbance observers [66] etc. Some techniques involved modifying the inverter topology and achieving the rectifier and inverter stage with only six switches [67]. Most of these techniques were PWM-based. With respect to electric vehicles, v/f was applied to the control of a battery operated two wheeler (electric wheel chair) [35] and light electric vehicle [68].

The principle of v/f and associated equations has been discussed earlier in section 2.2.1, but the idea is that v/f represents flux [2]. If the voltage is kept constant and frequency is decreased, the flux might increase and the flux in machine may saturate. Thus the voltage and frequency have to be varied such that v/f ratio is kept constant. If voltage is increased, frequency also has to be increased and vice versa. Figure 4.8 shows the torque-speed curve in a v/f drive, developed in MATLAB®. The code can be found in Appendix B along with table of parameters of the modelled induction motor. The maximum torque remains approximately valid, except in the low-frequency region where the air gap flux is reduced by the stator impedance drop ($V_m < V_s$), hence the stator drop must be compensated for by an additional boost voltage in this region [16].

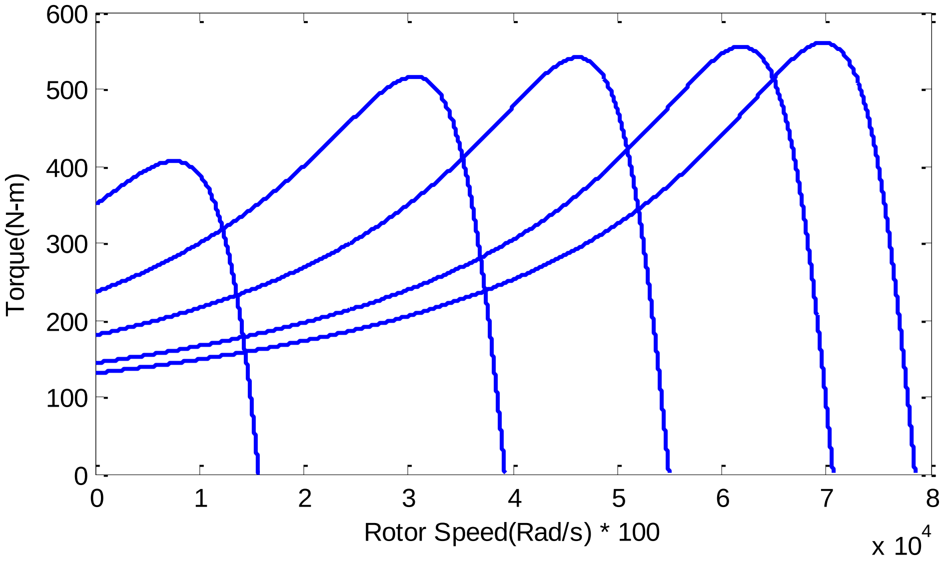

Figure 4.8 Torque-speed curve for the v/f controlled IM drive

Usually the *v/f* drive system constitutes of a rectifier and inverter system [16, 17]. Figure 4.9 shows the configuration of the experimental system which was set up in the Department of Electrical Engineering Laboratory of the University of Nigeria, Nsukka.

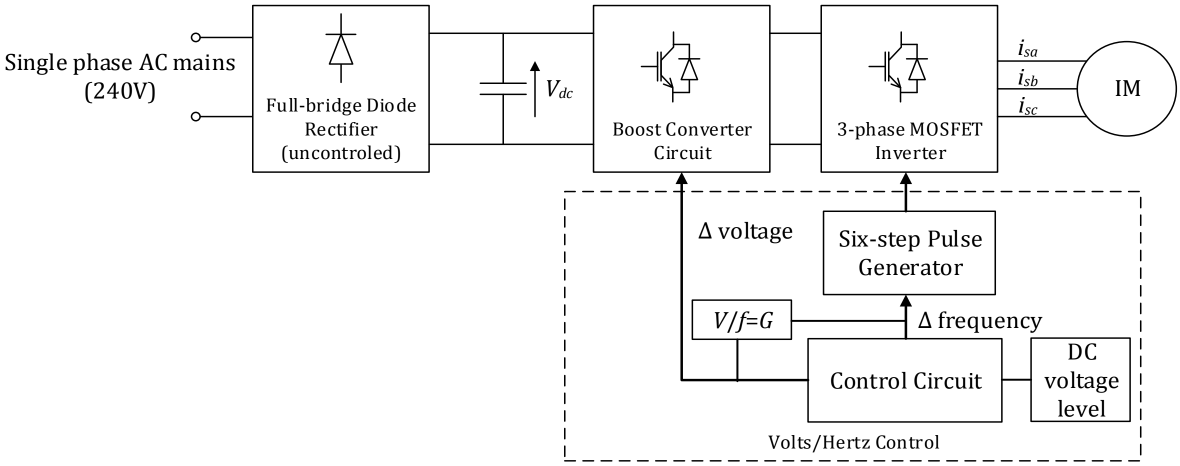

Figure 4.9 Configuration of experimental setup of open-loop v/f control

The power circuit consists of a diode rectifier with a single or three phase ac supply, C filter, a boost converter and square-wave voltage-fed inverter. To maintain the flux at a constant, the stator voltage should be varied in proportion to the supply frequency. The proposed approach is to change the amplitude of the stator voltage from the boost converter and the frequency is changed proportionally within the inverter. Ideally, no feedback signals are needed for the control, but in practical systems measures are taken to avoid overloads. For low speed operation (at reduced frequencies), the stator resistance tends to absorb the major amount of the stator voltage, thus weakening the flux. Hence, the stator voltage must be appropriately boosted so that the rated flux and corresponding full torque become available down to zero speed. Frequencies higher than the rated frequency causes reduction in developed torque which is as a consequence of a reduced magnetizing current, i.e. weakened magnetic field.

In the operation of the v/f drive in Figure 4.9, the DC voltage level is the primary control variable it is compared with a sawtooth generator to change the amplitude of the voltage input to the inverter and also passed through a voltage controlled oscillator (which converts voltage to frequency) in order to make available a variable frequency control of the inverter. Change in this dc level varies the voltage and frequency proportionally at a constant ratio.

4.4 Design, Modelling and Implementation of V/f Control Scheme

Discussed, in this section, is the design and simulation of v/f and eventual laboratory implementation. The square-wave mode of operation was chosen for its simplicity and availability of electrical components and materials. Prior to the design, simulation of open-loop v/f was carried out on the MATLAB® platform. Model simulation is presented in Figure 4.10 and the outputs is discussed in the results section. The six-step induction motor drive block is a high-level schematic made up of the induction motor block, the three-phase inverter block, the rectifier block, the bus voltage regulator block and the six-step generator block. Figure 4.10a shows the whole MATLAB® model, 4.10b illustrates the six-step generator block The six-step generator illustrated in the following figure contains six comparators to produce the six-step switching waveforms.

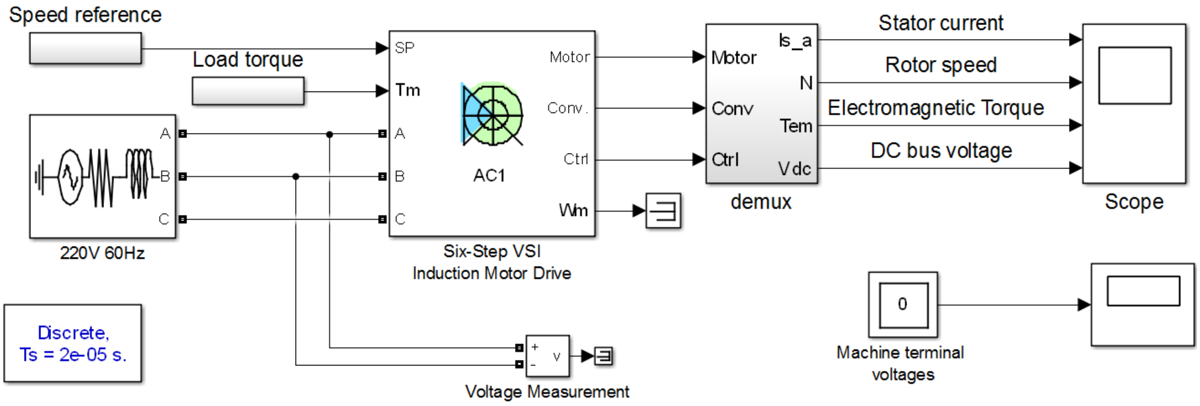

(a) MATLAB® model of the six-step v/f drive for induction motor

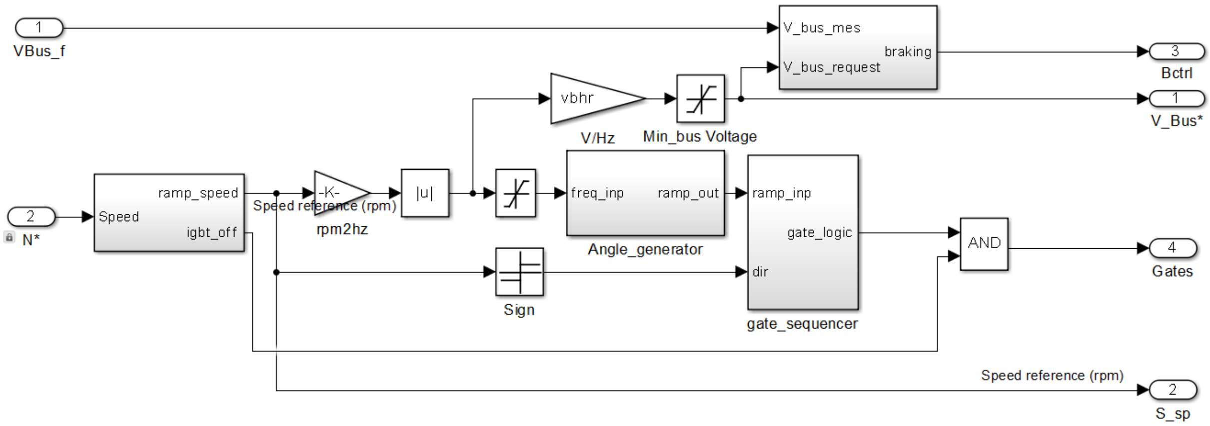

(b) MATLAB® model of the six-step generator block

Figure 4.10 MATLAB model of a v/f drive

4.4.1 Proposed *V/f* Methodology

The schematic diagram of the proposed system to obtain a constant *v/f* ratio is shown in Figure 4.11. The dc voltage level controls the voltage amplitude and frequency of the inverter. This occurs simultaneously but for ease of explanation it would be discussed in two stages, (i) boost converter and, (ii) inverter frequency stages. At the boost converter stage, the dc level controls the change in amplitude of the boost converter which is an input to the inverter, and its rms is the fundamental output voltage of the inverter. The output voltage of the inverter is the voltage at the stator of the induction motor. The dc level also effects frequency changes within the inverter. It is fed into a VCO that converts voltage to frequency used to clock a set of flip flops configured to generate symmetrical 3-phase balanced square wave logic signals for driving the inverter. Thus there is a simultaneous and proportional change in the voltage and frequency output of the inverter.

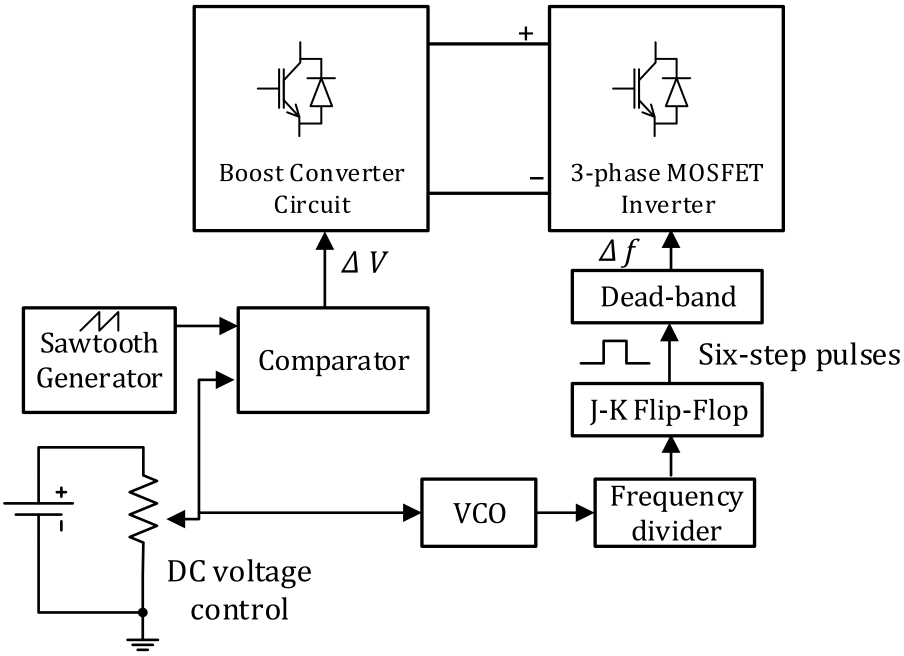

Figure 4.11 Block diagram of proposed control circuit

4.4.2 Control Circuit Design and Implementation

The basic components used in achieving the control circuit are the dc voltage level control, the sawtooth generator and comparator circuits for control of the boost converter, the voltage controlled oscillator (VCO) that converts voltage to frequency thus generating a 0 to 1Khz square wave signals, the frequency divider that divides the high frequency signal from the timer to output up to 50Hz signals (it can go up to 100Hz) for clocking the flip flops. The flip-flops are configured such that their outputs are 120^0 phase shifted. They produce the switching signals for the upper and lower switches of the inverter.

A. Boost Converter firing logic circuitry

The block diagram of the boost converter and logic circuit has been illustrated in Figure 4.11, the boost circuit and its firing logic circuit is shown in Figure 4.12a and b respectively. The output dc voltage V_O of the boost converter is always higher than the input or source dc voltage V_S for steady-state operation. The converter consists of an inductor L, a power MOSFET, a fast switching diode, a filter capacitor, and a load, in this case, the 3-phase inverter and induction motor are connected as load. The switch $Q1$ is turned on and off at the switching frequency $f_s = 1/T$ with the ON duty ratio $D = t_{on}/T$, where t_{on} is the time interval when the switch S is ON. The principle of operation of the boost converter is summarised in Equation 4.19 [69, 70] as:

$$V_o = \frac{V_s}{1-D} \tag{4.19}$$

So that as D varies from 0 to 1, V_o varies from V_s to theoretical infinity (based on ideal components), real components will prevent such an occurrence. In this case, the boost converter is designed to operate from a supply voltage of about 120V to about 600V output voltage. This provides an inverter output voltage of 415V rms for such rated induction motor.

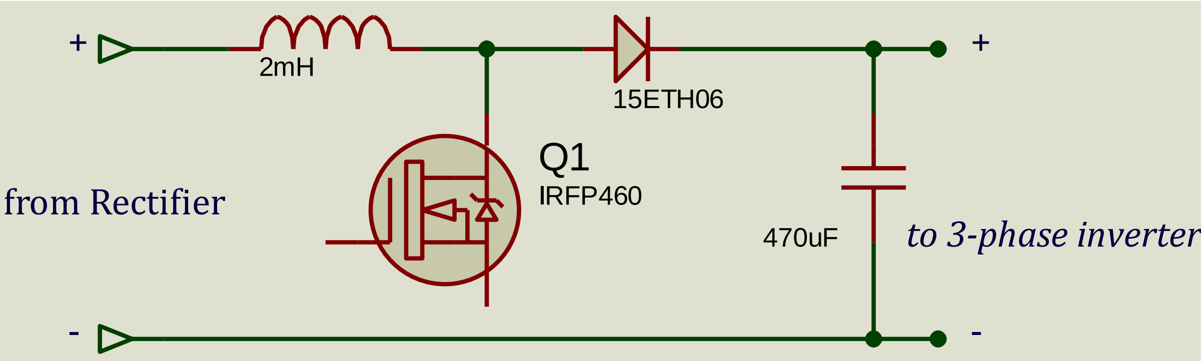

(a) boost dc-dc converter

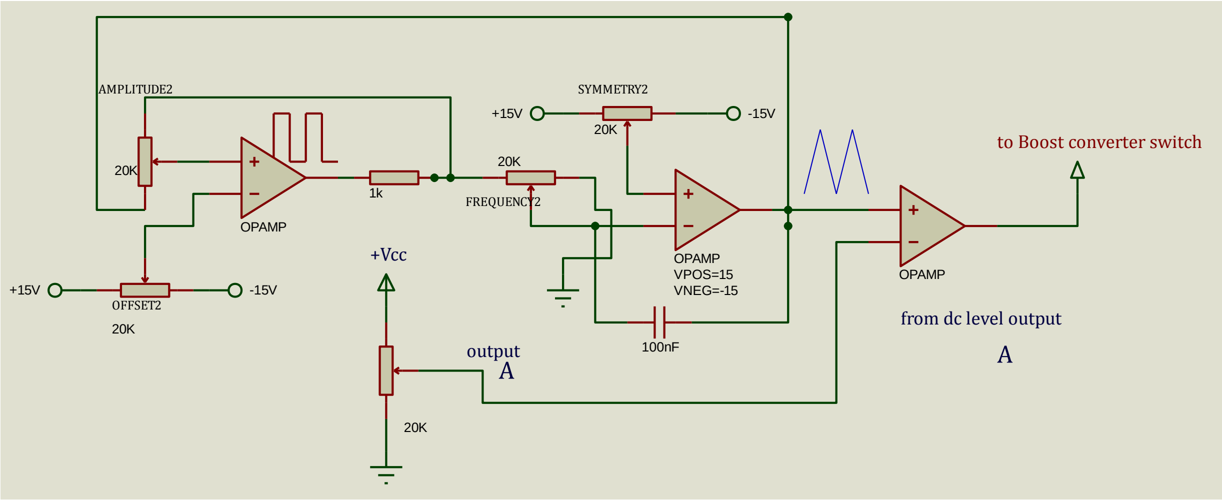

(b) firing logic circuit for boost dc-dc converter

Figure 4.12 Boost converter and logic control circuit

B. Voltage controlled oscillator (VCO)

The voltage controlled oscillator (VCO) was designed using operational amplifiers (opamp). The output waveform of this VCO is a square-wave. Figure 4.13 shows the VCO circuit. The leftmost stage, with opamp A_1 is basically an inverting, summing amplifier with the feedback resistor replaced by capacitor C_1. The circuit can be called an integrator. A linear ramp of voltage is expected across C_1. A_2 is configured as a voltage comparator circuit with the upper and lower thresholds established by diodes D_1 and D_2 and amplifier A3 is connected as an inverting summing amplifier. The frequency of operation is determined by the time it takes C_1 to charge to the threshold levels of A_2. Once the circuit components have been fixed, the only thing that determines frequency is the value of input voltage *(+V_{IN}).* This is why it is referred to as, voltage-controlled oscillator [71] . A triangle-wave (or double ramp) signal may be taken from the output of A1.The output of A2 provides a square-wave output. The output of A2 is what serves as the clock input to the flip flops.

Numerical analysis: The practical design requirements are;

i. Input voltage range: 0 to 12volts DC (from logic power supply)
ii. Ramp output voltage: ±8volts
iii. Frequency range: 0 to 1Khz. The frequency of I khz is chosen so that the a divide-by-ten circuit can be easily designed to divide the frequency to as low as 100Hz. This gives a variable frequency output of 0 to 100Hz .

The components considered are D_3, R_3, R_5, D_5, D_6, R_6 and D_4. The gain of A_3 is ensured to be -1, and -2 for the +v_{in} and A_2 signals respectively.

1. *Selecting the zener diodes.*

The voltage rating of D_2 plus the forward voltage drop of D_1 determines the upper limit of ramp output voltage, also, D_1 plus the forward voltage drop of D_2 determines the lower limits of ramp output voltage. Selecting the voltage drop of D_1 and D_2, where V_{ramp} is the amplitude of the ramp voltage and 0.6 is the voltage drop of a diode,

$$V_{D1} = -V_{ramp} + 0.6;\ V_{D2} = +V_{ramp} - 0.6 \qquad (4.20)$$

For this design, the required zener ratings are:

$$V_{D1} = -8V + 0.6V = -7.4V \; and \, V_{D2} = +8V - 0.6 = +7.4V \qquad (4.21)$$

The commercially available component satisfying this rating is 1N4737 or 1N5236.

2. Compute R2

Resistor R2 is a current limiting resistor that keeps current through D1 and D2 within safe limits. Designing for a current through zener diodes can be obtained by the following expression [71]:

$$I_Z = 10I_{ZK} \qquad (4.22)$$

where I_{ZK} is knee current which according to datasheet is 0.25mA

Therefore, R2 can be determined by the following:

$$R_2 = \frac{V_{sat} - V_Z - 0.6}{I_Z} \qquad (4.23)$$

where V_{sat} is the highest saturation voltage for opamp A2 (±13V from datasheet), V_Z is the lower of the two zener voltages (if not equal) and I_Z is the zener current obtained from Equation (4.22). Therefore,

$$I_Z = 10 \times 0.25mA = 2.5mA \text{ and,} \qquad (4.24)$$

$$R_2 = \frac{13V - 7.4V - 0.6}{2.5mA} = 2K\Omega \qquad (4.25)$$

3. Compute R1 and C1.

Once, the zeners has been selected, the values of R1 and C1 determine the frequency for a given voltage. The product of R1 C1 can be found by the following equation [71]:

$$R_1C_1 = \frac{V_{in(max)}}{2f_{Hi}V_{ramp}} \qquad (4.26)$$

where $V_{in(max)}$ is the highest input voltage (12V in this case), f_{Hi} is the highest frequency of oscillation (1kHz in this case). Therefore,

$$\frac{12}{2 \times 1kHz \times 16V} = R_1C_1 = 375\mu s \qquad (4.27)$$

According to [71] the VCO must satisfy the condition that R1 must be in the range of 1 – 470kΩ, C1 > 470pF and ratio of R1 to R4, R1:R4 = 2:1. So, if we select R1 = 2k, and $R_1 C_1$ = 375μs, then

$$C_1 = \frac{375\mu s}{R_1}, = \frac{375\mu s}{2k} = 0.1\mu F. \quad (4.28)$$

4. Compute R4

R4 must be exactly one-half the value of R1, i.e. $R_4 = R_1/2$, therefore, $R_4 = 2k\Omega/2 = 1.0k\Omega$

The circuit (designed in Proteus) is presented in Figure 4.13.

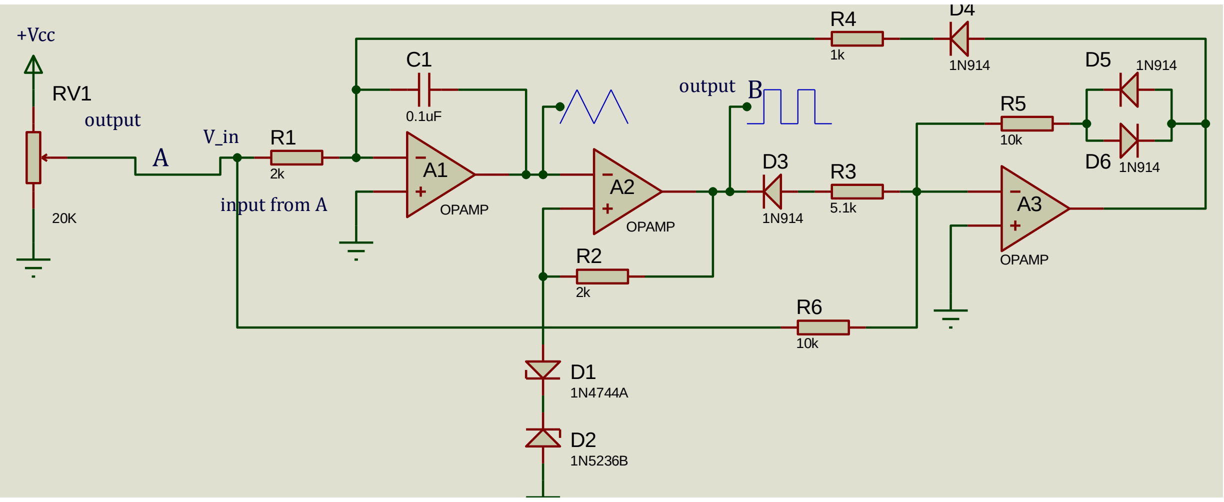

Figure 4.13 VCO circuit diagram

C. Frequency divider

The decade counter HCF4017BE can be connected as a divide-by-n frequency divider. For the purpose of this setup, it is connected as a divide-by-10 frequency divider as described in its datasheet [72]. Its output is used as a clock signal for the JK flip flops. To avoid the intrusion of unwanted signals (known as noise) at higher frequencies, which have the potential of disrupting the clocking signal thus producing undesired results, a simple low-pass filter (known as integrator) is designed to stop the noise at high frequency and pass the signal at low frequency [59, 73, 74]. The buffer at the output of the filter is a single input circuit that does not alter its input signal, rather it provides increased current or voltage drive capabilities [75, 76]. It allows a weaker signal to drive loads. In this case the 4050 buffer IC is used to increase the voltage drive capability of the signal for clocking. Circuit is shown in Figure 4.14

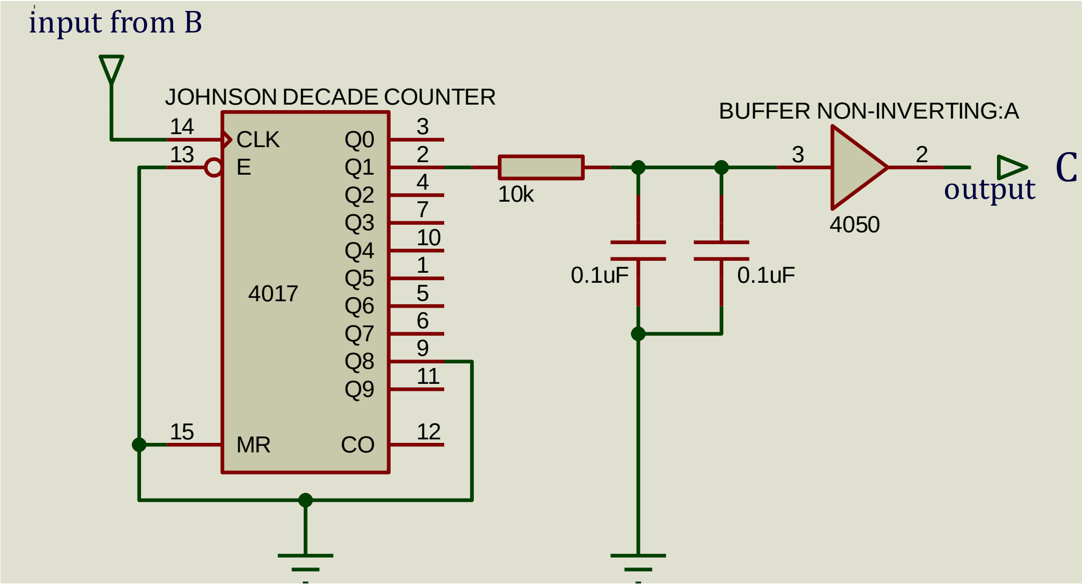

Figure 4.14 Frequency divider circuit with a low-pass filter and buffer

D. JK flip flop

The JK flip flop [77] was designed as a counter that generates a symmetrically balanced set of 3-phase signals, the firing signal sequence for three-phase switching. Firing signals for a three-phase are in the sequence: 561→612→123→234→345→456. Signals 4 6 2 are complements of 1 3 5 respectively. Figure 4.15 and 4.16 shows the power circuit and timing diagram respectively.

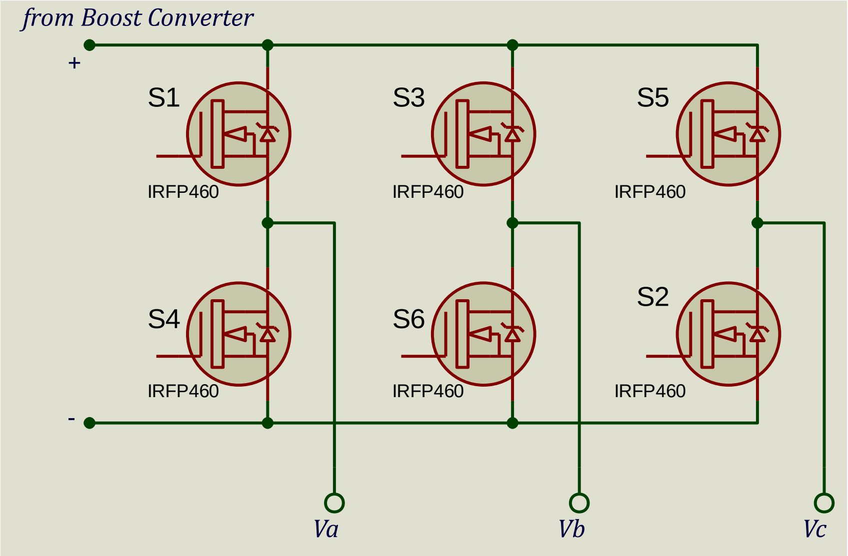

Figure 4.15 3-phase inverter power circuit

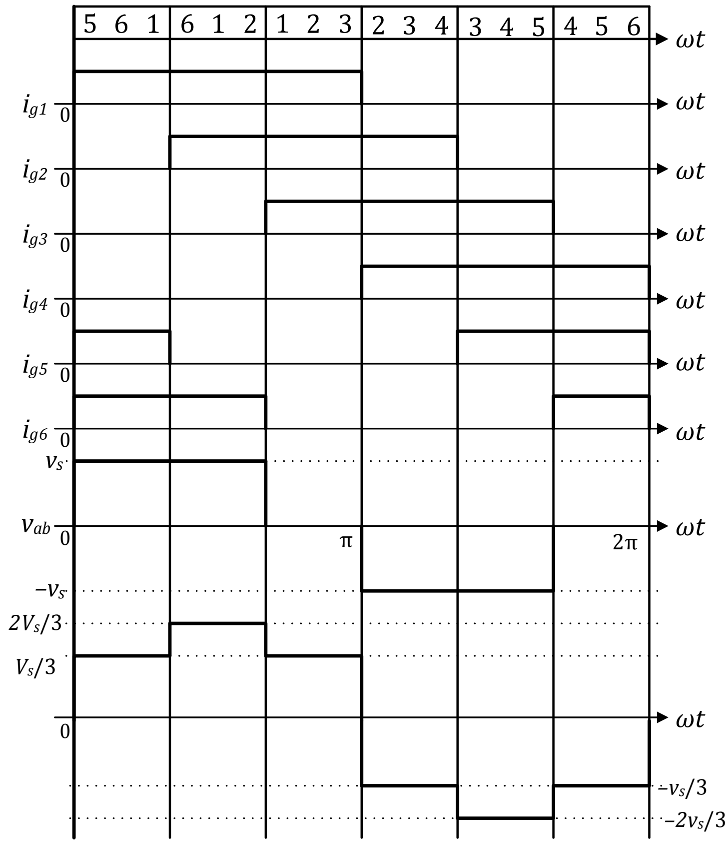

Interval	v_a	v_b	v_c	v_{ab}	v_{an}
I	V_s	0	V_s	V_s	$V_s/3$
II	V_s	0	0	V_s	$2V_s/3$
III	V_s	V_s	0	0	$V_s/3$
IV	0	V_s	0	$-V_s$	$-V_s/3$
V	0	V_s	V_s	$-V_s$	$-2V_s/3$
VI	0	0	V_s	0	$-V_s/3$

Figure 4.16 Timing diagram showing conventional waveforms and firing sequence

Hence, we use a nomenclature such that the signals for the top switches S_1, S_3, S_5 = A B C = 1 1 1. Therefore, from Figure 4.16 the state graph for the firing sequence is: 101→100→110→010→011→001. This is represented in the state transition diagram presented in Figure 4.17. The JK flip flop excitation table is presented in Table 4.1 and the corresponding transition table presented in Table 4.2. The Karnaugh map representation is also presented in Figure 4.18.

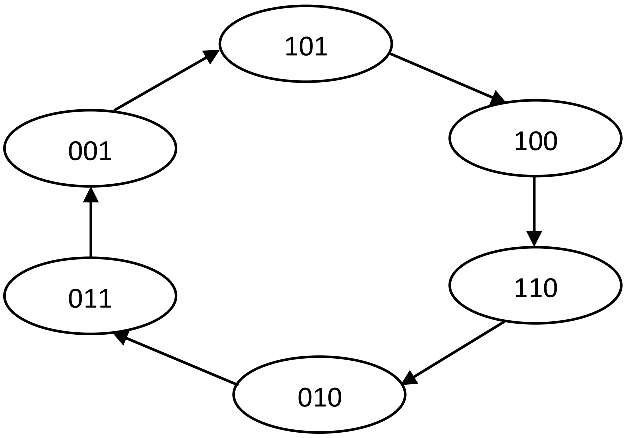

Figure 4.17 State transition diagram

Table 4.1 J-K Excitation table

PS*	NS*	Required Inputs	
Q	Q^+	J	K
0	0	0	x
0	1	1	x
1	0	X	1
1	1	X	0

* PS = Present State, NS = Next State

Table 4.2 State transition table

PS			NS			FF					
A	B	C	A^+	B^+	C^+	J_A	K_A	J_B	K_B	J_C	K_C
0	0	0	-	-	-	X	x	x	x	x	x
0	0	1	1	0	1	1	x	0	x	x	0
0	1	0	0	1	1	0	x	x	0	1	x
0	1	1	0	0	1	0	x	x	1	x	0
1	0	0	1	1	0	X	0	1	x	0	x
1	0	1	1	0	0	X	0	0	x	x	1
1	1	0	0	1	0	X	1	x	0	0	x
1	1	1	-	-	-	X	x	x	x	x	x

where: PS = Present State, NS = Next State, FF = flip-flop outputs

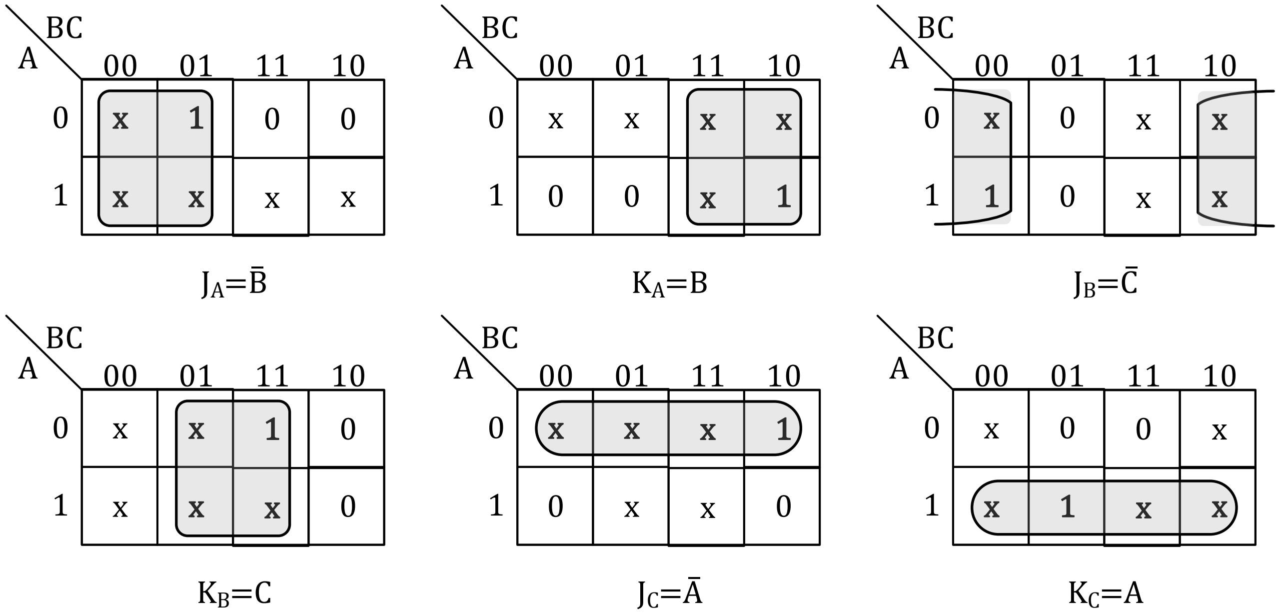

A \ BC	00	01	11	10
0	x	1	0	0
1	x	x	x	x

$J_A=\bar{B}$

A \ BC	00	01	11	10
0	x	x	x	x
1	0	0	x	1

$K_A=B$

A \ BC	00	01	11	10
0	x	0	x	x
1	1	0	x	x

$J_B=\bar{C}$

A \ BC	00	01	11	10
0	x	x	1	0
1	x	x	x	0

$K_B=C$

A \ BC	00	01	11	10
0	x	x	x	1
1	0	x	x	0

$J_C=\bar{A}$

A \ BC	00	01	11	10
0	x	0	0	x
1	x	1	x	x

$K_C=A$

Figure 4.18 Karnaugh mapping

The wiring diagram for the JK flip flop to achieve the 3 phase sequence is presented in Figure 4.19. The connections are made based on the results obtained from the Karnaugh map.

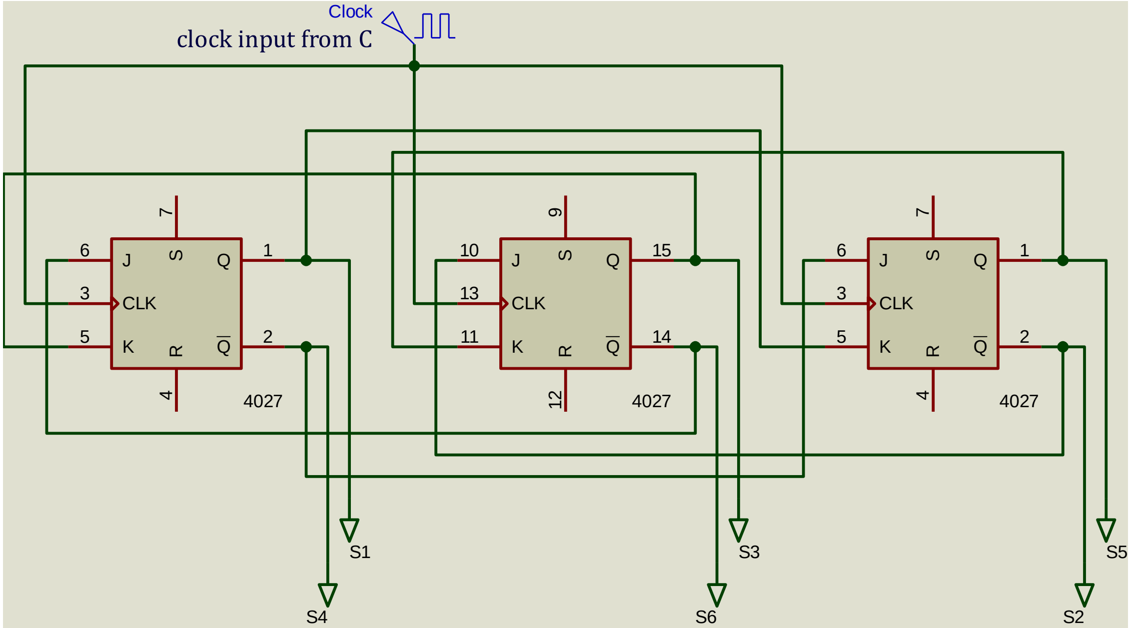

Figure 4.19 JK flip flop connection to obtain 6-pulse for three-phase inverter

E. Dead time circuit

Ideally the switches on one inverter leg should turn On and OFF in zero time, but this does not occur in real components. This causes a shoot-through fault were at the point of turning ON and OFF of complementary switches, there is a point were both switches are ON. This causes a short-circuit and can damage the switches and ruin inverter operation. To avoid shoot-through faults, a *dead-time* is designed to delay the signal (typically a few µs) [16]. This is shown in Figure 4.20.

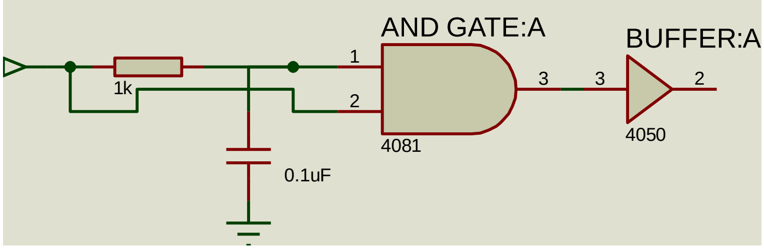

Figure 4.20 Dead time or delay circuit

The complete circuit diagram is shown in Figure 4.21 and Figure 4.22 shows the system during the process of design in the laboratory.

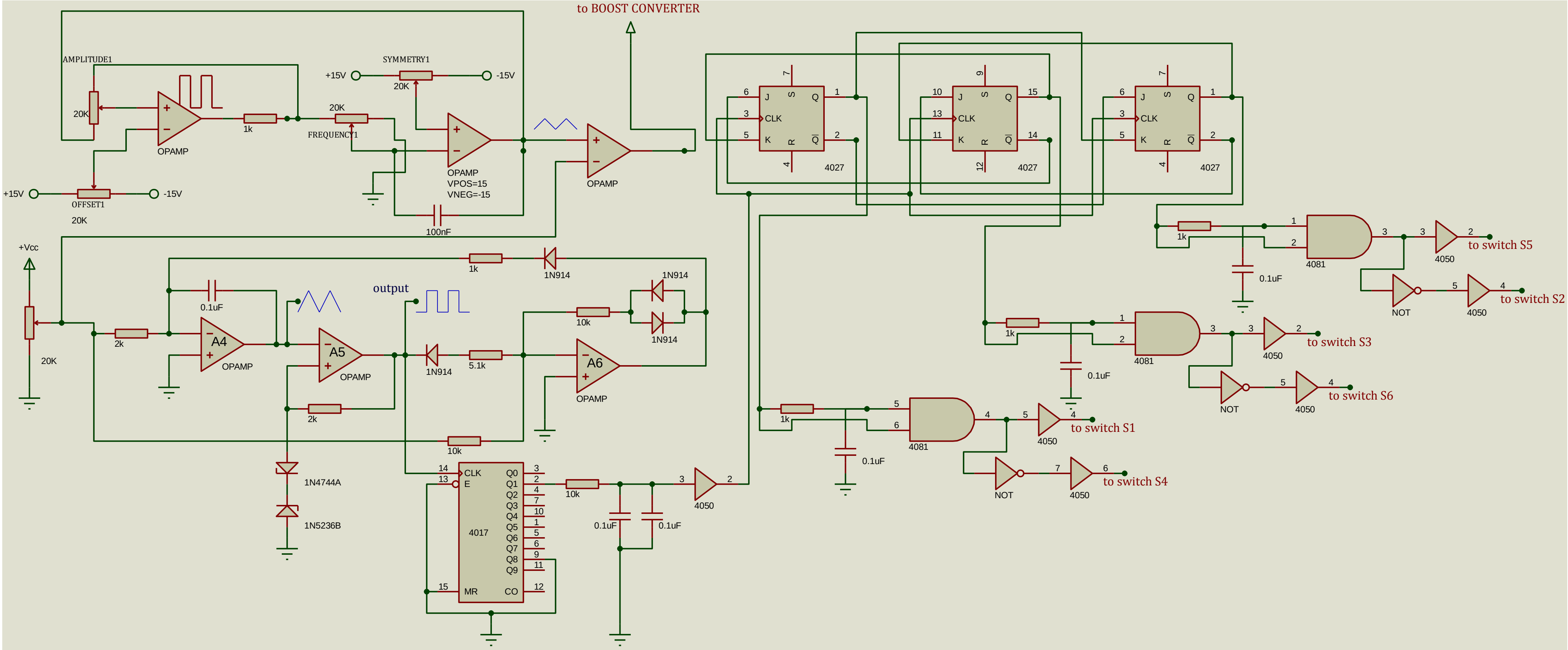

Figure 4.21 Full v/f control circuit

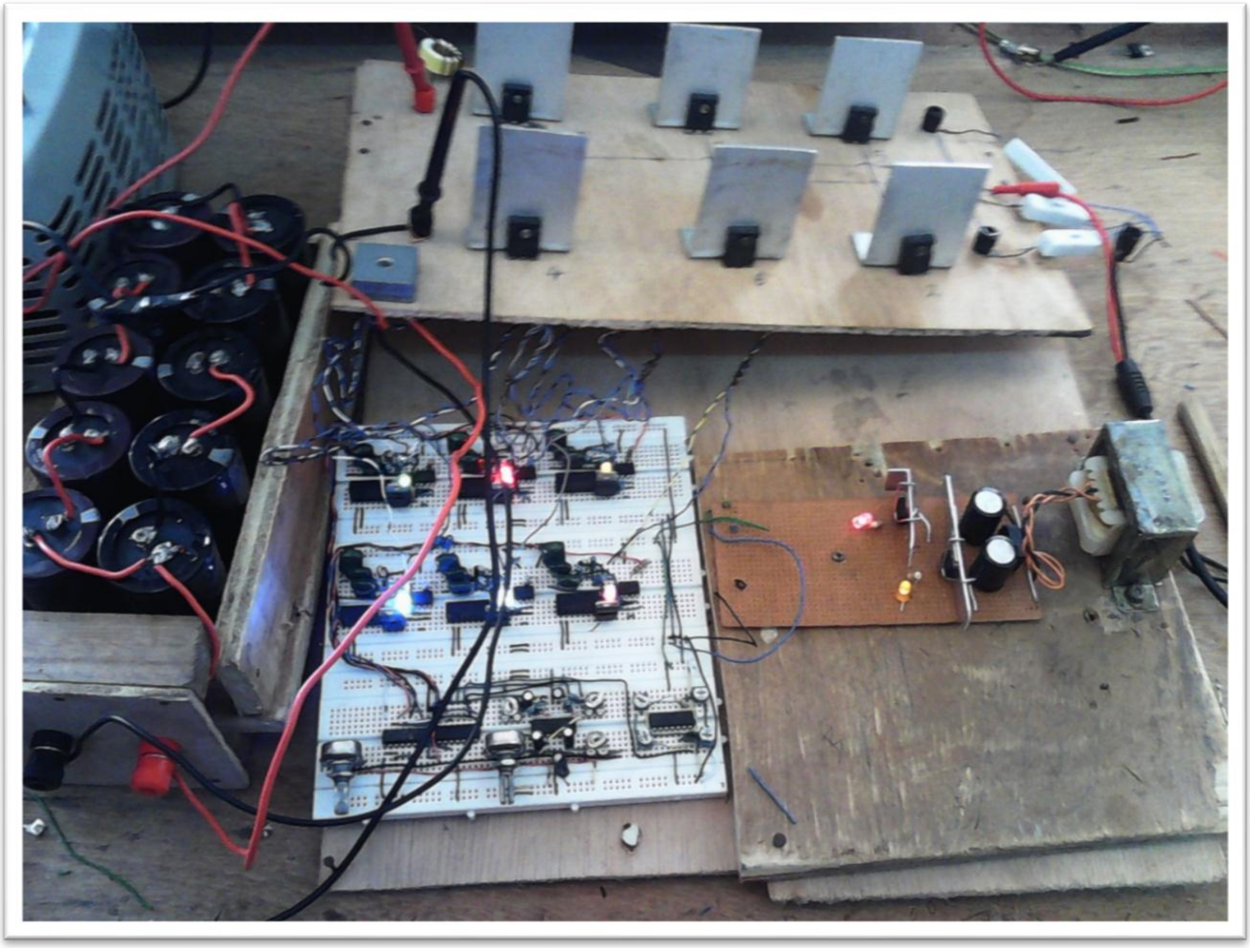

Figure 4.22 Laboratory setup

The circuit was implemented in the laboratory, the inverter was energized with a three-phase resistive load of about 100Ω and the signals were measured out from an oscilloscope. The voltage level input to the timer and the frequency change was measured and plotted on a graph, to be sure there was a simultaneous change in the two parameters for a 415V/50Hz rated machine. The ratio is 8.3, in the logic circuit design, the amplitude of the voltage was a variable value from 0V – 10V, and this effected changes in the frequency. The result is plotted and discussed in the experimental results section of Chapter 6.

With satisfactory waveforms and v/f ratio, the system was hooked up to a three-phase induction machine and driven at different speeds.

Chapter 5

5 Variable Structure Direct Torque Control of the Induction Motor

5.1 Sliding Mode Direct Torque Control

In high-performance drive systems, in which control variables include the torque developed in the motor, vector control methods are necessary [17]. In chapter two the DTC control technique was introduced and the principle of encoder-less operation was enumerated. Also the sliding mode theory was introduced and conditions for existence and stability was presented. The analysis of the IM carried out in chapter 3 establishes the mathematical requirement for the implementation of the sliding mode DTC control scheme. Two different sliding surfaces for flux and torque will be designed so that the error between reference and actual values are driven to respective sliding surfaces where the error is enforced to zero.

The proposed schematic, of the drive system is presented in Figure 5.1 comprising of the power circuit, the co-ordinate transforms from *dq* to *abc* coordinates, the estimator block and the sliding mode controller. The estimator and sliding mode controller block is explained in the next sections.

5.2 Encoderless Direct Torque Control Design

5.2.1 Calculation of $\vec{\lambda}_s$, $\vec{\lambda}_r$, $\vec{T}_{em}$, and $\vec{\omega}_m$, in the Estimator Block of DTC

Calculations required for the estimator section of the DTC will be carried out in this section [46].

5.2.1.1 Calculation of the Stator Flux $\vec{\lambda}_s$

The stator voltage equation with the stator a-axis as the reference is

$$\vec{v}_s = R_s\vec{\imath}_s + \frac{d}{dt}\vec{\lambda}_s \tag{5.1}$$

From Equation (5.1), he stator flux linkage space vector at time t can be calculated in terms of the flux linkage at the previous sampling time as

$$\vec{\lambda}_s(t) = \vec{\lambda}_s(t - \Delta T) + \int_{t-\Delta T}^{t} (\vec{v}_s - R_a\vec{\imath}_s).\,d\tau = \vec{\lambda}_s e^{j\theta_s} \tag{5.2}$$

where τ is the variable of integration.

The applied stator voltage remains constant during the sampling interval ΔT and the stator current value is that measured at the previous step.

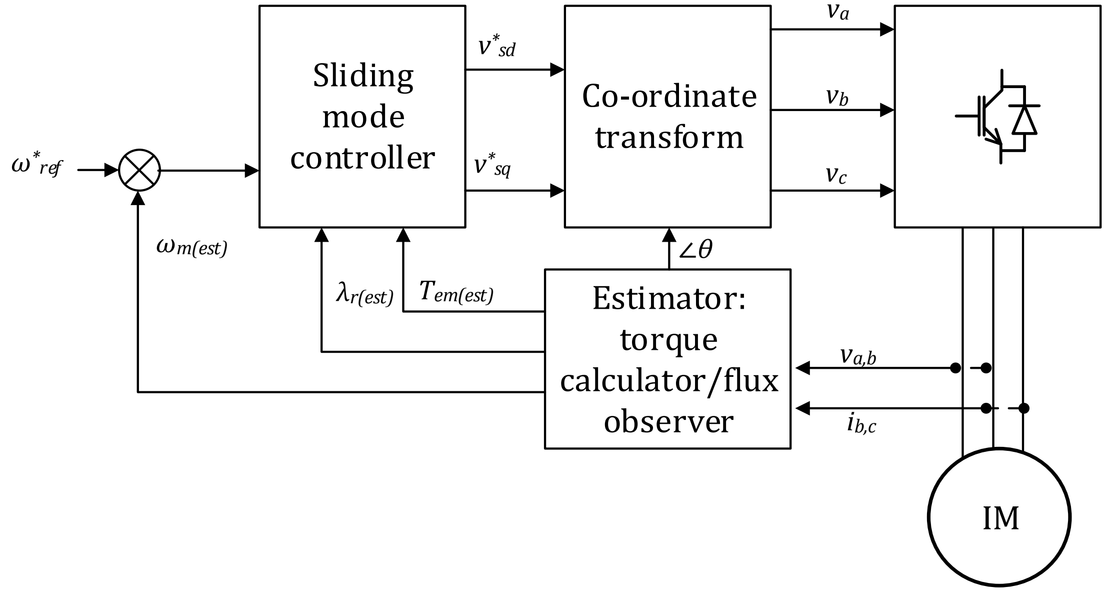

Figure 5.1 Block diagram of speed sensorless DTC drive system

5.2.1.2 Calculation of the Rotor Flux $\vec{\lambda}_r$

From chapter 3, the stator flux was established as:

$$\vec{\lambda}_s = L_s\vec{\imath}_s + L_m\vec{\imath}_r \tag{5.3}$$

and

$$\vec{\lambda}_r = L_r\vec{\imath}_r + L_m\vec{\imath}_s \tag{5.4}$$

Calculating $\vec{\imath}_r$ from Equation (5.3)

$$\vec{\imath}_r = \frac{\vec{\lambda}_s}{L_m} - \frac{L_s}{L_m}\vec{\imath}_s \tag{5.5}$$

and substituting it into Equation (5.4)

$$\vec{\lambda}_r = \frac{L_r}{L_m}\vec{\lambda}_s - \frac{L_rL_s}{L_m}\vec{\imath}_s + L_m\vec{\imath}_s = \frac{L_r}{L_m}\left[\vec{\lambda}_s - L_s\vec{\imath}_s \underbrace{\left(1 - \frac{L_m^2}{L_sL_r}\right)}_{=\sigma}\right] \tag{5.6}$$

where σ is the leakage factor.

Therefore, the rotor flux linkage space vector in Equation (5.6) can be written as

$$\vec{\lambda}_r = \frac{L_r}{L_m}\left(\vec{\lambda}_s - \sigma L_s \vec{i}_s\right) = \vec{\lambda}_r e^{j\theta_r} \tag{5.7}$$

Similar to Equation (5.2) for the stator flux linkage vector, the rotor flux linkage space vector can be expressed (with respect to the A-axis) as follows, recognizing rotor voltage in a squirrel-cage rotor is zero

$$\vec{\lambda}_r^A(t) = \vec{\lambda}_r^A(t - \Delta T) + \int_{t-\Delta T}^{t} (-R_r \vec{i}_r^A).\, d\tau = \vec{\lambda}_r e^{j\theta_r^A} \tag{5.8}$$

Observation: rotor flux changes very slowly with time (in amplitude and in phase angle with respect to the rotor A-axis) only due to a small drop across the rotor resistance.

5.2.1.3 Calculation of the Electromagnetic Torque T_{em}

Electromagnetic torque developed by the motor can be estimated in terms of the stator flux and stator current, or in terms of the stator flux and the rotor flux. For torque estimation, the expression in terms of the estimated stator flux linkage and the measured stator currents will be used and is presented as

$$T_{em} = \frac{p}{2} Im\left(\vec{\lambda}_s^{conj} \vec{i}_s\right) \tag{5.9}$$

which does not depend on the rotor flux linkage (rotor flux linkage in Equation (5.8) depends on correct estimates of L_s, L_r, and L_m).

5.2.1.4 Calculation of the Rotor Speed ω_m

A much slower sampling rate with a sampling interval ΔT_ω, for example equal to $1ms$ can be used for estimating the rotor speed. The speed of the rotor flux in electrical rad/s is calculated from the phase angle of the rotor flux space vector in Equation (5.8) as follows:

$$\omega_r = \frac{d}{dt}\theta_r = \frac{\theta_r(t) - \theta_r(t - \Delta T_\omega)}{\Delta T_\omega} \tag{5.10}$$

Recalling torque equation developed in chapter 3, the slip is calculated as follows:

$$T_{em} = \frac{P}{2}\lambda_{rd}\left(\frac{L_m}{L_r} i_{sq}\right) \tag{5.11}$$

and

$$\omega_{slip} = R_r \frac{1}{\lambda_{rd}} \left(\frac{L_m}{L_r} i_{sq} \right) \tag{5.12}$$

Calculating i_{sq} from Equation (5.12) and noting that in the model with the d-axis aligned with the rotor flux linkage, $\lambda_{rd} = \sqrt{2/3}\,\hat{\lambda}_r$, the slip speed in electrical rad/s is

$$\omega_{slip} = \frac{2}{p} \left(\frac{3}{2} R_r \frac{T_{em}}{\hat{\lambda}_r^2} \right) \tag{5.13}$$

Therefore, the rotor speed can be estimated from Equation (5.10) and (5.13) as

$$\omega_m = \omega_r - \omega_{slip} \tag{5.14}$$

where all speeds are in electrical radians/s. In a multi-pole machine with $p \geq 2$

$$\omega_{mech} = (2/p)\omega_m \tag{5.15}$$

5.3 Sliding Mode Controller Design

The motor torque and amplitude of rotor flux will be controlled directly by the inverter On-Off gating signals without explicitly involving the stator current control and conventional PWM techniques. Figure 5.2 shows the structure of the sliding mode controller for the DTC without the use of a switching table [78]. Recall that earlier, we had estimated the torque and flux from the DTC system. The next step is to design the sliding surfaces for torque and flux so that the system have the desired dynamic behaviour when restricted to S [56].

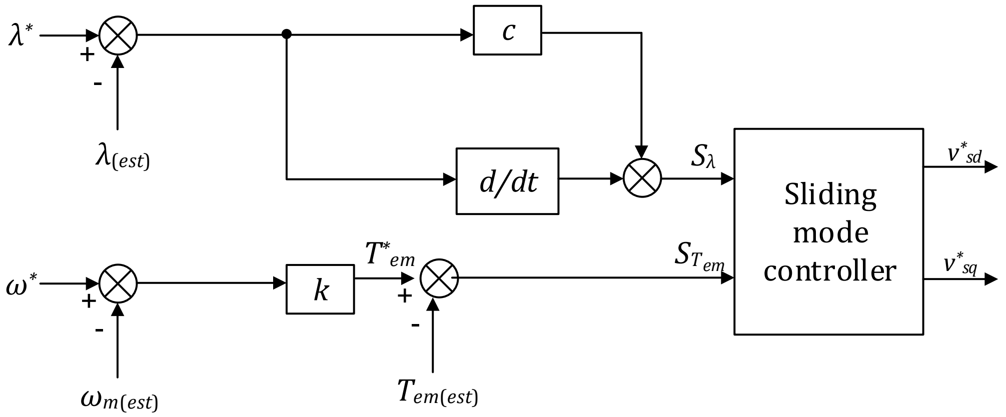

Figure 5.2 Structure of sliding mode DTC (without switching table)

Let $S_{T_{em},\lambda} = [s_{T_{em}} \quad s_{\lambda}]^T$ be the vector that contains sliding surface of torque and flux [55]:

$$\begin{cases} s_{T_{em}} = T_{em} - T_{em}^* \\ s_{\lambda} = (\|\lambda\| - \lambda^*)c + (\|\dot{\lambda}\| - \dot{\lambda}^*) \end{cases} \tag{5.16}$$

where $\|\lambda\| = \sqrt{\lambda_\alpha^2 + \lambda_\beta^2}$, $\|\dot{\lambda}\|$ denotes $d\|\lambda\|/dt$, c is a designated positive constant and T_{em}^*, λ^* are the reference values of motor torque and rotor flux respectively.

If $s_{T_{em}} = 0$, then $T_{em} = T_{em}^*$ and if $s_{\lambda} = 0$, then $\lambda \rightarrow \lambda^*$ at the rate defined by c. Time derivatives of $s_{T_{em}}$ and s_{λ} can be obtained by substituting the IM model equations developed in Chapter 3 and recalled here for purpose of convenience.

$$\begin{aligned} &\frac{di_\alpha}{dt} = \beta\eta\lambda_\alpha + \beta\omega_e\lambda_\beta - \gamma i_\alpha + \frac{1}{\sigma L_s} v_\alpha, \\ &\frac{di_\beta}{dt} = \beta\eta\lambda_\beta - \beta\omega_e\lambda_\alpha - \gamma i_\beta + \frac{1}{\sigma L_s} v_\beta, \\ &\frac{d\lambda_\alpha}{dt} = -\eta\lambda_\alpha - \omega_e\lambda_\beta + \eta L_m i_\alpha, \\ &\frac{d\lambda_\beta}{dt} = -\eta\lambda_\beta + \omega_e\lambda_\alpha + \eta L_m i_\beta, \\ &T = \frac{3P}{2}\frac{L_m}{L_r}\left(i_\beta\lambda_\alpha - i_\alpha\lambda_\beta\right), \\ &\frac{d\omega_r}{dt} = \frac{1}{J}(T - T_l), \end{aligned} \tag{5.17}$$

After substitution, for $s_{T_{em}}$ we have

$$\begin{aligned} \dot{s}_{T_{em}} &= \dot{T}_{em} - \dot{T}_{em}^* \\ &= \frac{3pL_m}{2L_r}\left(\dot{i_\beta}\lambda_\alpha + i_\beta\dot{\lambda}_\alpha - \dot{i_\alpha}\lambda_\beta - i_\alpha\dot{\lambda}_\beta\right) - \dot{T}_{em}^* \\ &= f_1\left(i_\alpha, i_\beta, \lambda_\alpha, \lambda_\beta, \omega_e, \dot{T}_{em}^*\right) + \frac{3pL_m}{2\sigma L_r L_s}\left(v_\beta\lambda_\alpha - v_\alpha, \lambda_\beta\right) \end{aligned} \tag{5.18}$$

and for s_{λ}

$$\begin{aligned} \dot{s}_{\lambda} &= (\|\dot{\lambda}\| - \dot{\lambda}^*)C + (\|\ddot{\lambda}\| - \ddot{\lambda}^*) \\ &= f_2\left(i_\alpha, i_\beta, \lambda_\alpha, \lambda_\beta, \omega_e, \dot{\lambda}^*, \ddot{\lambda}^*\right) + \frac{1}{\sqrt{\lambda_\alpha^2 + \lambda_\beta^2}}\left(v_\alpha\lambda_\alpha - v_\beta, \lambda_\beta\right) \end{aligned} \tag{5.19}$$

Where f_1 and f_2 are continuous non-linear functions of all arguments (note they're not functions of v_α and v_β) and $\|\ddot{\lambda}\|$ denotes $d^2\|\lambda\|/dt^2$.

Vector $\dot{S}_{T_{em},\lambda}$ can be expressed in matrix form as:

$$\dot{S}_{T_{em},\lambda} = \begin{bmatrix} \dot{s}_{T_{em}} \\ \dot{s}_{\lambda} \end{bmatrix} = F + C_1 \begin{bmatrix} -\lambda_\beta & \lambda_\alpha \\ \frac{\lambda_\alpha}{\sqrt{\lambda_\alpha^2+\lambda_\beta^2}} & \frac{\lambda_\beta}{\sqrt{\lambda_\alpha^2+\lambda_\beta^2}} \end{bmatrix} \begin{bmatrix} v_\alpha \\ v_\beta \end{bmatrix} \tag{5.20}$$

where:

$F = [f_1 \quad f_2]^T$, C_1 is a diagonal matrix with elements $C_1^{11} = 3pL_m/(\sigma L_r L_s)$ and $C_1^{22} = 1$.

Stator voltages v_α and v_β can be handled as control inputs of the IM system, but they cannot be implemented directly since only the switching elements of the inverter (they receive PWM signals in conventional motor control techniques) can be controlled. Thus, the control inputs should be formulated in terms of phase voltages as well as of gating signals of the inverter. As follows from Equation (3.64) in Chapter 3, the relation between v_α, v_β and phase voltages is

$$\begin{bmatrix} v_\alpha \\ v_\beta \end{bmatrix} = \frac{2}{3} \begin{bmatrix} 1 & -\frac{1}{2} & -\frac{1}{2} \\ 0 & \frac{\sqrt{3}}{2} & -\frac{\sqrt{3}}{2} \end{bmatrix} \begin{bmatrix} v_a \\ v_b \\ v_c \end{bmatrix} \tag{5.21}$$

where the phase voltages v_a, v_b, v_c are the potential differences between points *a*, *b*, *c* and neutral point *n* respectively, as defined by Figure 3.7 (in Chapter 3).

From Equation (5.20) and (5.21)

$$\dot{S}_{T_{em},\lambda} = \begin{bmatrix} \dot{s}_{T_{em}} \\ \dot{s}_{\lambda} \end{bmatrix} = F + C_1 \begin{bmatrix} -\lambda_\beta & \lambda_\alpha \\ \frac{\lambda_\alpha}{\sqrt{\lambda_\alpha^2+\lambda_\beta^2}} & \frac{\lambda_\beta}{\sqrt{\lambda_\alpha^2+\lambda_\beta^2}} \end{bmatrix} \begin{bmatrix} v_\alpha \\ v_\beta \end{bmatrix}$$

$$= F + \frac{2}{3} C_1 \begin{bmatrix} -\lambda_\beta & \lambda_\alpha \\ \frac{\lambda_\alpha}{\sqrt{\lambda_\alpha^2+\lambda_\beta^2}} & \frac{\lambda_\beta}{\sqrt{\lambda_\alpha^2+\lambda_\beta^2}} \end{bmatrix} \begin{bmatrix} 1 & -\frac{1}{2} & -\frac{1}{2} \\ 0 & \frac{\sqrt{3}}{2} & -\frac{\sqrt{3}}{2} \end{bmatrix} \begin{bmatrix} v_a \\ v_b \\ v_c \end{bmatrix}$$

$$= F + \frac{2}{3} C_1 \begin{bmatrix} -\lambda_\beta & \left(\frac{\lambda_\beta+\sqrt{3}\lambda_\alpha}{2}\right) & \left(\frac{\lambda_\beta-\sqrt{3}\lambda_\alpha}{2}\right) \\ \frac{\lambda_\alpha}{\sqrt{\lambda_\alpha^2+\lambda_\beta^2}} & \frac{-\lambda_\alpha+\sqrt{3}\lambda_\beta}{2\sqrt{\lambda_\alpha^2+\lambda_\beta^2}} & \frac{-\lambda_\alpha-\sqrt{3}\lambda_\beta}{2\sqrt{\lambda_\alpha^2+\lambda_\beta^2}} \end{bmatrix} \begin{bmatrix} v_a \\ v_b \\ v_c \end{bmatrix}$$

$$= F + \frac{2}{3} \begin{bmatrix} Q_1 \\ Q_2 \end{bmatrix} \tag{5.22}$$

where $[Q_1 \quad Q_2]^T$ is a vector that represents the product of 2×2 matrix C_1, the 2×3 matrix (depending on flux components) and the 3×1 vector in the penultimate step in Equation (5.22).

5.3.1 Control Law Design by Ljapunov Method

Now consider the Ljapunov function candidate

$$V = \frac{1}{2} S_{T_{em},\lambda}^{T} S_{T_{em},\lambda} \tag{5.23}$$

Its derivative is

$$\begin{aligned} \dot{V} &= S_{T_{em},\lambda}^{T} \dot{S}_{T_{em},\lambda} \\ &= F + \frac{2}{3}\left(s_{T_{em}} Q_1 + s_\lambda Q_2\right) \\ &= F + \frac{2}{3}[\Omega_1 \quad \Omega_2 \quad \Omega_3]\begin{bmatrix} v_a \\ v_b \\ v_c \end{bmatrix} \end{aligned} \tag{5.24}$$

where:

$$\left| \begin{aligned} \Omega_1 = &\quad -C_1^{11}\lambda_\beta s_{T_{em}} + \frac{\lambda_\alpha}{\sqrt{\lambda_\alpha^2+\lambda_\beta^2}} s_\lambda \\ \Omega_2 = &\quad C_1^{11}\left(\frac{\lambda_\beta+\sqrt{3}\lambda_\alpha}{2}\right) s_{T_{em}} + \frac{-\lambda_\alpha+\sqrt{3}\lambda_\beta}{2\sqrt{\lambda_\alpha^2+\lambda_\beta^2}} s_\lambda \\ \Omega_2 = &\quad C_1^{11}\left(\frac{\lambda_\beta-\sqrt{3}\lambda_\alpha}{2}\right) s_{T_{em}} + \frac{-\lambda_\alpha-\sqrt{3}\lambda_\beta}{2\sqrt{\lambda_\alpha^2+\lambda_\beta^2}} s_\lambda \end{aligned} \right. \tag{5.25}$$

From Equations (3.40) and 3.41) in Chapter 3, we have

$$\begin{bmatrix} v_a \\ v_b \\ v_c \end{bmatrix} = \frac{1}{3}\begin{bmatrix} 2 & -1 & -1 \\ -1 & 2 & -1 \\ -1 & -1 & 2 \end{bmatrix}\begin{bmatrix} u_1 \\ u_2 \\ u_3 \end{bmatrix} \tag{5.26}$$

The control variables u_1, u_2, u_3, take values from the discrete set $\{-u_0 \quad u_0\}$ with u_0 being the DC-bus voltage (as showed in Figure3.7).

Substituting (5.26) into (5.24) and denoting

$$[\Lambda_1 \quad \Lambda_2 \quad \Lambda_3] = [\Omega_1 \quad \Omega_2 \quad \Omega_3]\begin{bmatrix} 2 & -1 & -1 \\ -1 & 2 & -1 \\ -1 & -1 & 2 \end{bmatrix}, \tag{5.27}$$

we have that

$$[\Lambda_1 \quad \Lambda_2 \quad \Lambda_3] = [2\Omega_1 - \Omega_2 - \Omega_3 \quad -\Omega_1 + 2\Omega_2 - \Omega_3 \quad -\Omega_1 - \Omega_2 + 2\Omega_3] \tag{5.28}$$

then $\dot{V}$ is of the form

$$\dot{V} = F + \frac{2}{9}\begin{bmatrix}\Lambda_1 & \Lambda_2 & \Lambda_3\end{bmatrix}\begin{bmatrix}u_1\\ u_2\\ u_3\end{bmatrix} \tag{5.29}$$

further simplified as

$$\dot{V} = F + \frac{2}{9}(\Lambda_1 u_1 + \Lambda_2 u_2 + \Lambda_3 u_3) \tag{5.30}$$

Defining the control logic signals as $g_1 = u_1/u_0$, $g_2 = u_2/u_0$, $g_3 = u_3/u_0$ which takes values from the discrete set $\{-1 \quad 1\}$, $\dot{V}$ becomes

$$\dot{V} = F + \frac{2}{9}[\Lambda_1 g_1 u_0 + \Lambda_2 g_2 u_0 + \Lambda_3 g_3 u_0] \tag{5.31}$$

which can be further expressed as

$$\dot{V} = f_v + \frac{2}{9}u_0[(\Lambda_1)g_1 + (\Lambda_2)g_2 + (\Lambda_3)g_3] \tag{5.32}$$

Select control logic of inverter as

$$\begin{cases} g_1 = & -sign(\Lambda_1)\\ g_2 = & -sign(\Lambda_2)\\ g_3 = & -sign(\Lambda_3)\end{cases} \tag{5.33}$$

resulting in

$$\dot{V} = f_v + \frac{2}{9}u_0[|\Lambda_1| + |\Lambda_2| + |\Lambda_3|] \tag{5.34}$$

When the DC-bus voltage $u_0 > 0$ has enough magnitude, $\dot{V} < 0$ can be guaranteed. Implying that $s_{T_{em}} = 0$, $s_\lambda = 0$ in finite time. This also means that the real torque is equal to the reference torque ($T_{em} = T_{em}^*$) and $||\lambda||$ tends to λ^* at the desired rate C.

Finally the On-Off signal which takes value from the discrete set {0, 1}, (with 0 = Off and 1 = On) can be generated based on Equation (3.58) in Chapter 3.

$$\begin{aligned} s_{w1} &= 0.5(1 + g_1),\ \ s_{w4} = 1 - s_{w1}\\ s_{w2} &= 0.5(1 + g_2),\ \ s_{w5} = 1 - s_{w2}\\ s_{w3} &= 0.5(1 + g_3),\ \ s_{w6} = 1 - s_{w3}\end{aligned} \tag{5.35}$$

The encoder-less DTC MATLAB® model is shown in Figure 5.3 and the associated code for execution of parameters and initial values is provided in Appendix C. Results of the model are discussed in Chapter 6.

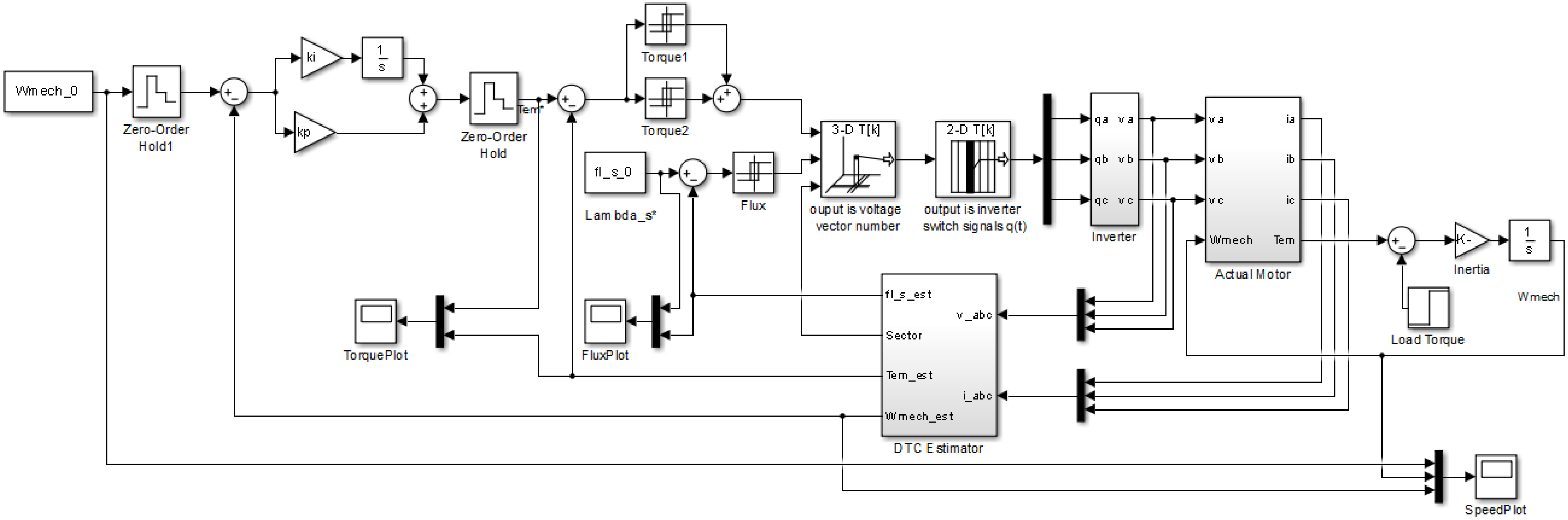

Figure 5.3 Encoderless DTC with SVM MATLAB® model

Chapter 6

6 Results and Discussion

6.1 V/f Experimental Results

Signal generated in the laboratory for the v/f control are presented in this section. Initially, the SPWM was designed using analog and logic circuits, the circuit and signals obtained have been discussed in SPWM section of Chapter 4. The six-step wave was generated and applied in the eventual design and implementation of the v/f drive discussed in Chapter 4. Results for the step-wave operation include the phase and line voltages obtained at the output of the three-phase inverter and the v/f graphical output from the control logic circuit.

6.1.1 Six-step Output Voltage

Figure 6.1 shows the output voltage waveforms for the six-step operation of the voltage-fed three-phase inverter. Figure 6.1a shows the line voltage output while (b) shows the phase voltage waveform. This waveforms match the MATLAB® simulated output, hence the results are satisfactory.

The logic circuit controls the ratio of voltage to frequency. The circuit was tested at different step voltages (2 units/step) to check the resulting change in frequency. The graph of voltage per frequency is plotted in Figure 6.2. The solid line shows the measured voltage-to-frequency obtained from the laboratory implementation while the dashed line shows the desired linear voltage-to-frequency ratio plot.

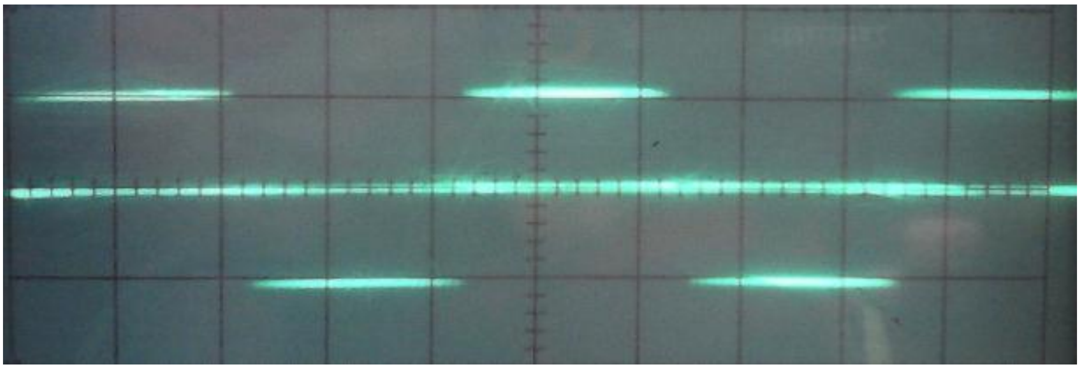

(a) Line voltage waveform

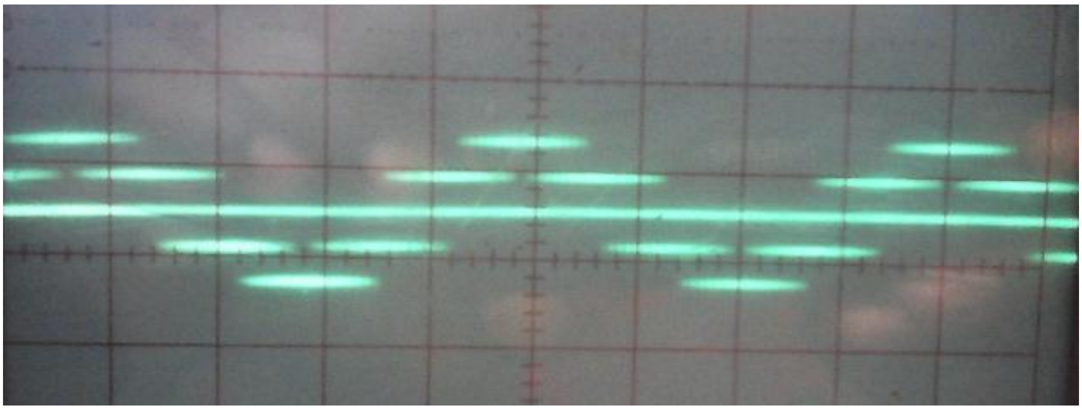

(b) phase voltage waveform

Figure 6.1 Output voltage waveforms for the six-step operated voltage-fed inverter

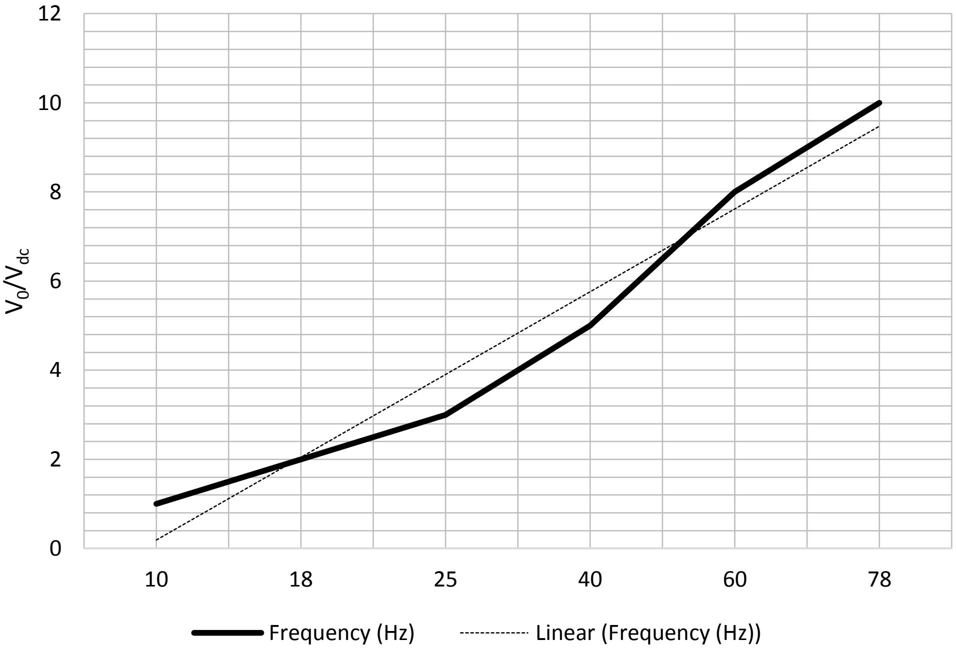

Figure 6.2 Graph of voltage (p.u.) against frequency of the control logic circuit

6.1.2 V/f MATLAB® Results

Simulation results for the constant volts/hertz model simulated in the MATLAB® environment is shown in Figure 6.3. Graphs showing the stator current, rotor speed, electromagnetic torque and dc bus voltage is shown.

Step torque are applied at 0, 2, 3 and 4 seconds with values 0, –11, 11 and back to 0. The behaviour of the stator current and dc-bus voltage to the torque changes is demonstrated in the figure. For the rotor speed graph, the dotted line shows the reference rotor speed while the solid line shows the actual rotor speed. At different values of impressed torque, the speed changes, but as observed from the graph the rotor speed in relation with the reference speed is not very large. This is a limitation of the open-loop v/f method. Its response to variable load torques are slow and not very precise. For the direct torque control, it will be seen that the rotor speed eventually matches with its reference speed, this is investigated in the next section

6.2 Direct Torque Control Simulation Results

The SM-DTC scheme was modelled, initially operating in steady state. At time t = 0.4 s, a load torque disturbance causes it to reduce to one-half of its initial value, the objective is to keep the load speed constant at its initial value. The maximum simulation time t_{max} = 1.0s, DC bus voltage of the inverter V_d is 600V, switching frequency is 10 kHz.

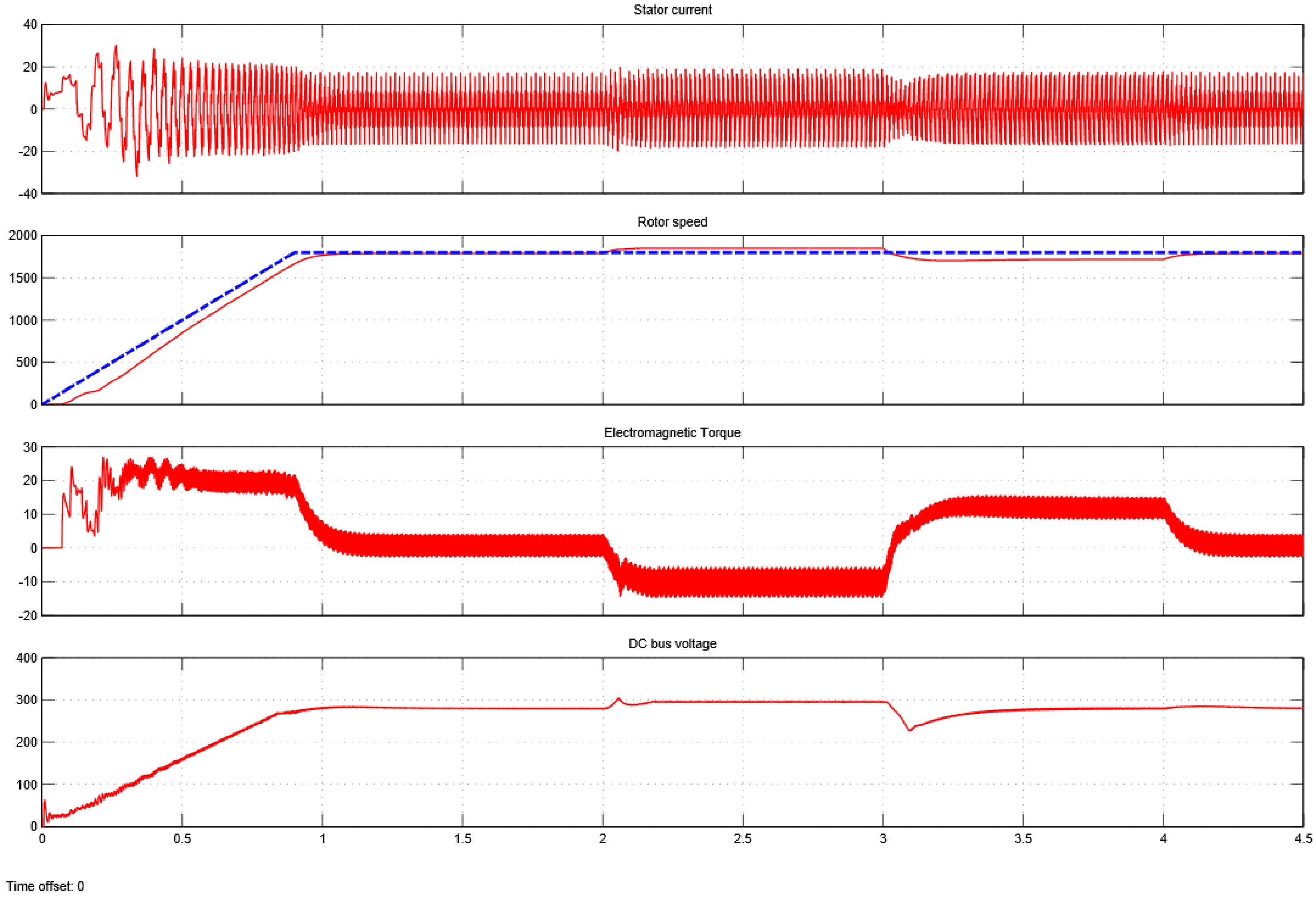

Figure 6.3 Simulation results showing stator current, rotor speed, electromagnetic torque and dc-bus voltage

Figure 6.4 shows the torque results of the MATLAB® simulation. At 0.4*s* a load disturbance torque is applied on the system. The torque graph shows that our estimated torque matches significantly with the reference torque. Corresponding effect on the speed is shown in Figure 6.5. It is observed that the speed increases momentarily with impression of decreased load which agrees with the dynamic behaviour of an induction motor.

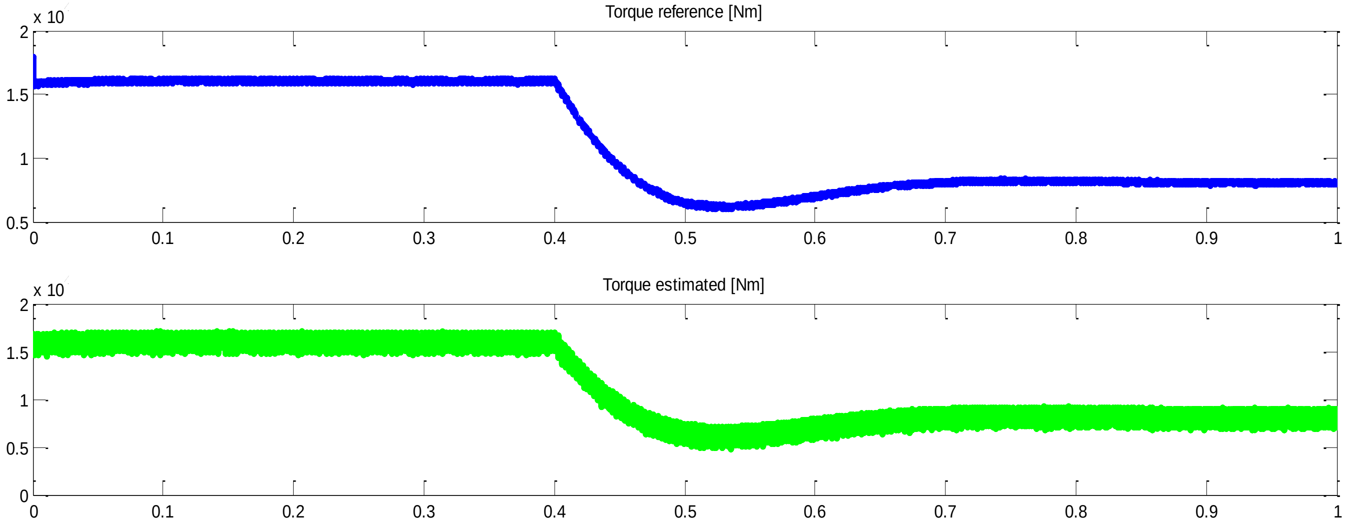

Figure 6.4 Torque waveforms (estimated and reference) for DTC

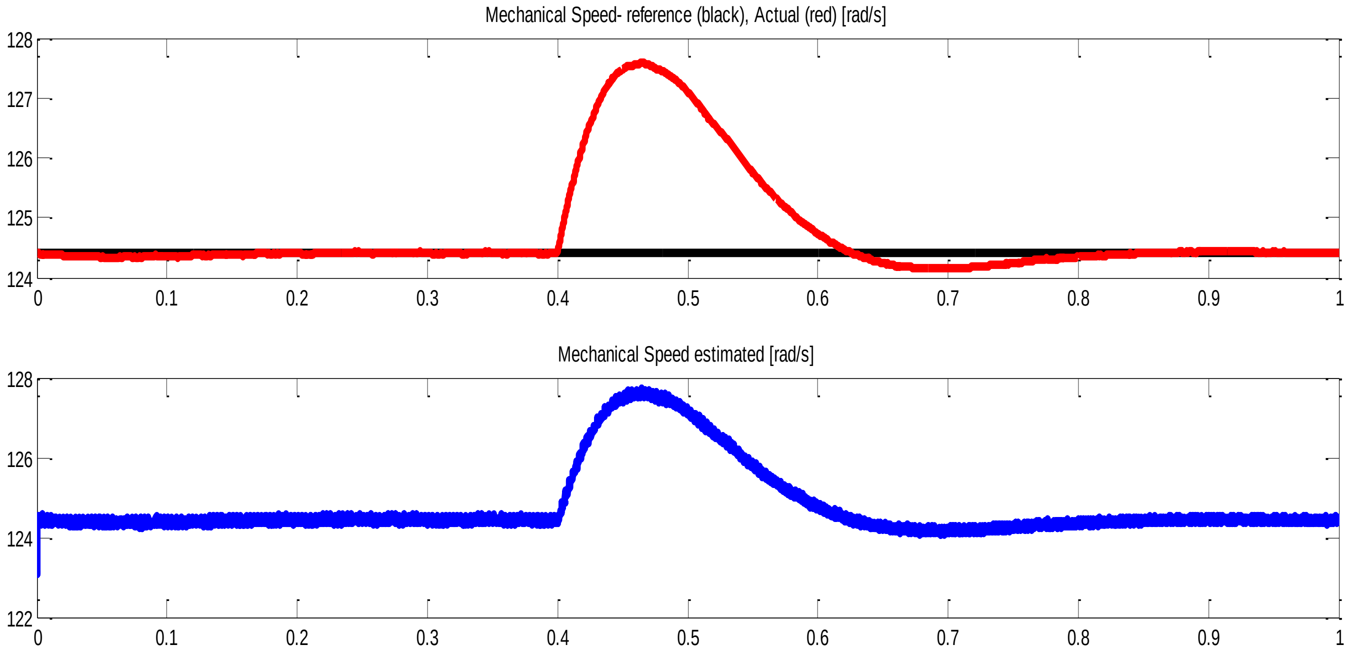

Figure 6.5 Speed waveforms for DTC

Figure 6.5 shows that our objective of constant load speed is accomplished, the black line is the reference speed, i.e. desired speed. The red line is the actual speed. In 0.4s, after the impressed load torque, the drive control system was able to come back to the desired speed. This highlights the advantage the DTC technique has over the v/f control technique. Recall, the drive is sensorless and both torque and speed had to be estimated, the graph shows the estimated mechanical speed is similar to the actual speed.

The stator flux, reference and estimated, is represented in Figure 6.6 for completion. Recall the calculations done for flux estimation, the scope waveform shown below shows the level of accuracy of the estimation. The reference is between the values 2.22 and 2.23*webers* while the estimated fluctuates between 2.2 and 2.5*webers*.

These waveform outputs proves the validity of encoder-less DTC with torque and rotor flux control.

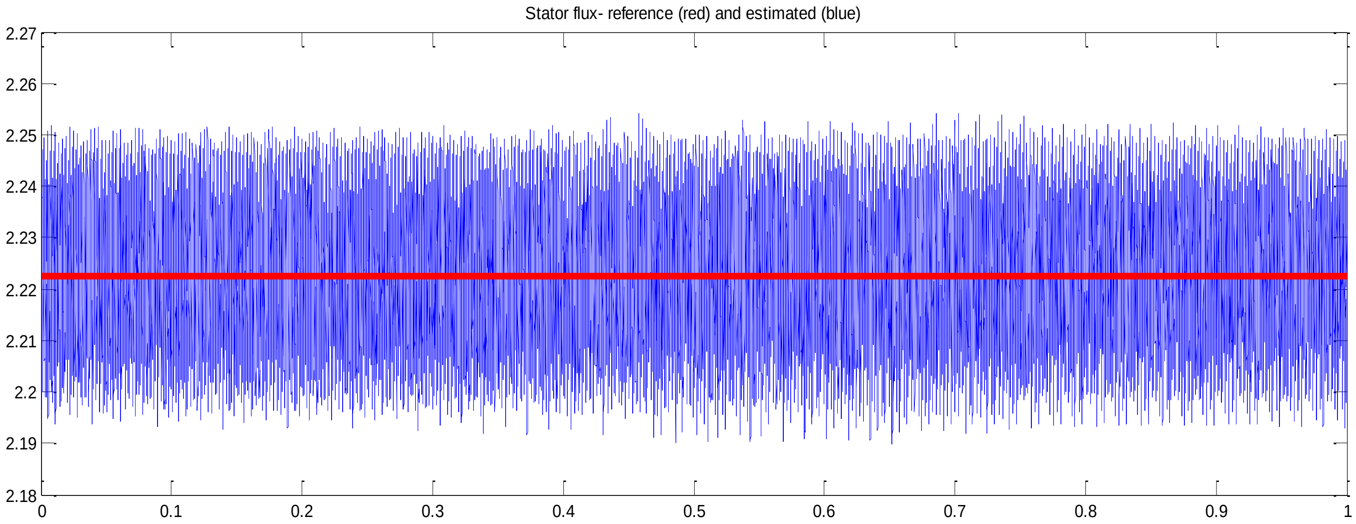

Figure 6.6 Waveform showing estimated and reference flux in the DTC scheme

Chapter 7

7 Conclusion and Recommendations

7.1 Conclusion

The two techniques employed in this research work are the constant volts/hertz control and the direct torque control using the sliding mode approach. Depending on the purpose and application of the drive, both techniques are able to achieve speed control.

The V/f control is one of the most popular control techniques and possessing a simple algorithm with no dependence on sensors and no requirement of speed measurement (as it can operate in open-loop). It is a much simpler control strategy than the DTC control and does not require high performance digital processing. The V/f drive response to torque is poor compared to the DTC drive but can be employed efficiently where precise speed control is not critical.

Speed and torque control of induction motor is usually attained by application of speed or position sensors, and its implementation is straightforward. However, the use of these encoders require the additional mounting space, reduction in reliability of the system in harsh environments [79] (such as vibrations from the EV) and also increase in the cost of motor drive. Furthermore, the encoders used for position and speed measurement may lead to problems. Faults such as loss of output information, offset, disturbances, measurement deviation [80], and so on, may occur. On the other hand, encoderless DTC control of induction motor drives estimates position using an observer and eliminates the need for the speed sensor. It reduces hardware complexity, size, maintenance and ultimately cost. It also eliminates direct sensor wiring and has been shown to have better noise immunity [81] and increased reliability.

The objective of the DTC is to maintain the motor torque and stator flux within a defined band of tolerance, hence it requires an accurate knowledge of the magnitude and angular position of the controlled flux. But its greatest drawback is the sensitivity to uncertainties in the motor parameters. The speed estimation is affected by parameter variations especially the stator resistance due to temperature rises, particularly at low speeds which may cause significant performance degradation and even instability of the system.

The sliding mode approach to the drive design is to ensure the stability and high performance levels in spite of the disturbances and mismatches. The sliding mode controller is designed to drive, force and confine the system state to lie within a very small neighbourhood of the switching function despite the disturbances and perturbations in harsh EV environments, and variations in IM parameters. The ease of implementation and relatively short computation required in the implementation of SMC in microcontrollers is an advantage of this technique.

The result of this study is an SM-DTC controller design which eliminates some limitations of the two individual controls and retains their merits. The performances of SM-DTC IM drive even in the presence of parameters uncertainties and mismatching disturbances has been presented. The drive delivers high performance and quicker response and can be applied in EV with satisfactory performance.

7.2 Recommendations

Modifications and improvement can be made in the control scheme such as an improved filter and observer design of the sliding mode controller also the design of an adaptive algorithm for increased robustness and reduced sensitivity to disturbances. The SM-DTC concept discussed so far remains theoretical until it is implemented, thus implementation is recommended and is possible with the use of microprocessors for computations.

References

[1] S. Dewan, G. Slemon and A. Straughen, Power Semiconductor Drives, Toronto, Ontario: John Wiley & Sons, 1984.

[2] S. Reddy, Fundamentals of Power Electronics, Harrow, UK: Alpha Science International Ltd, 2007.

[3] S. Leitman and B. Brant, Build Your Own Electric Vehicle, 2nd ed., The McGraw-Hill Companies, Inc.: New York, 2009.

[4] T. Uzuka, "Faster than a Speeding Bullet. An Overview of Japanese high-speed rail technology and electrification," *IEEE Electrification. Sparking Innovation.,* vol. 1, no. 1, pp. 11-20, 1 September 2013.

[5] J. Larminie and J. Lowry, Electric Vehicle Technology Explained, 2nd ed., Wes Sussex,UK: John Wiley & Sons, Ltd., 2012.

[6] M. Ehsani, Y. Gao and A. Emadi, Modern Electric, Hybrid Electric, and Fuel Cell Vehicles. Fundamentals, Theory and Design, 2nd ed., FLorida: CRC Press, 2010.

[7] C. Chan and K. Chau, Modern Electric Vehicle Technology, New York: Oxford University Press, 2001.

[8] M. Westbrook, The Electric car. Development and future of battery, hybrid and fuel-cell cars, London & Warrendale: The Institute of Electrical Engineers (IEE), London, UK and Society of Automotive Engineers, Warrendale, PA., 2001.

[9] I. Husain, Electric and hybrid vehicles: Design Fundamentals, Florida: CRC Press, Francis & Tayor Group, LLC, 2005.

[10] J. Estima and A. Cardoso, "Efficiency Analysis of Drive Train Topologies Applied to Electric/Hybrid Vehicles," *IEEE Transactions on Vehicular Technology,* vol. 61, no. 3, pp. 1021-1031, 2012.

[11] X. Xue, K. Cheng and N. Cheung, "Selection of Electric Motor Drives for Electric Vehicles," in *Power Engineering Conference, AUPEC '08. Australasian Universities*, Sydney, NSW, 2008.

[12] H. Toliyat and G. Kliman, Handbook of Electric Motors, 2nd, Revised and Expanded ed., Florida: CRC Press, 2004.

[13] N. Kar, K. Iyer, A. Labak, X. Lu, C. Lai, A. Balamurali, B. Esteban and M. Sid-Ahmed, "Courting and Sparking," *IEEE Electrification: Sparking Innovation,* vol. 1, no. 1, pp. 21-31, 1 September 2013.

[14] A. Hughes, Electric Motors and Drives: Fundamentals, Types and Applications, 3rd ed., Burlington, MA: Elsevier, 2006.

[15] D. Hanselman, Brushless Permanent-Magnet Motor Design, New York: McGraw-Hill, 1994.

[16] B. Bose, Modern Power Electronics and AC Drives, New Jersey: Prentice Hall, 2002.

[17] A. Trzynadlowski, Control of Induction Motors, California: Academic Press, 2001.

[18] B. Akin and N. Garg, “Scalar (V/f) Control of 3-Phase Induction Motors,” Texas Instruments Incorporated, Texas, 2013.

[19] K. Jezernik and G. Edelbaher, “Sensorless Torque VSS Control of EV,” in *The 29th Annual Conference of the IEEE Industrial Electronics Society, 2003. IECON '03.*, Roanoke, VA, USA, 2003.

[20] C. Lascu, I. Boldea and F. Blaabjerg, “A Class of Speed-Sensorless Sliding-Mode Observers for High-Performance Induction Motor Drives,” *IEEE Transactions on Industrial Electronics,* vol. 56, no. 9, pp. 3394-3403, September 2009.

[21] M. Guerreiro and F. Silva, “Rotor Position Control for Induction Machines using Diametrical Inversion of Stator Voltage,” *IEE Proc. Electr. Power Appl.,* vol. 147, no. 2, pp. 99-106, 2000.

[22] W. Rippel, “Blog: Induction versus DC Brushless Motors,” 9 January 2007. [Online]. Available: http://www.teslamotors.com/blog/induction-versus-dc-brushless-motors. [Accessed 24 March 2015].

[23] M. Ehsani, “Phase and Amplitude Modulation Techniques for Rotor Position Sensing in Switched Reluctance Motors”. United States of America Patent 5,291,115, 1994.

[24] J. Kokernak, D. Torrey and M. Kaplan, “A switched reluctance starter/alternator for hybrid electric vehicles,” in *Proceedings of the PCIM '99*, Nürnberg, 1999.

[25] J. Lyons, S. MacMinn and M. Preston, “Discrete position estimator for switched reluctance machine using a flux-current map comparator”. United States of America Patent 5140243, 1991.

[26] G. Suresh, B. Fahimi, K. Rahman and M. Ehsani, “Inductance based position encoding for sensorless SRM drives,” in *Proceedings of the 1999 IEEE Power Electronics Specialists Conference*, 1999.

[27] M. Ehsani, “Position Sensor Elmination Technique for the Switched Reluctance Motor Drive”. U.S. Patent 5072166, 1990.

[28] G. Dunlop and J. Marvelly, “Evaluation of a self commutated switched reluctance motor,” in *Proceedings of the 1987 Electric Energy Conference*, Adelaide, 1987.

[29] A. Lumsdaine and J. Lang, “State Observer for Variable Reluctance Motor,” *IEEE Transactions on Industrial Electronics,* vol. 37, no. 2, pp. 133-142, 1990.

[30] K. Rajashekara, “Present Status and Future Trends in Electric Vehicle Propulsion Technologies,” *IEEE Journal of Emerging and Selected Topics in Power Electronics,* vol. 1, no. 1, pp. 3-10, 2013.

[31] E. Schaltz, “Electrical Vehicle Design and Modeling,” in *Electric Vehicles - Modelling and Simulations*, 1 ed., S. Soylu, Ed., Croatia, INTECH, 2011, pp. 1-24.

[32] J. Wong, Theory of Ground Vehicles, New York: John WIley & Sons, 1978.

[33] D. Ronanki, A. Hemasundar and P. Parthiban, “A Small 4-wheeler EV Propulsion System Using DTC Controlled Induction Motor,” in *Proceedings of the World Congress on Engineering*, London, 2013.

[34] K. Jaber, A. Fakhfakh and R. Neji, "Modeling and Simulation of High Performance Electrical Vehicle Powertrains in VHDL-AMS.," in *Electric Vehicles - Modelling and Simulations*, S. Soylu, Ed., Croatia, INTECH, 2011, pp. 25-40.

[35] R. Udaykumar, V. Sundarsingh and M. Sharon, "Battery Operated Two Wheeler," in *Proceedings of International Conference on Power Electronic Drives and Energy Systems for Industrial Growth*, Perth, WA, Australia , 1998.

[36] K. Jezernik, A. Šabanović and M. Rodič, "Speed Sensorless Variable Structure Torque Control of Induction Motor," *AUTOMATIKA,* vol. 51, no. 1, pp. 33-40, 2010.

[37] K. Jezernik, "Speed Sensorless Torque Control of Induction Motor for EV's," [Online]. Available: http://www.ro.feri.uni-mb.si/projekti/pdf/EVS18.pdf. [Accessed 18 May 2015].

[38] K. Saito and I. Takahashi, "Application of Direct Torque Control Method to an Electric Vehicle," *Journal of Asian Electric Vehicles,* vol. 1, no. 2, pp. 437-442, 2003.

[39] O. Ellabban, J. Van Mierlo and P. Lataire, "A Comparative Study of Different Control Techniques for an Induction Motor Fed by a ZSource Inverter for Electric Vehicles," in *Proceedings of the 2011 International Conference on Power Engineering, Energy and Electrical Drives*, Torremolinos (Málaga), 2011.

[40] J. Guzinski and H. Abu-Rub, "Sensorless induction motor drive for electric vehicle application," *International Journal of Engineering, Science and Technology,* vol. 2, no. 10, pp. 20-34, 2010.

[41] E. Ejiogu and Y. Tanno, "A Simple 3-phase Reference Sinewave Generator Suitable for PWM AC Motor Drive.," in *Proceedings of the 31st SICE Annual Conference. International Session, Kumamoto University.*, Kumamoto, 1992.

[42] S. Srilad, S. Tunyasrirut and T. Suksri, "Implementation of a Scalar Controlled Induction Motor Drives," Busan, Korea, 2006.

[43] M. Khan, H. Al-Jenaid and M. Khan, "Duty cycle based volt/hertz inverter control for induction motor drives," in *Industry Applications Society Annual Meeting, 1994., Conference Record of the 1994 IEEE*, Denver, CO, 1994.

[44] K. Kumar and K. Satsangi, "Micro-Controller Based Closed Loop Control of Induction Motor Using V/F Method," in *IET-UK International Conference on Information and Communication Technology in Electrical Sciences (ICTES)*, Tamil Nadu, India, 2007.

[45] P. Vas, Sensorless Vector and Direct Torque Control, Oxford: Oxford University Press, 1998.

[46] N. Mohan, Advanced Electric Drives - Analysis, Control and Modeling using Simulink(R), Minneapolis: MNPERE, 2001.

[47] S.-K. Lin and C.-H. Fang, "Sliding-Mode Direct Torque Control of an Induction Motor," in *The 27th Annual Conference of the IEEE Industrial Electronics Society* , (IECON'01), 2001.

[48] E. Ejiogu and T. Kawabata, "Variable Structure System Control of Power Converters," *Power Electronics Society Journal,* vol. 20, no. 2, pp. 17-22, 1994.

[49] E. Ejiogu, “High Performance Vector Control of the Induction Motor by Application of the Variable Structure System Theory,” Department of System Development Engineering, Shinshu University, School of Graduate Studies, Nagano, 1994.

[50] S.-C. Tan, Y.-M. Yuk-Ming Lai and C. Tse, Sliding Mode Control of Switching Power Converters Techniques and Implementation, Boca Raton: CRC Press, 2012.

[51] W. Perruquetti and J. Barbot, Sliding Mode Control in Engineering., New York: Marcel Dekker Inc., 2002.

[52] V. Utkin, “Variable Structure Systems with Sliding Modes.,” *IEEE Transaction on Automatic Control,* vol. 22, no. 2, pp. 212-222, 1977.

[53] V. Utkin, Sliding Modes in Control and Optimization, London: Springer-verlag, 1992.

[54] W. Gao and J. Hung, “Variable Structure Control of non-linear System: A new approach,” *IEEE Transactions on Industrial Electronics,* p. 45, 1993.

[55] V. Utkin, J. Guldner and J. Shi, Sliding Mode Control in Electro-Mechanical Systems, 2nd ed., Florida: CRC Press, 2009.

[56] Q. Wu and C. and Shao, “ovel Hybrid Sliding-mode Controller for Direct Torque Control Induction Motor Drives,” in *Proceedings of the 2006 American Control Conference*, Minneapolis, 2006.

[57] M. Kazmierkowski, “Control of PWM Inverter-Fed Induction Motors,” in *Control in Power Electronics - Selected Problems*, M. Kazmierkowski, R. Krishnan and F. Blaabjerg, Eds., California, Academic Press, 2002, pp. 161-208.

[58] B. Bose, Power Electronics and AC Drives, New Jersey: Prentice-Hall, 1986.

[59] P. Horowitz and W. Hill, Art of Electronics, Cambridge: Cambridge University Press, 1989.

[60] V. Athani and S. Deshpande, “Microprocessor Control of a Three-Phase Inverter in Induction Motor Speed Control System,” *IEEE Transactions on Industrial Electronics and Control Instrumentation,* Vols. IECI-27, no. 4, pp. 291-298, 1980.

[61] M. Park and S. Sul, “Microprocessor-Based Optimal-Efficiency Drive of an Induction Motor,” *IEEE Transactions on Industrial Electronics,* Vols. IE-31, no. 1, pp. 69-73, 1984.

[62] A. Munoz-Garcia, T. Lipo and D. Novotny, “A new induction motor open-loop speed control capable of low frequency operation,” in *IEEE Industry Applications Society. Annual Meeting*, New Orleans, Louisiana, 1997.

[63] A. Gastli and N. Matsui, “V/F PWM Inverter with Motor Parameter Idnetification and Voltage Auto-Boost Capabilities,” in *Industrial Electronics Society. IECON '90., 16th Annual Conference of IEEE*, California, 1990.

[64] T. Ohnishi, H. Miyazaki and H. Okitsu, “High Efficiency Drive of an Induction Motor by Means of V/F Ratio Control,” in *IECON*, Tokushima, 1988.

[65] R. Echavarria, S. Horta and M. Oliver, “A Three Phase Motor Drive Using IGBT's and Constant V/F Speed Control with Slip Regulation,” in *CIEP IEEE*, San Luis Potosi, Mexico, 1995.

[66] J. Itoh, T. Hoshino and T. Kaneko, "A Performance Improvement of V/F Control using a Disturbance Observer," in *EPE-PEMC*, Portoroz, 2006.

[67] D. Lee and Y. Kim, "Control of Single-Phase-to-Three-Phase AC/DC/AC/ PWM Converters for Induction Motor Drives," *IEEE Transactions on Industrial Electronics,* vol. 54, no. 2, pp. 797-804, 2007.

[68] J. Slicker, "A PWM Transistor Inverter for an AC Electric Vehicle," IEEE Industrial Applications Society, Annual Meeting, 1991.

[69] D. Hart, Power Electronics, New York: McGraw-Hill, 2010.

[70] M. Kazimierczuk, Pulse-width Modulated DC–DC Power Converters, West Sussex: John Wiley & Sons, Ltd, 2008.

[71] D. Terrel, OP AMPS: Design, Application and Troubleshooting, 2nd ed., USA: Elsevier Science, 1996, p. 488.

[72] STMicroelectronics, "HCF4017B - DECADE COUNTER WITH 10 DECODED OUTPUTS," 2001. [Online]. Available: http://pdf.datasheetcatalog.com/datasheet/stmicroelectronics/2029.pdf. [Accessed 28 October 2014].

[73] G. Rizzoni, Principles and Applications of Electrical Engineering, 4th ed., New York: McGraw Hill, 2003.

[74] R. Boylestad and L. Nashelsky, Electronic Devices and Circuit Theory, New Delhi: Prentice-Hall of India Private Limited, 2006.

[75] R. Tocci and N. M. G. Widmer, Digital Systems: Principles and Application, 9th ed., Delhi: Dorling Kindersley (India) Pvt. Ltd., 2007.

[76] J. Bignell and R. Donovan, Digital Electronics, NY: Thomson Delmar Learning, 2007.

[77] STMicroelectronics, "HCC/HCF4027B - DUAL-J-K MASTER-SLAVE FLIP-FLOP," SGS-THOMSON Microelectonics., USA, 1994.

[78] M. Dal, "Sensorless Sliding Mode Direct Torque Control (DTC) of Induction Motor," in *IEEE ISIE 2005*, Dubrovnik, Croatia, 2005.

[79] B. Salmani, F. L. Pour and M. B. B. Sharifian, ". (2014). Comparison between the Vector Control Based on Anti-saturation Capability with the Sensorless Vector Control in PMSM," *American Journal of Electrical and Electronic Engineering,* vol. 2, no. 1, pp. 11-16, 2014.

[80] K. Gaeid, H. Ping, M. Khalid and A. Masaoud, "Sensor and Sensorless Fault Tolerant Control for Induction Motors Using a Wavelet Index," *Sensors,* vol. 12, no. 4, pp. 4031-4050, 2012.

[81] M. S. Zaky, "Stability Analysis of Speed and Stator Resistance Estimators for Sensorless Induction Motor Drives," *IEEE Transactions on Industrial Electronics,* vol. 59, pp. 858-870, 2012.

Appendices

Appendix A: MATLAB® Code for modelling EV Acceleration and distance covered

```
% PROJECT ELECTRIC VEHICLE ACCELERATION
t=linspace(0,50,501); % 0 to 15sec, in 0.1s steps
vel=zeros(1,501); % 501 readings of velocity
d=zeros(1,501);% array for storing distance travelled
dT=0.1;% 0.1sec time step
%THERE ARE THREE PHASES TO THE ACCELERATION
for n=1:500
    if vel(n)<10.5 % Torque constant till this point
        vel(n+1)=vel(n)+dT*(0.71-(0.000103*(vel(n)^2)));
    elseif vel(n)>16.7 % controller stops any more speed increase
        vel(n+1)=vel(n);
    else
      vel(n+1)=vel(n)+dT*((8.65/vel(n))-0.125-(0.000103*(vel(n)^2)));
    end;
    d(n+1)=d(n)+0.1*vel(n); % compute distance travelled.
end;
    vel=vel.*3.6; %multiply by 3.6 to convert m/s to kph
plot(t,vel);
xlabel('Time / seconds');
ylabel('distance / m');
title('Full power (WOT) acceleration of electric CAR');
```

To find the distance covered, change the plot line above to

```
plot(t,d);
```

Appendix B: MATLAB® Code for Execution of Torque vs Speed Characteristics of V/F Control in IM

Table B.1 Machine details used in MATLAB® codes execution for V/F control

RMS value of supply voltage (line-to-line)	415V
Number of poles	4
Stator resistance	0.075*ohms*
Rotor resistance	0.1*ohms*
Frequency	50 *Hz*
Stator leakage reactance at 50Hz	0.45 *ohms*
Rotor leakage reactance at 50Hz	0.45 *ohm*
V/F ratio	8.3

```
function out = inductionconstVf()
Vll=input('Suppy Voltage (line to line) RMS value @ 50 Hz: ');
f2=input('Enter the second frequency: ');
f3=input('Enter the third frequency: ');
f4=input('Enter the fourth frequency: ');
f5=input('Enter the fifth frequency: ');
P=input('Enter the number of poles: ');
Rs=input('Stator Resistance: ');
Rr=input('Rotor Resistance: ');
Xs=input('Stator Leakage Reactance @ 50 Hz frequecny: ');
Xr=input('Rotor Leakage Reactance @ 50 Hz frequecny: ');
Ls=Xs/(2*pi*50);
Lr=Xr/(2*pi*50);
```

```
Vlnf1=Vll/(3^0.5);
Vlnf2=Vlnf1*f2/50;
Vlnf3=Vlnf1*f3/50;
Vlnf4=Vlnf1*f4/50;
Vlnf5=Vlnf1*f5/50;
Wsync1=4*pi*50/P;
Wsync2=4*pi*f2/P;
Wsync3=4*pi*f3/P;
Wsync4=4*pi*f4/P;
Wsync5=4*pi*f5/P;
Tmf2=Wsync2*500+1;
Tmf3=Wsync3*500+1;
Tmf4=Wsync4*500+1;
Tmf5=Wsync5*500+1;
Tmf1=Wsync1*500+1;
m=1;
for Wrotor1=0:0.002:Wsync1
Tmf1(m)=(3*(((Vlnf1^2)*Rr/((Wsync1-Wrotor1)/Wsync1))/((Rs+Rr/((Wsync1-
Wrotor1)/Wsync1))^2+(2*pi*50*Ls+2*pi*50*Lr)^2))/Wsync1); %star connected
m=m+1;
end
m=1;
for Wrotor2=0:0.002:Wsync2
Tmf2(m)=(3*(((Vlnf2^2)*Rr/((Wsync2-Wrotor2)/Wsync2))/((Rs+Rr/((Wsync2-
Wrotor2)/Wsync2))^2+(2*pi*f2*Ls+2*pi*f2*Lr)^2))/Wsync2);
m=m+1;
end
m=1;
for Wrotor3=0:0.002:Wsync3
Tmf3(m)=(3*(((Vlnf3^2)*Rr/((Wsync3-Wrotor3)/Wsync3))/((Rs+Rr/((Wsync3-
Wrotor3)/Wsync3))^2+(2*pi*f3*Ls+2*pi*f3*Lr)^2))/Wsync3);
m=m+1;
end
m=1;
for Wrotor4=0:0.002:Wsync4
Tmf4(m)=(3*(((Vlnf4^2)*Rr/((Wsync4-Wrotor4)/Wsync4))/((Rs+Rr/((Wsync4-
Wrotor4)/Wsync4))^2+(2*pi*f4*Ls+2*pi*f4*Lr)^2))/Wsync4);
m=m+1;
end
m=1;
for Wrotor5=0:0.002:Wsync5
Tmf5(m)=(3*(((Vlnf5^2)*Rr/((Wsync5-Wrotor5)/Wsync5))/((Rs+Rr/((Wsync5-
Wrotor5)/Wsync5))^2+(2*pi*f5*Ls+2*pi*f5*Lr)^2))/Wsync5);
m=m+1;
end
plot(Tmf1);
hold on;
plot(Tmf2);
plot(Tmf3);
plot(Tmf4);
plot(Tmf5);
hold off;
ylabel('Torque(N-m)');
xlabel('Rotor Speed(Rad/s) * 100');
end
```

Appendix C: MATLAB® Code for Encoder-less DTC with SVM

C.1 Parameters and Initial Conditions

```
clear all
clc
% Example 8-1; File Name EX8_1calc.m
% Calculation of Initial Conditions
% Induction Motor Parameters
Rs=0.002;
Rr=0.0015;
Xls=0.05;
Xlr=0.047;
Xm=0.86;
Jeq=70;
p=6;
% Steady State Operating Condition
f=60; VLLrms= 690; s=0.01;  % phase-a voltage is at its positive peak at t=0
Wsyn=2*pi*60;                                           % synchronous speed in rad/s
Wd=Wsyn                                                 % speed of d-axis
WdA= s *Wsyn;                                           % slip speed
Wm=(1-s)*Wsyn;                                          % rotor speed in electrical
rad/s
% Phasor Calculations
Va = VLLrms * 2^0.5 / 3^0.5;                            % Va phasor
% Space Vectors at time t=0 with stator a-axis as the reference
Vs_0 = (3/2) * Va;                                      % Vs(0) space vector
Theta_Vs_0 = angle(Vs_0);                               % angle of Vs(0) space
vector
% We will assume that at t=0, d-axis is aligned to the stator a-axis.  Therefore,
Theta_da_0=0
Theta_da_0 = 0;
Vsd_0 = (2/3)^0.5 * abs(Vs_0) * cos(Theta_Vs_0 - Theta_da_0); % similar to Eq. 3-64
Vsq_0 = (2/3)^0.5 * abs(Vs_0) * sin(Theta_Vs_0 - Theta_da_0); % similar to Eq. 3-65
% Calculation of machine inductances
Ls = (Xls + Xm) / (2*pi*f);
Lm = Xm / (2*pi*f);
Lr = (Xlr + Xm) / (2*pi*f);
tau_r=Lr/Rr;
% Inductance matrix L in Eq. 3-62
L = [Ls Lm;...
     Lm Lr];
% Matrix A in Eq. 3-##
A = [Rs -Wd*Ls 0 -Wd*Lm;...
     Wd*Ls Rs Wd*Lm 0;...
     0 -WdA*Lm Rr -WdA*Lr;...
     WdA*Lm 0 WdA*Lr Rr];
Ainv = inv(A);
Vvector=[Vsd_0; Vsq_0; 0; 0];
Ivector=Ainv*Vvector;
Isd_0=Ivector(1)
Isq_0=Ivector(2)
Ird_0=Ivector(3)
Irq_0=Ivector(4)

% Electromagnetic Torque, which equals Load Torque in Initial Steady State
Tem_0 = (p/2) * Lm * (Isq_0 * Ird_0 - Isd_0 * Irq_0)    % Eq. 3-47
TL_0 = Tem_0

% Wmech = rotor speed in actual rad/s
Wmech_0=(2/p)*Wm      % Eq. 3-34

% Inductance matrix M in Eq. 3-61
M = [Ls 0  Lm 0 ;...
     0  Ls 0  Lm;...
     Lm 0  Lr 0 ;...
     0  Lm 0  Lr];
```

```
% dq winding Flux Linkages with the d-axis aligned with the stator a-axis
fl_dq_0 = M * [Isd_0; Isq_0; Ird_0; Irq_0];    % dq-winding fluxes in vector form,
Eq. 3-61
fl_sd_0 = fl_dq_0(1)
fl_sq_0 = fl_dq_0(2)
fl_rd_0 = fl_dq_0(3)
fl_rq_0 = fl_dq_0(4)
[thetar, fl_r_dq_0]=cart2pol(fl_rd_0, fl_rq_0)
[thetas, fl_s_dq_0]=cart2pol(fl_sd_0, fl_sq_0)
[theta_Is_dq, Is_dq_0]=cart2pol(Isd_0, Isq_0)
[theta_Vs_dq, Vs_dq_0]=cart2pol(Vsd_0, Vsq_0)

% d-axis is now aligned with the rotor flux which results in the following new
values:
fl_rq_0=0;              %fl_rq_0 equals zero
fl_rd_0=fl_r_dq_0
fl_sd_0_vs=fl_sd_0;
fl_sq_0_vs=fl_sq_0;
[fl_sd_0, fl_sq_0]=pol2cart(thetas-thetar, fl_s_dq_0)
[Isd_0, Isq_0]=pol2cart(theta_Is_dq-thetar, Is_dq_0)
[Vsd_0, Vsq_0]=pol2cart(theta_Vs_dq-thetar, Vs_dq_0)
fl_s_0=sqrt(3/2)*fl_s_dq_0;
sigma=1-(Lm*Lm)/(Ls*Lr);
Lsigma=sqrt(Ls*Lr-Lm*Lm);

Vd=1000
Vtri=5
fs=10e3

% Three level hysterisis control selection table
% The first index is the torque command :1->Decrease torque;2->Apply zero vecor;3-
>Increase torque
% The second index is the stator flux command: 1->Decrease flux;2->Increase flux
% The third index is the stator flux sector number 1-6

% The following is to Decrease Torque
U(1,:,:)=[  4   5   1   3   2   6   ;...
            5   1   3   2   6   4   ];

% The following is to Apply Zero Vector as determined by torque controller
(indepenent of flux controller)
U(2,:,:)=[  0   7   0   7   0   7   ;...
            7   0   7   0   7   0   ];
% The following is to Increase torque
U(3,:,:)=[  2   6   4   5   1   3   ;...
            3   2   6   4   5   1   ];

delta_Tem=0.05*Tem_0
delta_flux=0.005*fl_s_0
Tsample=25e-6
Tsample_speed=500e-6

% Based on the voltage vector number, inverter switch signals q(t) are selected for
phases a-b-c.
Q=[0    1   0   1   0   1   0   1;...
   0    0   1   1   0   0   1   1;...
   0    0   0   0   1   1   1   1];

% controller calculations for example 5_2
Wc=25; % crossover freq in rad/s
PM=60*pi/180; % phase margin in rad/s
Wc_kp_by_ki=tan(PM);
ki=Wc*Wc*Jeq/(sqrt(1+(tan(PM)^2)))
kp=ki*Wc_kp_by_ki/Wc
```

C.2 DTC MATLB® Plots

```
figure(1)
subplot(2,1,1);
plot(SD2(:,1),SD2(:,2)); % plotting of Torque
title('Torque reference [Nm]');
subplot(2,1,2);
plot(SD2(:,1),SD2(:,3),'g');
title('Torque estimated [Nm]');

figure(2)
subplot(2,1,1);
plot(SD1(:,1),SD1(:,2),SD1(:,1),SD1(:,3),'r'); % plotting of mechanical speed
title('Mechanical Speed- reference (blue), Actual (red) [rad/s]');
subplot(2,1,2);
plot(SD1(:,1),SD1(:,4));
title('Mechanical Speed estimated [rad/s]');

figure(3)
plot(SD3(:,1),SD3(:,3),SD3(:,1),SD3(:,2),'r'); % plotting of stator flux
title('Stator flux- reference (red) and estimated (blue)');
```